ABSTRACT

Title of thesis: CLOSED-LOOP CONTROL OF A MICROPOSITIONER USING INTEGRATED PHOTODIODE SENSORS

Mustafa Ilker Beyaz, Master of Science, 2008

Directed by: Professor Reza Ghodssi
Department of Electrical and Computer Engineering

A closed-loop control system with photodiode position sensors has been implemented in a microball bearing supported linear electrostatic micromotor to improve accuracy and reliability. The fabrication sequence of the previously developed micromotor was modified to integrate a photodiode-based position sensing mechanism. Proportional control law is used in the control system and device step response is analyzed for several step sizes at various maximum applied voltages by varying the constant of proportionality. Two critical functions for micropositioning applications have been demonstrated; the device can establish a necessary frame of reference for coordinate-based positioning and autonomously respond to arbitrary disturbances. The closed-loop position control system presented in this work illustrates the feasibility and functionality of smart microsystems using integrated feedback sensors.

CLOSED-LOOP CONTROL OF A MICROPOSITIONER USING INTEGRATED PHOTODIODE SENSORS

by

Mustafa Ilker Beyaz

Thesis submitted to the Faculty of the Graduate School of the
University of Maryland, College Park, in partial fulfillment
of the requirements for the degree of
Master of Science
2008

Advisory Committee:

Professor Reza Ghodssi, Chair
Professor Sarah Bergbreiter
Professor Christopher Cadou

@ Copyright by

Mustafa Ilker Beyaz

2008

DEDICATION

To my mother and father, Muazzez and Enver Beyaz and my sisters Ayten, Nurten, and Ayse Beyaz for their support and encouragement throughout my life.

ACKNOWLEDGMENTS

I sincerely thank my advisor Prof. Reza Ghodssi for his support and guidance throughout my graduate studies. I would like to also thank my committee members Prof. Sarah Bergbreiter, and Prof. Christopher Cadou.

Special thanks to Dr. Matthew McCarthy from MEMS Sensors and Actuators Laboratory (MSAL). I have significantly benefited from our discussions on control systems. Many thanks to Dr. Nima Ghalichechian for mentoring me during my first two years of my graduate life. I would like to also thank all members of MSAL for their assistance and constructive feedback. Thanks to Dr. James O'Connor, Mr. Thomas Loughran, Mr. Jonathan Hummel, and Mr. John Abrahams from Maryland Nanocenter cleanroom facilities for their help with the fabrication. Finally, I would like to thank Army Research Laboratory and Army Research Office for funding this project.

TABLE OF CONTENTS

Chapter 1: Introduction ……………..…………………………………………………….1

1.1 MEMS Background………………………......……………………………1

1.2 Closed-loop Control in MEMS…………………………………………3

1.3 Micromotors as Power MEMS Devices…………………………………..4

1.4 Motivation: Micropositioners……………………………………………..7

1.5 Summary……………………………………………………………………10

Chapter 2: Linear Micromotor……………………………………………………...12

2.1 Introduction………………………………………………………………12

2.2 Micromotor Design………………………………………………………14

2.3 Micromotor Fabrication…………………………………………………….17

2.4 Testing…………………………………………………………………………19

2.5 Summary……………………………………………………………………20

Chapter 3: Position Sensing Design…………………………………………………...22

3.1 Introduction………………………………………………………………22

3.2 Position Sensing Techniques for Linear Micromotor……………………23

3.2.1 Capacitive Position Sensing……………………………………..23

3.2.2 Optical Position Sensing………………………………………...24

3.2.3 Photodiode Selection……………………………………………28

3.2.4 MSM Photodiodes………………………………………………29

3.3 First Generation Photodiodes…………………………………………….34

3.4 Second Generation Photodiodes…………………………………………37

3.5 Control System…………………………………………………………..40

3.6 Summary……………………………………………………………………41

Chapter 4: Fabrication…………………………………………………………42

4.1 Stator Fabrication……………………………………………………...47

4.2 Slider Fabrication……………………………………………………...53

4.3 Summary……………………………………………………………………55

Chapter 5: Test Results……………………………………………………...56

5.1 Test Setup………………………………………………………………..56

5.2 Feedback Configuration…………………………………………………60

5.2.1 Position Feedback…………………………………………………60

5.2.2 Acceleration and Critical Speed Detection………………………...65

5.2.3 Overcoming Friction Barriers……………………………………...67

5.3 Closed-loop Control……………………………………………………..69

5.3.1 System Operation…………………………………………………70

5.3.2 System Step Response……………………………………………..72

5.4 Micromotor Tests for Micropositioning Applications…………………...82

5.5 Summary……………………………………………………………………86

Chapter 6: Conclusion…………………………………………………………87

6.1 Summary……………………………………………………………………87

6.2 Future Work……………………………………………………………...89

Appendix A: Process Recipes………………………………………………..90

Appendix B: Microcontroller Programs…………………...…………………92

References……………………………………………………………………..117

1. Introduction

1.1 MEMS Background

Micro-electro-mechanical-systems (MEMS) is the integration of electronics and mechanical elements with micrometer-scale dimensions on a single chip through microfabrication technology. Due to the enormous diversity of devices designed and manufactured so far, MEMS is used to refer all the devices produced by microfabrication other than integrated circuits (ICs). The field has expanded to magnetic, optical, chemical, and biological domains [1] with device dimensions varying from millimeters to sub-micrometers. MEMS provides a means to interface the digital electronic world dominated by ICs with the analog physical world [2]. The wide variety of non-electrical signals of interest in the physical world [3] is converted into electrical signals through the use of sensors with different transduction mechanisms. In addition, electrical signals are transformed into other physical signals with various actuators to manipulate the surrounding physical environment. These sensing and actuating mechanisms can also be integrated to form complete microsystems.

MEMS technology has been used to develop numerous devices for different applications. Inertial sensors (accelerometers, gyroscopes), chemical and biological sensors (developed for gas, humidity, DNA, bacteria, or virus detection), magnetometers, and pressure sensors are among the products developed on the sensor side of the MEMS research. MEMS actuators produced to date include micromotors, micropositioners, micropumps, microvalves, micromirrors and microrelays. Some of these products (e.g. accelerometers, gyroscopes, and microrelays) have been commercialized and are used in

everyday life. As the microfabrication technology is improved, more devices will be commercially available.

Most of the process techniques and materials used to produce MEMS devices are inherited from the IC industry. Conventional IC fabrication technologies such as photolithography, thermal oxidation, low pressure chemical vapor deposition (LPCVD), plasma enhanced chemical vapor deposition (PECVD), sputtering, wet etching, and reactive ion etching (RIE) are widely used in MEMS to process common materials used in IC industry (e.g. silicon, silicon dioxide, aluminum) [4-5]. Moreover MEMS has driven the development and refinement of other process techniques and materials which are not traditionally used in IC fabrication such as anisotropic wet etching of single crystal silicon, deep reactive ion etching (DRIE), x-ray lithography, electroplating, low stress LPCVD films, thick film resist (SU-8), spin casting, micromolding, batch microassembly, piezoelectric thin films, magnetic films, high temperature materials, stainless steel, platinum, gold, PVC and PDMS [2-4-5].

MEMS fabrication is generally classified in two sub groups: surface micromachining and bulk micromachining. Surface micromachining involves depositing, patterning, and etching a sequence of thin films with submicron to hundreds of microns thickness. The substrate is used for mechanical support and remains un-patterned through out the whole process. In this technique, thin films, referred to as sacrificial layers, are deposited and etched on the substrate to define the mechanical structures of the other layers, referred to as structural layers. Most cantilevers structures are fabricated using this technique [6] for sensing applications. Bulk micromachining differs from the surface micromachining in that the substrate is patterned to form a functional component of the

final device. Many high precision complex three dimensional structures such as V-grooves, channels, pyramidal pits, membranes and nozzles are fabricated using this technique [4, 7]. Additionally, bulk micromachining involves DRIE where structures with vertical side walls can be etched in the silicon wafer independent of the crystal orientation [8, 9]. There are other fabrication techniques that are do not fit in the two sub groups described above. Some applications need more than one substrate to be bonded together. This is achieved by substrate bonding which can be done through fusion bonding [10], anodic bonding [11], eutectic bonding [12], and adhesive bonding [13]. Another technique called lithographie galvanoformung abformung (LIGA) offers the fabrication of high aspect ratio structures on the substrate [14].

The techniques discussed above are used to fabricate MEMS sensors and actuators. The integration of electronics into the MEMS structures can promote the compactness and greatly improve the performance of these devices. Combining MEMS with ICs requires careful consideration of the manufacturing feasibility, complexity, yield and cost [2]. Depending on the specific device, mechanical structures and electronics can be separately produced on different wafers and assembled together, or can be fabricated on the same wafer to realize a complete microsystem.

1.2 Closed-Loop Control in MEMS

Regardless of the actuation mechanism, MEMS devices are typically driven in an open-loop fashion by applying input control signals. Straight forward open-loop driving techniques provide the MEMS designer a simple choice to achieving required behavior. On the other hand, the dynamic requirements of MEMS in terms of response time and

precision have resulted in gradual development of improved controller driving approaches. The input control signals are often made more complex by considering the system dynamic analysis (pre-shaped control) [15-18]. In this technique, the device model is used to design a pre-shaped input signal sequence that enables the device to achieve faster dynamic performance [15].

However, the open-loop control configuration is usually inadequate to achieve high device performance. The lack of accurate models, fabrication imperfections, and changes in environmental conditions all call for the use of closed-loop control design [18-22]. The increase in complexity, device integration and the sophistication level of MEMS demands equally advanced control architectures. Unlike macro mechanical systems where the control system integration is relatively simple, it is very problematic in MEMS devices [15]. Consequently, there are very few microsystems employing feedback control. The requirements for the integration of the control system on the MEMS device have introduced additional challenges for the control system design.

Closed-loop control systems can significantly improve the device performance with a careful selection of control parameters. The purpose of the device, complexity of sensor implementation with the electronic control circuitry, and available space on the device need to be considered when designing the control architecture to achieve accurate and fast dynamic response and realize robust microsystems.

1.3 Micromotors as Power MEMS Devices

Power MEMS is a subgroup of the MEMS field that focuses on the development of micromachines capable of providing power conversion such as micromotors,

microgenerators, and energy harvesting devices. Mechanical and electrical power generation, positioning, and fluid delivery systems are the primary application areas of this field. While micromotors provide mechanical motion for positioning and pumping actions in micro-scale, microgenerators and microengines can supply electrical energy to drive various electrical systems. Among these micromachines, electrostatic [23-26], electromagnetic [27-29], piezoelectric [30-33] and ultrasonic [34, 35] micromotors and microgenerators are widely studied.

Variable capacitance micromotors (VCMs) are among the first fabricated Power MEMS devices. These are synchronous machines that produce torque due to the tangential electrostatic forces resulting from spatial misalignment of the electrodes on the stator and salient poles on the rotor. Trimmer and Gabriel proposed the concept of linear and rotary VCMs in 1987 [36]. The first VCMs were simultaneously developed by two groups at the University of California, Berkeley [37, 38] and Massachusetts Institute of Technology [39]. These were synchronous micromotors fabricated by surface micromachining technique. The development of VCMs was based on the attempts of Lober and Howe on fabricating structures with a top drive VCM [40] that rotated at 500 rpm. Similar fabrication processes reported by Mehregany *et al.* were used for center pin and flange VCMs [41, 42]. These devices produced torques in the range of pico-newton meters. Although functional, these motors had stability and reliability problems due to the bearing design. Harmonic side drive VCMs, also known as wobble VCMs, were developed by Mehregany *et al* and these motors produced more torque due to the normal forces rather than the tangential forces acting on the rotor [43, 44]. The friction, wear and wobbling motion of the rotor limited the applications of this micromotor. One attempt to

reduce the friction and eliminate the wear was demonstrated by Jeon *et al.* [45]. In this design, the rotor was electrostatically levitated by applying voltages of about 500 V. The micromotor was able to achieve a top speed of 60 rpm with an air gap of 300 µm. In addition, linear and rotary micromotors were reported with magnetic levitation [46, 47]. The levitation at smaller gaps requires complex control schemes and therefore is difficult to implement.

An electrostatic induction micromotor was developed by Livermore *et al.* Unlike the VCMs, this is an asynchronous machine which was based on the induction of image charges following the traveling wave on the stator. The micromotor produced 3.5 µNm of torque and reached 55000 rpm [48]. This machine was supported by gas lubricated bearings and required complex fabrication process.

Linear and rotary six phase VCMs supported on microball bearings were reported by Modafe and Ghalichechian *et al.* in MEMS Sensors and Actuators Lab at the University of Maryland, College Park (UMD) [49, 50]. The linear micromotor was observed to produce 0.19 mN of force and was able to run with a synchronous speed of 7.3 mm/s at 40 Hz excitation frequency [49]. This device was developed mainly for millimeter-scale micropositioning applications and later served as a platform for rotary design. The rotary micromotor designed and fabricated recently provided a torque value of 5.6 µNm and rotated at 517 rpm [50]. Microball bearings were shown to be a more stable support mechanism with less fabrication complexity compared to gas lubricated bearings. Additionally they exhibit less friction and wear compared to center pin designs.

The stability problems of micromotors arising from some factors such as friction, wear, fabrication imperfections limit a reliable operation for micropositioning and

micropumping applications. Therefore new solutions have to be introduced to the machine design for realizing robust machines. The control of micromotors is gaining importance as new micromotors in different operating principles are being developed based on micromachining technology. Small and efficient control systems will greatly promote the performance and reliability of such micromachines [51, 52].

1.4 Motivation - Micropositioners

Micropositioners capable of accurate and reliable operation over long actuation ranges are required for a variety of next-generation applications. The development of such micropositioners is essential for the realization of high-performance optical, data storage, and surface scanning components within compact low-cost distributed microsystems. This work focuses on the development of an integrated feedback control system for accurate dynamic positioning of a variable-capacitance micromotor supported on microball bearings over millimeter-scale range.

Micro- actuators and positioners have been demonstrated with a variety of actuation mechanisms including electrostatic, thermal, magnetic, and piezoelectric. Patrascu *et al.* [53] and Lee *et al.* [54] have reported micropositioners using electrostatic actuation in stepper and comb drive configurations, respectively, with displacement ranges of less than 200μm. Additionally, a cantilever-based optical switch using electrostatic actuation to bend waveguide structures has been demonstrated [55]. The tethered nature of these devices couples the actuation forces and displacement distances, limiting there operation to specific deflections and precluding their use in long-range applications. Devices using a similar tethered design and thermal actuation have been

reported for ranges of up to a few hundred microns [56], [57]. In addition to range limitations, these devices require large temperatures and temperature gradients to provide actuation. Magnetic and piezoelectric actuation mechanisms have also been used to develop microfabricated positioners with ranges of up to 12μm [58], [59]. While an inchworm micropositioner capable of moving up to several millimeters has been developed by Cusin *et al.* [60], the actuation speed (~300μm/s) is likely too slow for most applications.

Robust and repeatable actuation requires integrated feedback control, and accordingly, has been investigated for microfabricated positioning systems. Chu *et al.* [61] developed a two-dimensional electro-thermally actuated micropositioner using capacitive position sensors for feedback control. They were able to achieve high-resolution positioning over a 19μm range. Similarly, an electrostatic micropositioner with capacitive sensing and a positioning range of 2.8μm was demonstrated by Horsley *et al.* [62]. Continued work in the field of closed-loop control for MEMS-fabricated actuators is required for the realization of high-performance microsystems capable of accurate and long-range positioning.

Previous work by our group has demonstrated variable-capacitance micromotors supported on linear microball bearings [49], including characterization of the drive mechanism using benzocyclobutene-embedded electrodes [63] - [65] as well as the microball support mechanism [66] - [69]. Electrostatics and linear microball bearings have been shown to be stable and robust actuation and support mechanisms created through simple fabrication processes. The range of these devices is limited by the length of the microball housings, while the positioning resolution is dictated by the variable-

capacitance electrode spacing. Using such a design, the actuation force and translation distance have been decoupled. This allows for a continuous in-plane force to be applied over the entire range of displacement, making these devices highly desirable for long-range applications. This design, however, is susceptible to random disturbances and variations in microball rolling friction leading to erratic behavior. Accordingly, this work focuses on the development of integrated photodiode-based position sensors and a proportional control law to drive such devices under closed-loop excitation.

Closed loop control systems have been previously investigated for micromotors. Control architectures have been designed using electrical microsystems based on capacitive detection technique [70-73]. These systems detect the critical angles of the rotor position with respect to the stator by measuring the capacitance between the rotor poles and stator electrodes. Applied voltages are adjusted depending on the pole-electrode alignment condition. Designed systems are simulated and tested. However to the best of my knowledge, no implementation has been demonstrated for an electrostatic micromotor.

Guckel *et al* developed a magnetic micromotor and used integrated photodetectors to measure the angular speed of the rotor [74]. The photodetectors were fabricated under the rotor and the electrical output of these detectors changed when a rotor pole passed on, allowing for the calculation of the time between two such events. The micromotor was driven in an open loop fashion, however the possibility of using these detectors as position sensors as part of a feedback control system was discussed.

Control systems for electromagnetic micromotors have also been developed [75, 76]. Lyshevski has integrated the soft switching controllers into a permanent magnet

micromotor with hall sensors [76] and showed improved speed response with a settling time of less than 1 milisecond. It is also reported that the implementation of this system allowed the micromotor to achieve high efficiency, desired steady state, stability and controllability [76].

Following chapters describe the details of the design and implementation of the control system. Closed-loop position control, along with reliable millimeter-range microball bearings and a simple electrostatic actuation principle, are used to demonstrate the viability of smart microsystems using integrated feedback sensing.

1.5 Summary

Chapter one provides the concept of MEMS, fundamental fabrication techniques, power MEMS devices, micromotors, micropositioners, and control systems in MEMS domain. Basic micromotor types and the necessity of a feedback control are discussed. Previous work in the field of micromotor control is covered. Although the implementation of the feedback systems in macro world is straight forward, it remains problematic in micro domain. Once very sophisticated control systems are integrated in micromotors, the development of smart micromachines will be possible.

Chapter two explains the structure of linear variable capacitance micromotor developed at UMD. Operating principle, device design parameters, fabrication sequence are described, and test results are briefly discussed. The need for control system and how it can affect the device performance are also explained.

Chapter three covers the possible position sensing schemes for the linear micromotor. Capacitive position detection technique is evaluated and the advantages and

disadvantages are explained. Optical position detection is described and shown that it is more advantageous to use this technique. Photodetectors as optical sensors are discussed and photodiode design is described in detail. Some initial photodetector test results and circuits to process photodiode signals are also included.

Chapter four goes through the integration of the photodiode sensors into the linear micromotor process flow. The modifications in the original micromotor fabrication are explained and the bottlenecks of the process are presented. Alternative ways for the integration are discussed.

Chapter five presents the operation of the micromotor using the closed loop system. Test setup is described in detail. Improved stability together with autonomous decision making to overcome friction barriers is demonstrated. Device step response with the closed loop control is characterized and the device is tested for micropositioning applications. These results prove the functionality of the control system and the enhancement in the device reliability.

Chapter six provides a summary of the results and future work. The appendix section covering the very details of the work and the references section are also presented at the end.

2. Linear Micromotor

2.1 Introduction

This chapter discusses the previously developed microball bearing supported linear electrostatic micromotor design [49, 77]. The micromotor is a six-phase variable capacitance micromachine that relies on tangential capacitive aligning forces created by electrostatic actuation. Ball bearing is selected to decrease the friction and provide a robust support mechanism for the device. Figure 2.1 shows the schematic illustration of the micromotor.

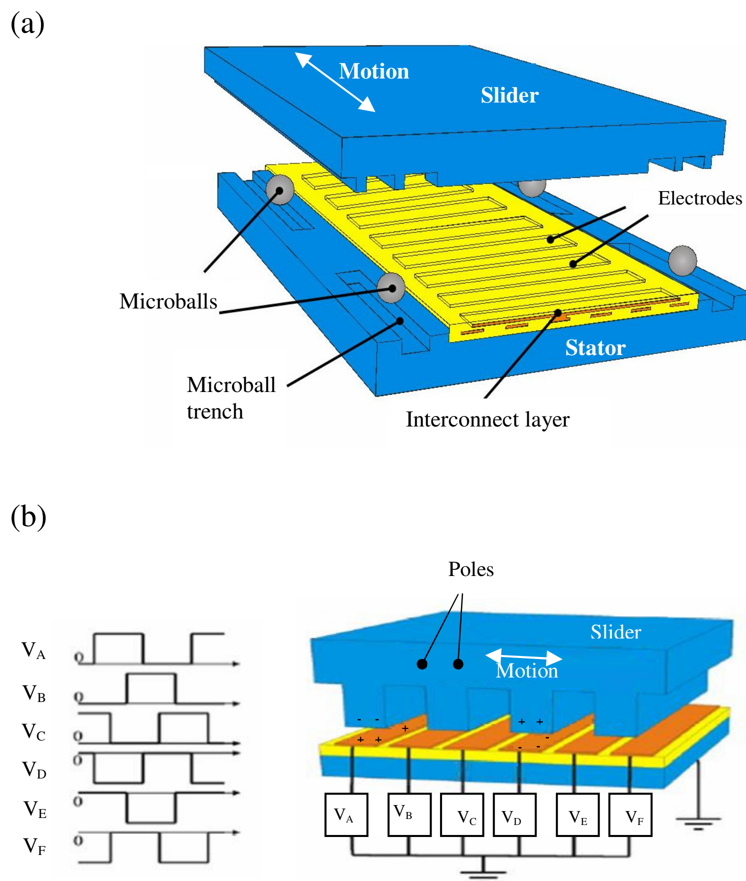

Figure 2.1: (a) Schematic of the micromotor showing stator structure, electrodes, interconnect layer, slider, and microballs, (b) the electrical phases and the side view of the micromotor showing slider poles.

The fundamental principle of operation is that when voltages are applied to the electrodes on the stator, charges flow from power source to the electrodes. This results in the opposite image charges to appear on the slider poles. Consequently, the poles are forced to be aligned with the excited electrodes resulting in lateral motion. When the electrodes are excited sequentially, creating a traveling wave, the slider follows the excitation and continuous motion in one dimension is generated.

The stator phases A-B-C shown in Fig. 2.1 (b) have 120° phase difference while the phases D-E-F are in phase with A-B-C respectively but negative in magnitude. This six phase configuration is shown to prevent charge build-up on the slider [49].

The micromotor is fabricated using Si MEMS process techniques. Every sixth electrode on the array shown in Fig. 2a is connected via underlying interconnect layer. The isolation between the electrode and interconnect metal layers is provided with a low-k dielectric benzocyclobutene (BCB). The same dielectric is used to isolate the interconnect layer from the Si substrate. The low-k feature of this material decreases the parasitic capacitances between the interconnects and the substrate, increasing the efficiency of electrostatic actuation.

The microball trenches on the stator and slider wafers together with the slider poles are defined by deep reactive ion etching (DRIE). The slider has one microball trench on each side. On the other hand, two trenches instead of one on the each side exist on the stator to avoid the ball collocation that may result in the slider to loose the mechanical stability and collapse on the stator. This design ensures that the balls on one side will never localize at one point on the trench.

2.2 Micromotor Design

Three different stator structures have been designed based on the electrode width and spacing [49, 77] which determine the speed and force of the micromotors. In all the designs, electrode and pole dimensions (length and width) within each design were equal. However the electrode and pole spacings were different, resulting in an electrode to pole ratio of 3:2. Figure 2.2 shows this structure.

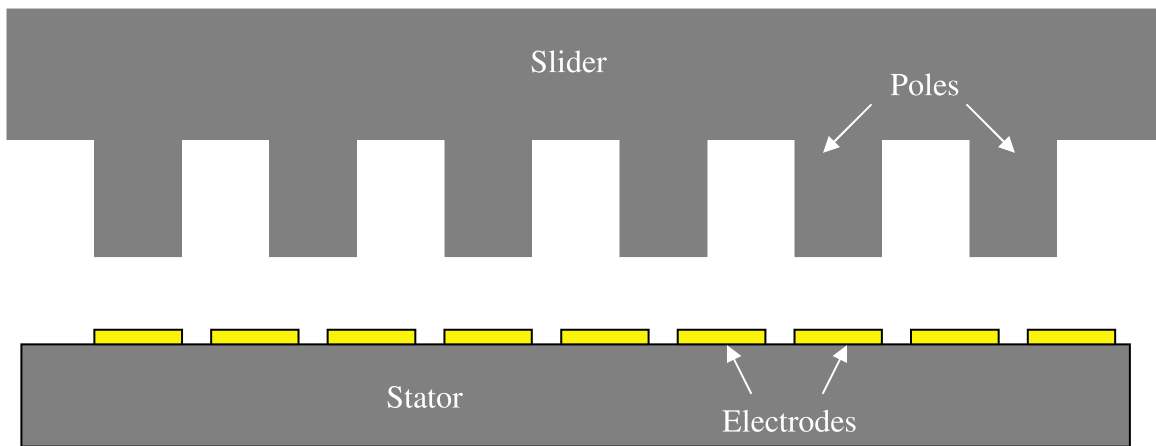

Figure 2.2: Schematic side view of the stator electrodes and slider poles.

The total length of the micromotor was also a design parameter. A short and a long micromotor structure had been designed for each electrode width [77]. Table 2.1 summarizes the micromotor design parameters.

	Design 1	Design 2	Design 3	Design 4	Design 5	Design 6
Width (electrode, pole in µm)	30, 30	90, 90	180, 180	30, 30	90, 90	180, 180
Spacing (electrode, pole in µm)	10, 30	30, 90	60, 180	10, 30	30, 90	60, 180

Length (stator, slider in mm)	10, 6.2	10, 6.2	10, 6.2	16, 10	16, 10	16, 10
Width (Stator, slider in mm)	5, 5	5, 5	5, 5	5, 5	5, 5	5, 5

Table 2.1: Micromotor design parameters

Design 1 and design 3 correspond to high force and high speed micromotors respectively. Design 1 has the most number of electrodes and the possible electrode-pole misalignment is minimum, and this structure produces the most force. At each electrode excitation, the slider travels 2/3 of the electrode width. Therefore design 3 with the minimum number of electrodes provides the highest speed. Design 2 is a compromise between the high speed and high force [77]. The L-edit schematics of a stator with 90 µm wide electrodes and the whole stator wafer is shown in Fig. 2.3 and Fig. 2.4, respectively.

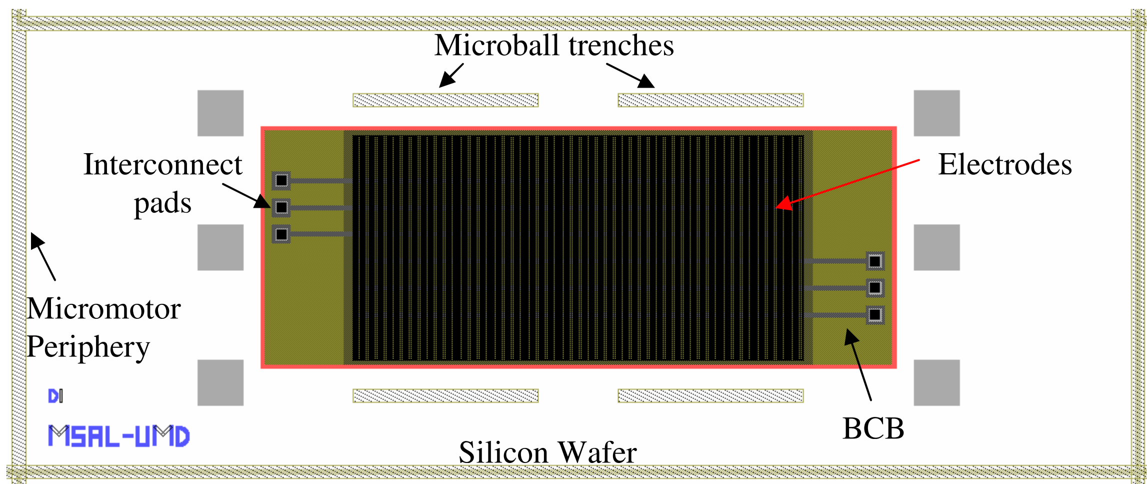

Figure 2.3: The L-edit layout of a micromotor with 90 µm electrode width. The individual electrodes are not visible.

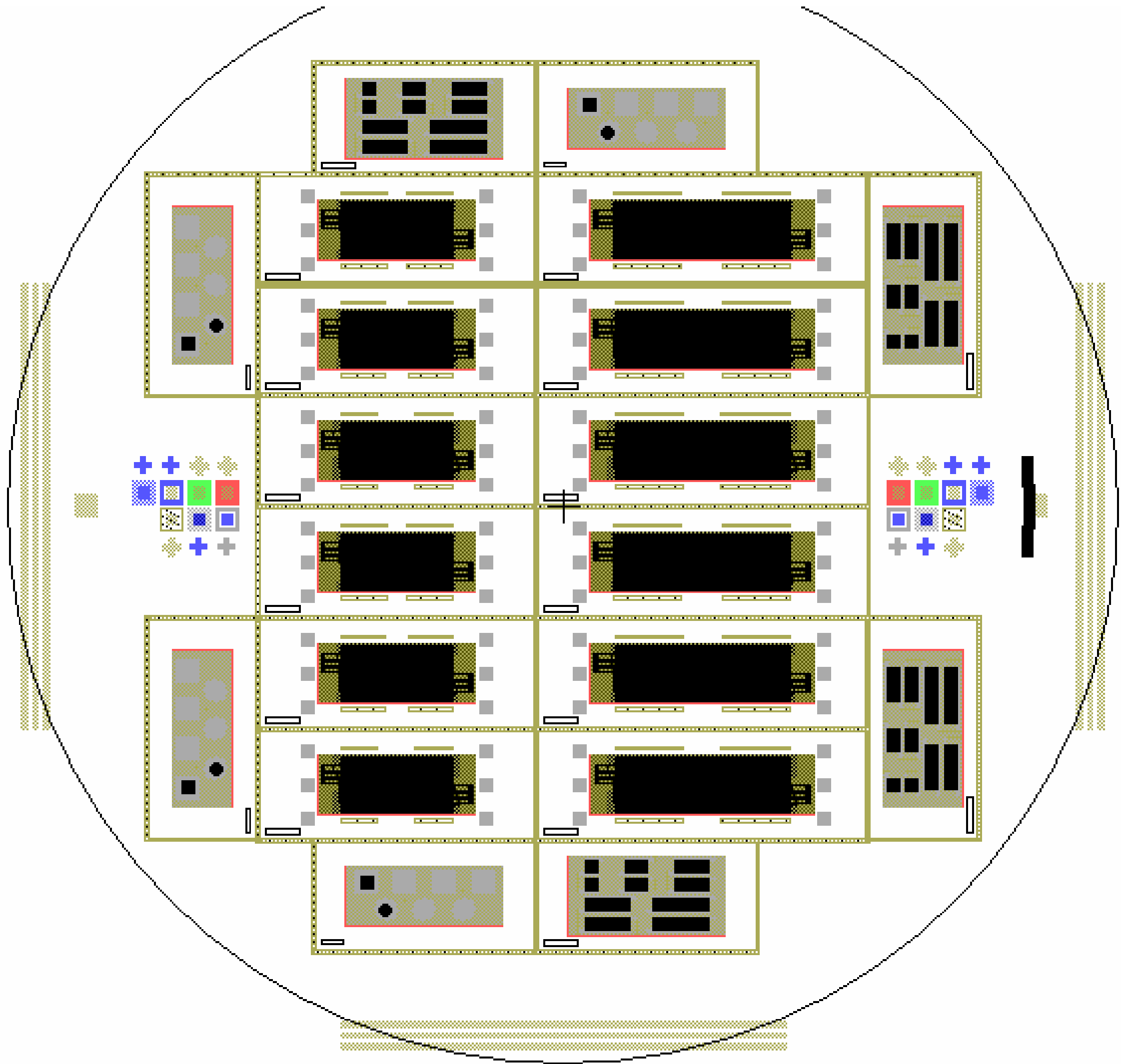

Figure 2.4: L-edit schematic of the wafer having 12 stators. Short micromotor designs are on the left and long designs are on the right.

The microball trenches are designed to be 290 µm wide to ensure that the 285 µm diameter stainless steel would fit in. The depths of the trenches in the stator and slider are determined to be 130-135 µm, so that the final gap between the poles and electrodes would be around 10 µm. This gap ensures that enough electrostatic force can be created while the slider is avoided to contact the stator surface due to the fabrication imperfections [77].

2.3 Micromotor Fabrication

MEMS Si process technology was used to fabricate the linear electrostatic micromotor and a total of eight optical chromium masks were utilized for the completion of the process [77, 78]. Stator fabrication consists of depositing dielectric and metal layers on Si substrate, and etching trenches for microballs. The first BCB dielectric layer deposited on the substrate provides isolation between the metal layers and semiconducting substrate. BCB is a material that is sensitive to ultraviolet light and that can be spun on a wafer. Therefore lithography technique is used to deposit and pattern BCB dielectric layers. The first metal layer deposited on BCB serves as an interconnect layer. The voltages are carried to the electrodes via this layer that is composed of six metal lines, one for each phase. Cr and Au was sputtered the wafer and patterned using wet etchants and the interconnects were formed. Next, another BCB layer was deposited for the isolation between the electrodes and interconnects. This BCB has via holes allowing the electrodes to be connected to the interconnect lines. Consequently every sixth electrode is connected via the underlying interconnect line.

The electrode layer was deposited by sputtering Cr and Au. A liftoff method is used for patterning the metal electrodes [78]. The stator fabrication was completed by a third layer of BCB for passivation and deep etching 130-135 μm trenches for the microball housing. The same DRIE process was performed for defining the microball trenches and poles on the slider. The details of the fabrication steps can be found in [77, 78]. Figures 2.5 and 2.6 show pictures of the fabricated stator and slider.

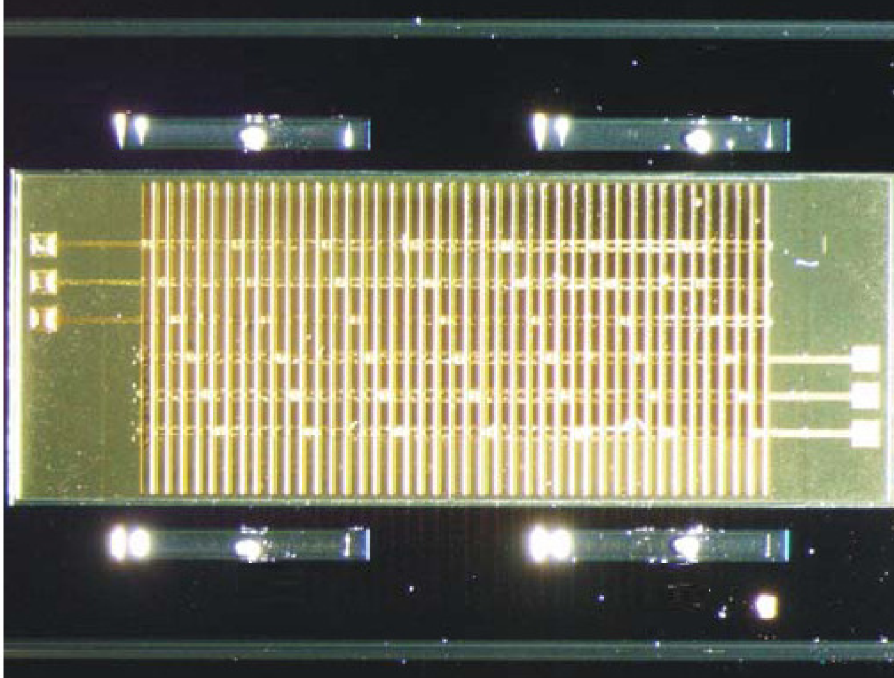

Figure 2.5: A fabricated stator. The electrode and interconnect structures are clearly visible. One ball is placed on each trench.

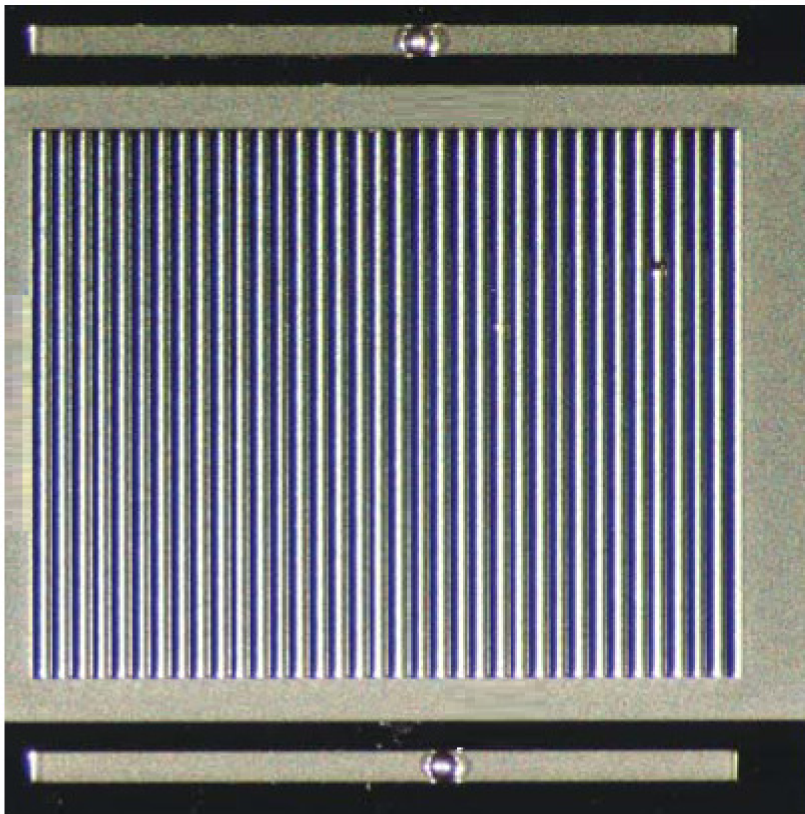

Figure 2.6: Bottom view of a fabricated slider.

2.4 Testing

A test setup had been built to investigate the micromotor performance. In this setup, a computer with the lab view program had been used for outputting the necessary square wave voltages. The output voltages were amplified by a high voltage amplifier (HVA) and applied to the stator via electrical probes. Meanwhile, a high speed camera and an image tracking software were employed to independently measure the slider motion.

The main focuses of the tests were measuring the speed and force produced by the micromotor. The fabrication imperfections and friction problems avoided the designs with 30 μm and 180 μm electrode widths to function properly. The micromotors with 90 μm wide electrodes worked as expected. Maximum synchronous speed and average force produced by 90 μm electrode width design were measured to be 7.32 mm/s and 0.19 mN respectively, showing good agreement with the theoretical values [49, 77]. Figures 2.7 and 2.8 show the slider trajectories for a 90 μm electrode width design tracked by the camera.

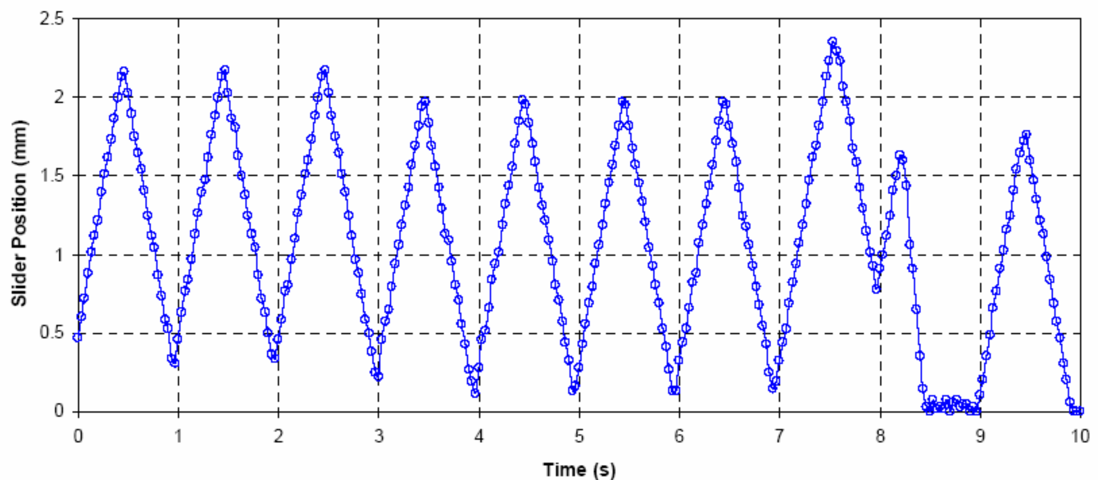

Figure 2.7: Slider position versus time graph. The device was excited at 20 Hz at 100 Volts peak to peak square wave.

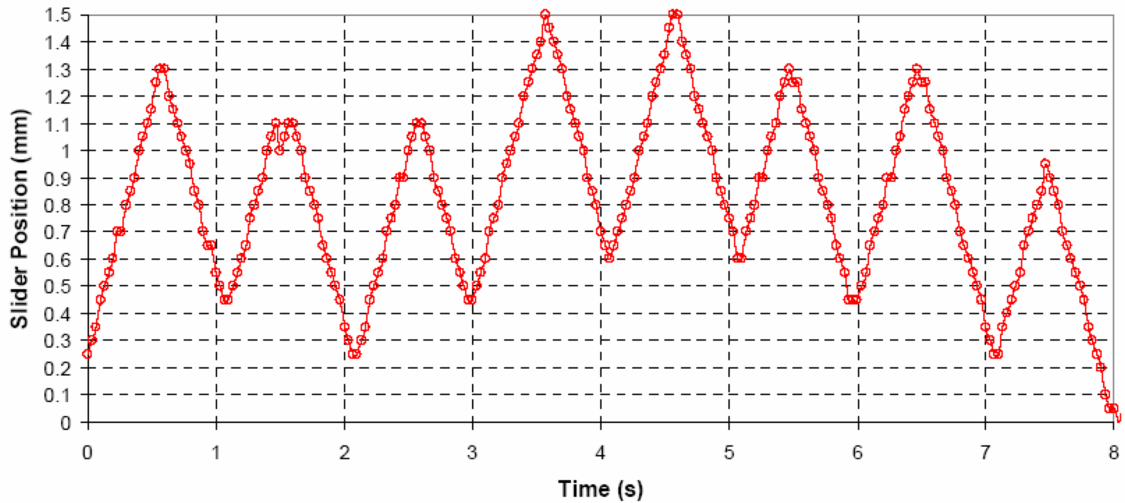

Figure 2.8: Slider position versus time graph. The device was excited at 10 Hz 100 Volts peak to peak square wave.

The figures show successful electrostatic actuation of the slider. Perfect triangular patterns were expected in both figures. However due to the random friction behavior, the motion is not smooth and the peaks of the waveforms drift over time. This shows a synchronization problem and precludes the use of this device as a micropositioner.

2.5 Summary

The first micromotor supported on ball bearings is described in this chapter. Design details are discussed, fabrication process is explained and test results are briefly presented. This work formed a basis for rotary electrostatic micromotor that has recently been demonstrated [79].

One of the problems of the micromotor was shown to be the lack of control on the slider motion. The slider moves in a random manner due to the unpredictable behavior of friction. Therefore feedback system integration is required to sense slider position and

modify the electrical signals for a reliable operation. The next chapter discusses the position sensing mechanism designed for this micromotor.

3. Position Sensing Design

3.1 Introduction

The most important element of the control system in a micromotor is the position sensor as the performance of the device depends on accurate feedback signals. Therefore extra effort has to be spent to design a position sensing mechanism that is reliable and has high signal to noise ratio for precise position information. Actuation signals are then applied to the micromotor by electronic circuits that process sensor signals.

The most straightforward way of detecting slider position in a variable capacitance micromotor is the capacitive sensing technique which does not need any additional elements to be implemented in the micromotor. In this technique, the critical positions of the moving component (slider or rotor) are detected by a circuit measuring the capacitance between rotor poles and stator electrodes. The output of this circuit is fed into actuating circuits which determine the voltages to be applied to stator electrodes. However, capacitance change is usually small and consequently very sophisticated circuits are needed to sense the differential capacitance of the motor. Moreover, fabrication imperfections in electrodes and poles make it even harder to use capacitance sensing technique since these defects mislead detection circuits.

Another way of obtaining feedback signal is by using optical detection technique which requires photodetectors to be implemented in the micromotor. In this technique, the amount of light received by the photodetector depends on the slider location. Photodetector output current changes in correspondence with the slider-position-dependent illumination and this current change can be detected by a circuit. This usually

gives a signal with a higher signal to noise ratio than capacitive sensing technique, however it requires photodetectors, most commonly photodiodes, to be implemented in the fabrication process.

Other position sensing mechanisms for feedback loops can be proposed. However they usually come with a signal to noise ratio or implementation cost. The appropriate mechanism should be chosen by considering specific micromotor configuration.

3.2 Position Sensing Techniques for Linear Micromotor

3.2.1 Capacitive Position Sensing

The feasibility of capacitive position sensing mechanism has been investigated for the linear micromotor. As the slider travels on the stator, the capacitance between one stator electrode phase and slider poles is expected to oscillate between a maximum and a minimum capacitance value. When the capacitance reaches its maximum, one stator phase and poles are perfectly aligned. This is one of the critical slider positions at which the applied voltage set has to be changed. Therefore the goal is to detect maximum capacitance for three different phases.

One of the previously fabricated micromotors has been tested for monitoring capacitance variation. In this test, the slider is moved manually with a probe and capacitance values between one phase and slider poles are measured by a capacitance meter. The resulting graph in Fig. 3.1 shows the capacitance variation as the slider travels.

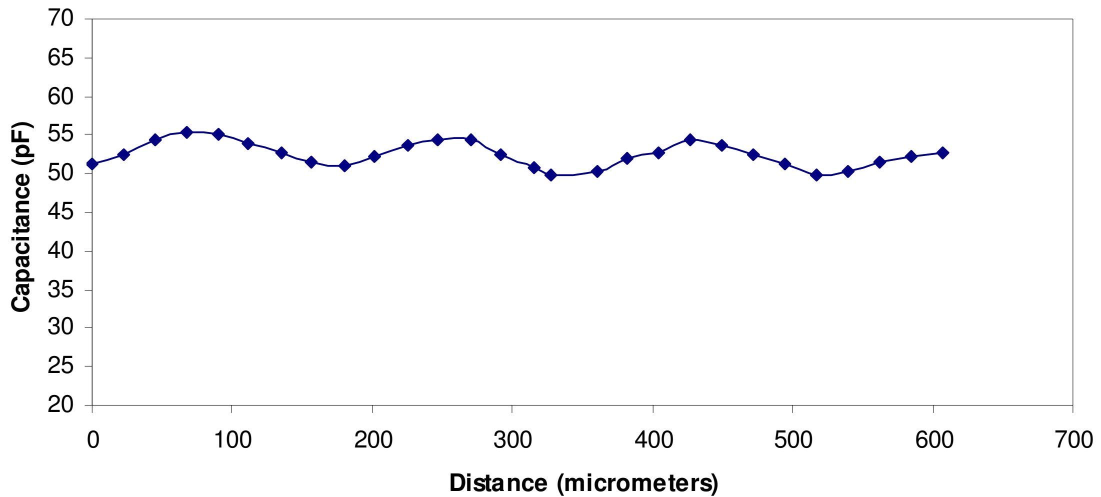

Figure 3.1. Capacitance variation of one phase with respect to slider position.

This graph shows that the change in the capacitance is around 10% of the minimum value. Moreover maximum and minimum capacitances drift as the slider moves, making it very difficult to obtain a reliable feedback. Therefore, alternative ways were investigated for position feedback.

3.2.2 Optical Position Sensing

The critical slider positions can also be detected using a photodetector scheme. Photodiodes have to be implemented and fabricated on the stator for this technique. If an array of holes is introduced in the slider and light is provided from top, pole-electrode alignment can be related to the light amount reaching photodiode surface and increasing the diode current. Full alignment is desired to match with the maximum photodiode current which can be measured and detected by a circuit. The maximum to minimum current ratio can be enhanced for a clearer signal by increasing the light intensity,

eliminating the need for advanced electronics and decreasing system complexity in contrast to the other methods. Therefore, efforts have been focused on designing an optical position sensing based feedback system.

One photodiode is assigned for detecting the alignment of each phase with the poles on the slider, and consequently, at least three photodiodes are needed in this micromotor corresponding to three distinct stator phases.

The diode geometry has to be determined such that maximum alignment corresponds to maximum diode current to implement optical position sensing as explained above. The first requirement for this correspondence is that photodiodes should be located on the stator aligned with the electrodes. Similarly, through holes should be etched aligned with the slider poles. Additionally, the widths of photodiodes, holes, electrodes and poles should be equal. This results in the simultaneous alignment of electrode-pole and photodiode-hole pairs during the motor operation, allowing the available light passing through the hole to reach the photodiode and to illuminate the whole diode surface. Once this happens, the number of photogenerated electrons and holes in the diode depletion region reaches its peak value and diode current becomes maximum. The maximum current value can converted to a feedback signal by using electrical circuits. The micromotor configuration including photodiodes is shown in Fig. 3.2.

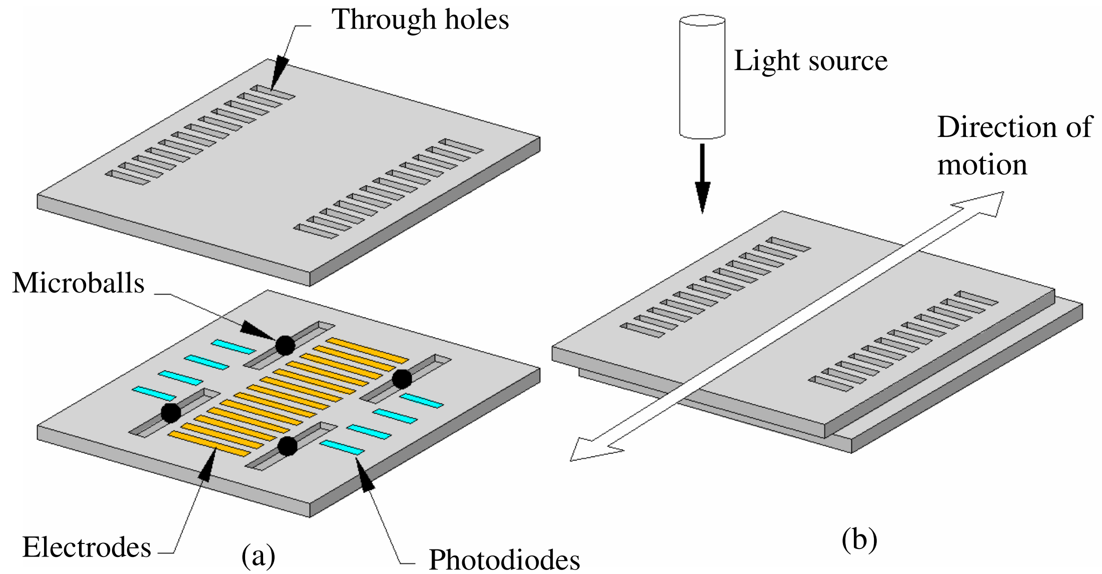

Figure 3.2. Micromotor configuration with optical position sensing scheme showing a) electrodes, photodiodes, microballs on the stator, and through holes on the slider, b) direction of motion and position of the light source during the operation.

Another requirement is that, the feedback system should be implemented in the available micromotor area without changing the original structure so that the number of masks to be designed and purchased for the new generation micromotor will be as few as possible, decreasing the fabrication cost. Consequently, photodiodes should be located in the available space on the stator. The least number of modifications is desired for the slider, similarly. Only one mask was used for slider fabrication to define poles and trenches previously. If the same mask is to be used, one additional mask has to be made for defining the holes and the related photolithography should be performed on the backside of the slider so that the holes can be etched through the wafer. However it is very difficult to attain perfectly vertical holes using Deep Reactive Ion Etching (DRIE). The difference in the hole area between the upper and lower surfaces of the slider would directly mislead the photodiodes and the feedback system. This provided the motivation for performing the hole etch in two DRIE steps. The first DRIE on the front side of the

wafer defines poles and trenches together with the holes, and the second large area DRIE on the backside finishes the fabrication of the holes. Therefore two new masks were designed for the slider. The structures of the stator and slider masks are shown in Fig 3.3 and Fig 3.4, respectively.

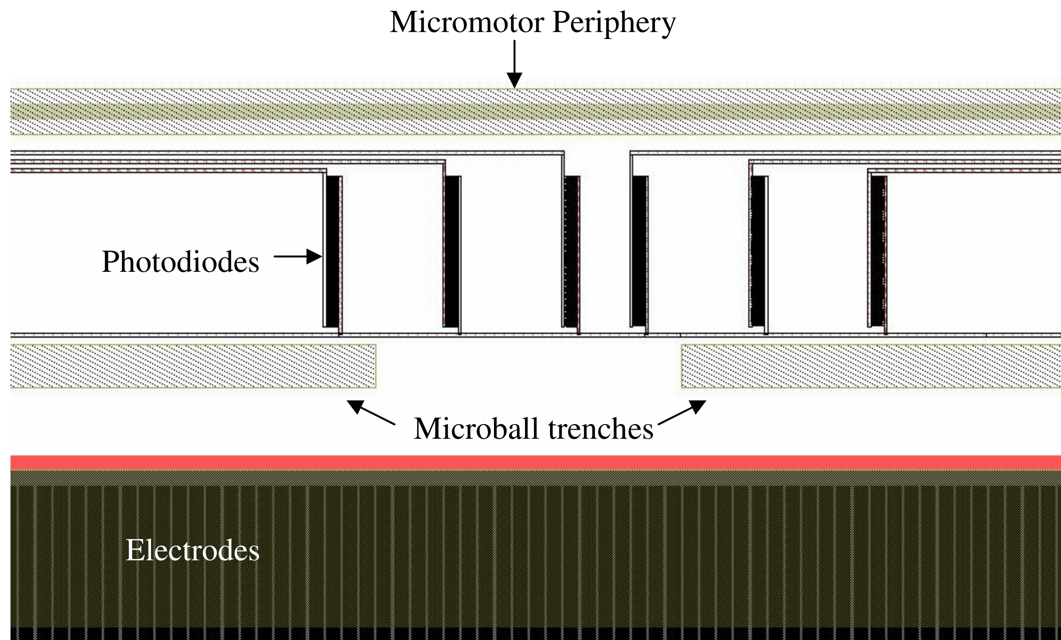

Figure 3.3. L-edit file showing the new stator structure. The picture shows upper middle part of the stator, electrodes, microball trenches and photodiodes aligned with electrodes. Each photodiode is aligned with a different electrode phase. Three photodiodes are used during the operation, however more than three photodiodes are located on the stator considering fabrication imperfections which may result in problems with photodiode fabrication.

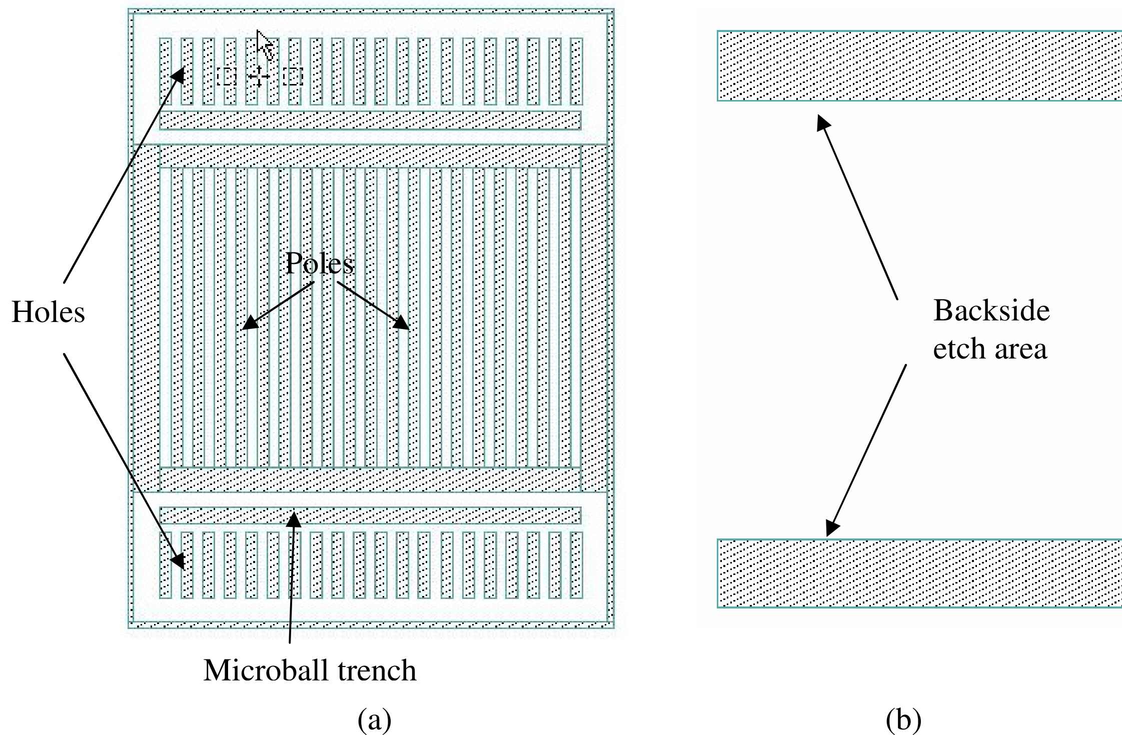

Figure 3.4. (a) Front and (b) back sides of the slider mask.

3.2.3 Photodiode Selection

As mentioned above, the optical position sensing based feedback system is expected to provide a clear position information and feedback signal. However it needs photodiodes to be implemented in the micromotor fabrication. A photodiode structure that would yield the least number of modifications in the original fabrication process needs to be selected to alleviate this disadvantage. The common types of photodiodes are:

- p-n junction photodiodes
- p-i-n phtodiodes
- Avalanche photodiodes
- Metal-Semiconductor-Metal (MSM) photodiodes

P-n junction and p-i-n junction photodiodes require ion implantation and metal deposition for achieving the desired doping level and ohmic contacts. Therefore at least three masks and three photolithography steps are required. Similarly, Avalanche photodiodes need several masks and lithography steps for the diode junction and carrier multiplication layers. On the other hand, MSM photodiodes can be fabricated by depositing and patterning one metal layer on silicon that requires one optical mask and one lithography step. Therefore considering the fabrication complexity, MSM photodiodes are preferred for the photodiode selection.

3.2.4 MSM Photodiodes

An MSM photodiode usually consists of interdigitated Schottky metal contacts on top of a semiconductor absorption layer. It is a high speed device due to its low capacitance. The responsivity, which is defined as the output current per incident light power, is adequate for position sensing but lower compared to p-i-n and avalanche photodiodes. The main causes for the low responsivity are the reflection from the surface metals and semiconductor surface, the finite carrier lifetime as the carriers traverse the gap between the electrodes, surface recombination currents, and deep traps within the semiconductor material which may lower the detected optical signal. However a series of amplifiers can be used to enhance the signal. Figure 3.5 shows a schematic illustration of an interdigitated MSM photodiode.

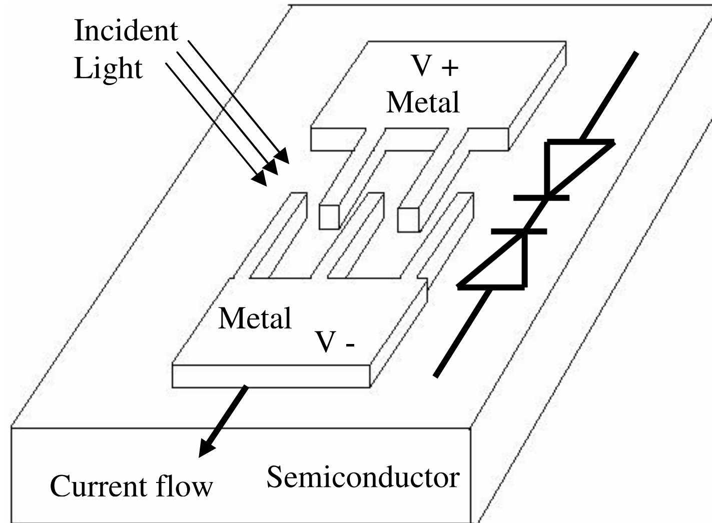

Figure 3.5. Schematic of interdigitated MSM photodiode showing the applied voltage and the direction of the current.

Correct selection of the metal and semiconductor yields a Fermi level difference and a Schottky contact between these two materials, creating a depletion region in the semiconductor. In the presence of light, photogenerated electrons and holes move in the electric field created by the applied voltage and contribute to the output current. The two metal electrodes on the semiconductor form two Schottky diodes connected back to back. Regardless of the polarity of the voltage, one diode is forward biased and the other is reverse biased. This configuration results in low dark current, which is the output current when there is no incident light, due to one of the reverse biased metal-semiconductor junctions. Interdigitated geometry increases the total electrode area and depletion region allowing more carriers to be generated by light.

Medici simulations have been performed on interdigitated MSM photodiodes to determine the critical parameters such as finger width and finger spacing. However due to the 2D nature of these simulations, the desired 3D response of the diodes could not be attained. These parameters are determined after experimental results.

The material selection for the semiconductor substrate is Si since the micromotor fabrication is performed on a Si wafer. However, the substrate was changed to n type Si from the original p type Si for attaining a Schottky contact. One key requirement for the Schottky diode is that the barrier height should be high to yield low dark current. This is desired to have a large difference between the dark and photo currents. Schottky height between a metal and Si is given by the equation 2.1 [80],

$$\Phi_B = \Phi_M - \chi \tag{2.1}$$

where Φ_B is the barrier height, Φ_M is the metal work function and χ is the electron affinity of Si which is 4.05 eV. Therefore, a metal with a metal work function greater than 4.05 eV should be selected for forming a Schottky barrier. The work functions of some metals are given in Table 2.1 below [81]:

Metal	Work Funciton in eV
Al	4.28
Ti	4.33
W	4.55
Mo	4.60
Cu	4.65
Ni	5.10
Au	5.15
Pt	5.65

Table 2.1: Work function of common metals [81].

Au and Al metals were available during the fabrication of the device. Moreover they are compatible with the micromotor fabrication process. Therefore efforts have been focused on these two materials.

The high work function feature makes Au very appealing for the metal selection. It is also one of the metals used for interconnect and electrode layer fabrication, making it a good candidate for photodiode metal as well. To fabricate Au photodiodes, the native oxide layer on the substrate was first etched using buffered oxide etch (BOE) and a clean metal-Si interface is attained. Next, Au was sputtered on n-Si 20 Ωcm substrate to a thickness of 0.3 μm. Photolithography has been performed after the sputtering using AZ5214E photoresist and a mask which had interdigitated features on it. However during the development step of the photolithography, the sputtered gold completely peeled of from the substrate due to the poor adhesion between the Au and Si. Therefore, it was not possible to fabricate Au photodiodes on Si.

Al was also used to fabricate photodiodes and same procedures have been followed. After a successful lithography, Al has been etched using Transene Al wet etchant type D and the photoresist has been stripped, completing the photodiode fabrication. A picture of the fabricated photodiodes is shown in Fig. 3.6.

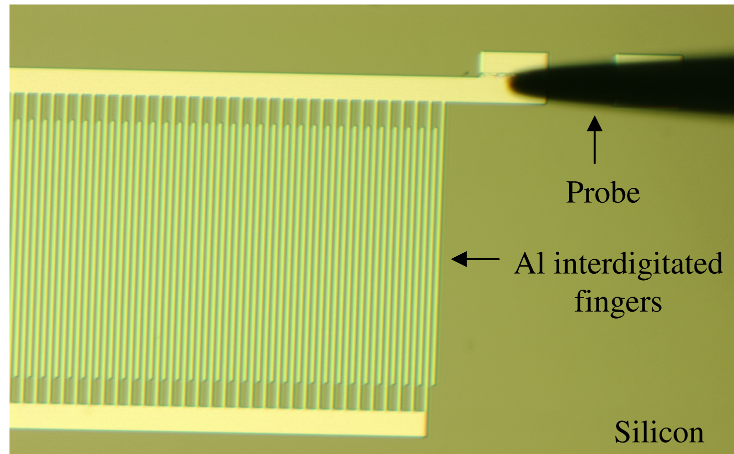

Figure 3.6. A fabricated photodiode being tested.

The photodiode shown in Fig 3.6 has an area of 5×1 mm^2 and it has a finger width and spacing of 5 μm. This interdigitated structure was previously used to investigate the dielectric constant of BCB by creating many capacitances in parallel when designing the micromotor [77]. For the testing purposes, same structure has been fabricated to evaluate the I-V characteristics of Al-Si MSM photodiodes. The output current was measured at 0-5 V applied bias voltage. The resulting I-V characteristics is shown in Fig. 3.7.

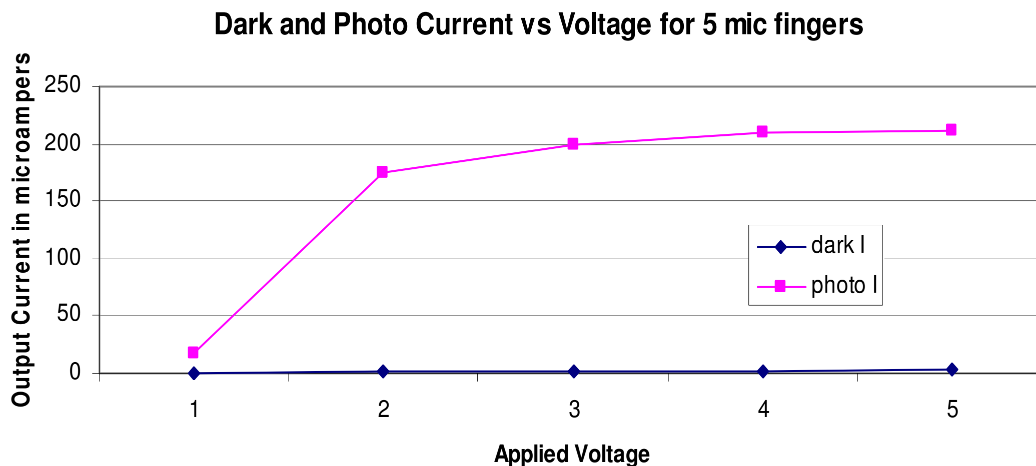

Figure 3.7. Photodiode I-V characteristics.

This plot shows an expected reverse bias saturation current curve. Responsivity was measured to be 0.2 A/W. The frequency response of the photodiode has also been evaluated for the frequencies of interest, 0-500 Hz. No noticeable change in the photodiode current has been observed at these frequencies. The rise and fall times of the photodiode output were measured to be on the order of 10 microseconds.

This current-voltage curve varies from wafer to wafer, i.e the maximum and minimum current values on the graph change for each wafer. This is attributed to the different doping values of the wafer varying from 20 to 40 Ωcm wafer resistance. Also the condition of the Al sputtering target might have been different for each deposition, i.e the same quality of metal can not be attained repeatably. Therefore the variation in output current was expected.

3.3 First generation photodiodes

The results obtained from the test photodiodes were evaluated to determine the important parameters of the interdigitated structure: finger spacing and finger width. The operating frequency of the photodiodes favors short finger spacing for the photogenerated carriers to traverse less distance. On the other hand, responsivity of the photodiodes favor the large finger spacing and small finger width to allow more light to reach Si surface. As more photoactive Si area (depletion region) receives light, more photogenerated carriers are created. Due to fabrication limitations, the finger width was selected to be 4 μm to safely define the fingers. Furthermore, the test results showed that photodiodes can operate much faster than the frequency of interest. Therefore finger spacing was not an issue and increased to 7 μm. The final dimensions of the photodiodes were determined to

be 30µm×1mm, 90µm×1mm, and 180µm×1mm corresponding to the motor designs with different electrode widths. A picture of fabricated photodiodes is shown in Fig. 3.8.

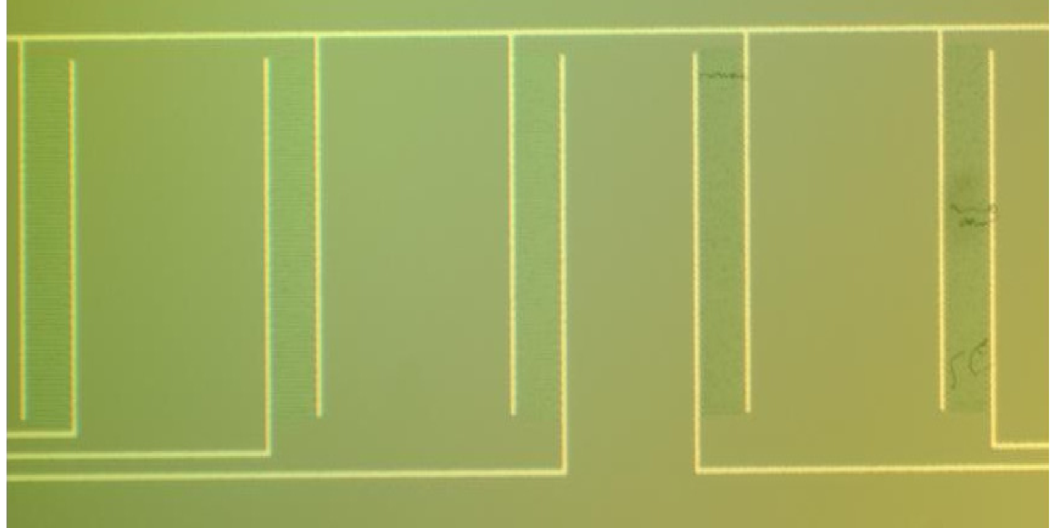

Figure 3.8. A picture of fabricated first generation photodiodes. The photodiode width is 180 µm.

A circuit composed of an opamp amplifier and comparator was built to sense the maximum photodiode current to detect the full hole-photodiode alignment. A slider with through holes was fabricated to test the sensing mechanism. In this test, the slider was moved manually on the photodiodes while photodiode fingers were biased at 4 Volts. Figure 3.9 shows two pictures taken during the test and Fig. 3.10 illustrates the circuit schematic.

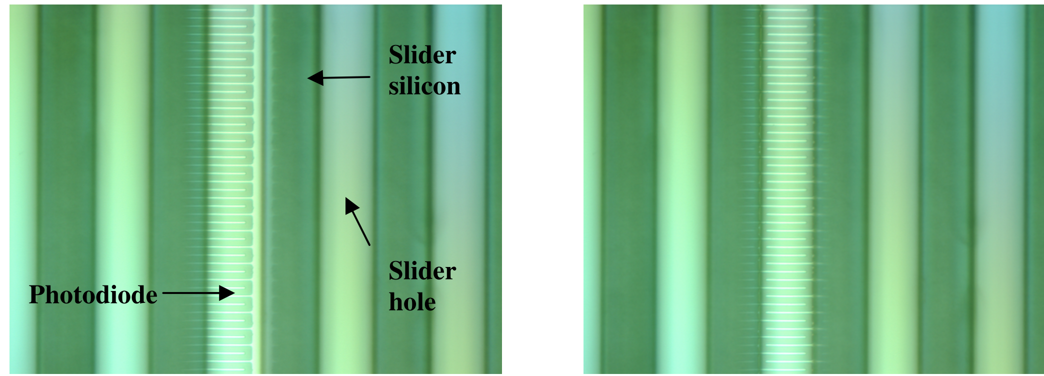

(a) (b)

Figure 3.9. (a) Slider holes on top of a photodiode showing a slight misalignment. (b) A slider hole and photodiode in perfect alignment.

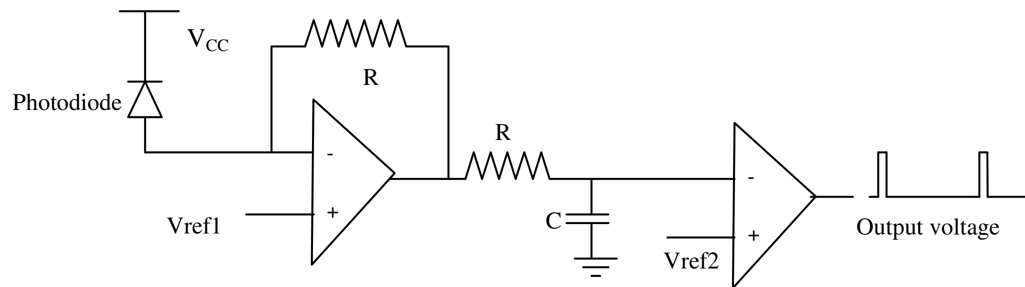

Figure 3.10. Schematic illustration of the circuit for detecting the maximum photodiode current.

Reference voltages in Fig 3.10 were set by considering the required bias for the photodiode and the output current variation. While the state in Fig 3.9 (a) with a slight misalignment of less than 10 µm on a 90 µm wide photodiode results in the circuit to output a low voltage (0 Volt), the full alignment shown in Fig 3.9 (b) results in a binary high voltage output (5 Volts). This shows that there can be less than 11% error in the alignment detection mechanism, which is adequate for the feedback performance.

When the slider travels over the stator, the Si area between the adjacent photodiodes also receives light. If the portion of this area is very close to the reverse biased photodiode electrode, then the diode current may increase. If the partial hole-photodiode alignment is also desired to be detected for a better feedback performance, it

might not be possible to use this design. Therefore second generation photodiodes were designed to alleviate this problem.

3.4 Second generation photodiodes

In second generation photodiodes, the Si surface between the photodiodes was passivated with Al. To achieve this, the mask has been redesigned to include Al blocks covering inactive Si surface and leave a safety distance of 8 μm between the blocks and photodiodes. The overall geometry of the interdigitated structure remained the same. A picture of the fabricated second generation photodiodes is shown in Fig. 3.11.

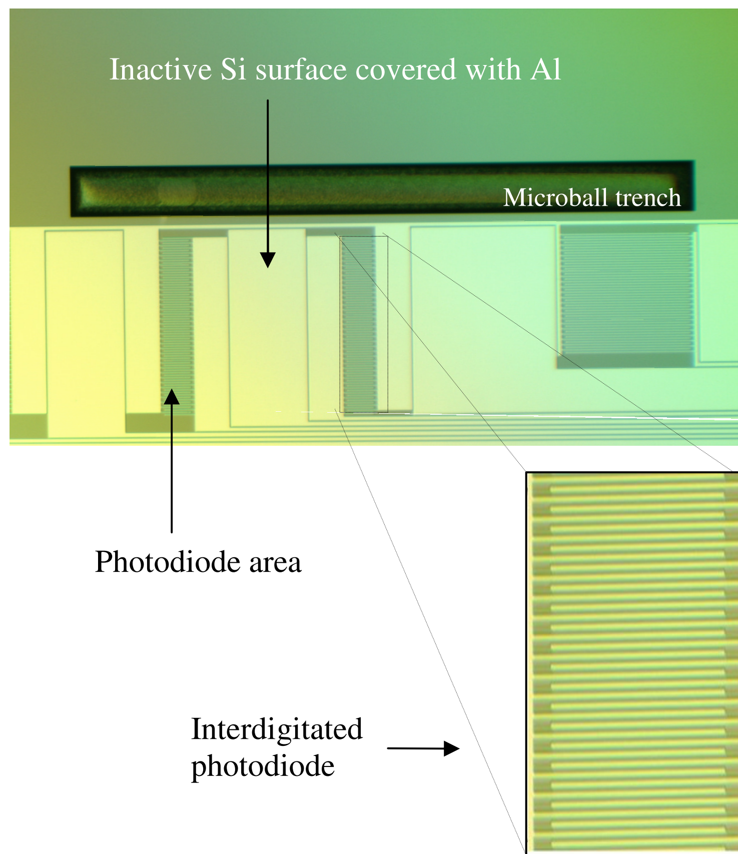

Figure 3.11. Second generation photodiodes with inactive Si surface covered.

The response of the photodiodes is investigated by mimicking the actual operation before implementing this design into the micromotor. In this test setup, stator with only the photodiodes and the microball trenches was fixed to a platform moving horizontally with a sinusoidal velocity. The slider supported on microballs was kept stationary with respect to the ground with a probe, so that a relative motion between the stator and slider is created as in the motoring operation. However in this case, the stator is moving and the slider is stationary. This configuration was designed since it was more difficult to move the slider continuously with a device and keep the stator stationary. During testing, a white light source was provided to shine light on the photodiodes. The schematic of the test setup is shown in Fig. 3.12.

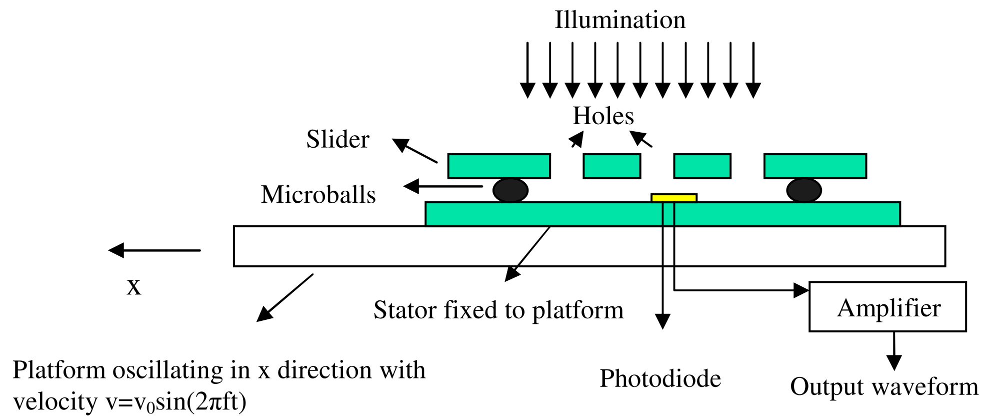

Figure 3.12. Schematic of the test setup.

While the stator was moving, the output photodiode current was amplified and transferred into a voltage waveform by an opamp amplifier. The holes pass over the photodiodes as the stator moves with respect to the slider, fluctuating the incident light in a sawtooth waveform where the slope of the sawtooth depends on the relative speed. The resulting voltage output for 90 μm wide photodiodes is shown in Fig. 3.13.

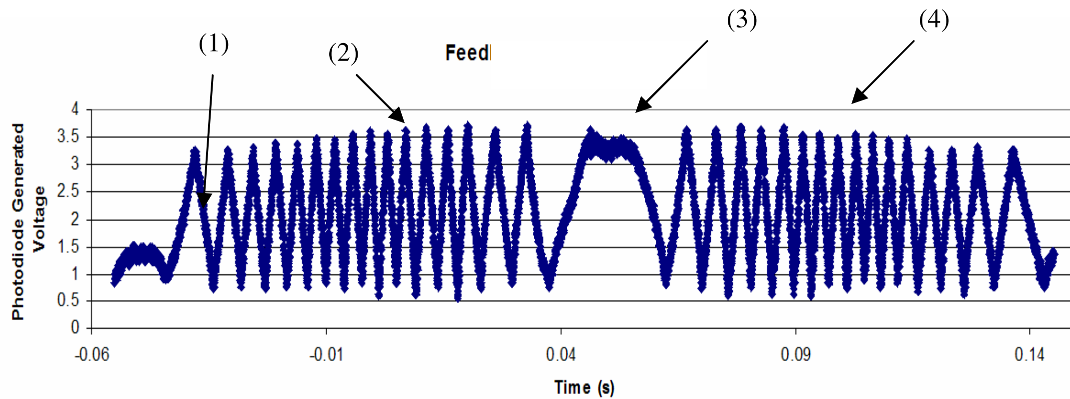

Figure 3.13. Photodiode output when the stator moves sinusoidally with respect to the slider. The photodiodes are 90 µm wide.

Each minimum in Fig. 3.13 corresponds to a full hole-photodiode alignment due to the negative opamp gain. The stator travels two times the electrode width, in this case 180 µm, between two consecutive minimum peaks and the total travel range in one direction is 3mm. Since the motion is sinusoidal, the time between the two peaks corresponding to instantaneous stator velocity also changes sinusoidally. In the region labeled (1) the slider reaches the rightmost end of the track and changes direction to the left. As the slider speed increases, the peaks becomes more dense as shown with label (2). Then the slider slows down and approaches to the leftmost end where it stops and changes direction to the right (3). Next, it speeds up again as shown by (4) and slows down as it approaches to the rightmost point. This graph shows a good agreement between the applied speed and photodiode response, proving the functionality of the sensing scheme.

One feature of the graph is that the peak values change as the stator travels under the slider. The reason is that the light source is also stationary and the stator actually moves with respect to the light source as well. Therefore photodiodes receive different maximum amount of light in time, changing the peak current value. However during the

actual operation, the stator will be stationary and therefore the peak current will not change. Consequently the configuration shown in Fig. 3.10 can be used to detect the maximum alignment conveniently.

3.5 Control System

A feedback system was designed to process the photodiode signals and apply proper voltages to the stator electrode phases. The photodiode readout mechanism is explained above in section 3.2. Using the circuit schematic shown in Fig 3.10, the full alignment information is changed to short binary pulses. These pulses are sent to a programmable microcontroller on which a control algorithm was uploaded. Receiving the pulses coming from the three photodiodes and the circuit, the microcontroller determines the output voltages to be applied to the stator. These voltages are sent to a high voltage amplifier (HVA) and amplified to 90-150 Volts. After amplification, the voltages are applied to the stator by electrical probes. The details about the programmable microcontroller, changes in the circuit for specific tests, and the control algorithm are given in Test Results chapter. Figure 3.14 shows a block diagram of the described system.

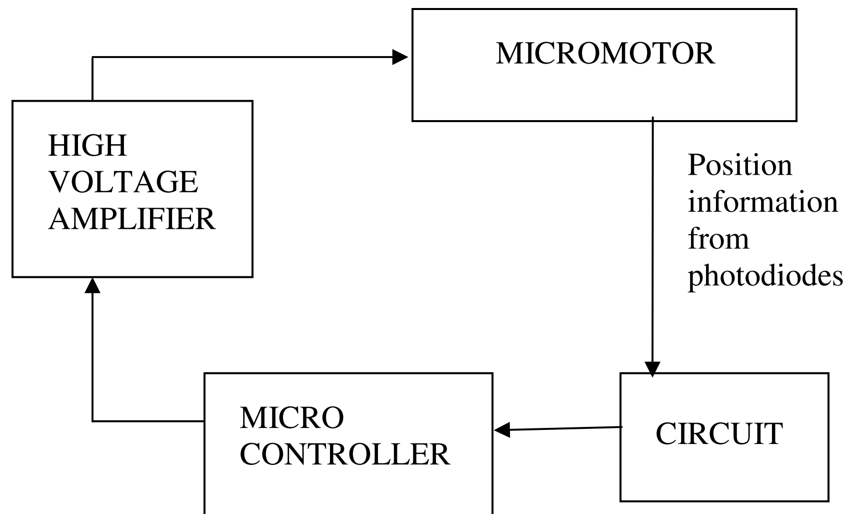

Figure 3.14. Block diagram of the complete system.

The microcontroller used for the feedback system is Texas Instruments MSP430F1612. The algorithm is coded using the C++ programming language on a computer and loaded to the microcontroller using a standard interface adapter.

3.6 Summary

A new micromotor design with a position sensing mechanism is explained. This design uses photodiodes on the stator as position detection elements. In particular, MSM photodiodes are well suited for this application and show adequate responsivity and speed. First and second generation MSM photodiodes are designed, fabricated and tested. Test results confirmed the functionality of the position sensing and alignment detection. A microcontroller and a HVA are used to process the photodiode signals and complete the feedback loop for driving this device in closed-loop fashion.

The next chapter focuses on the integration of photodiodes and through holes into the existing micromotor fabrication process, including the newly introduced process steps. Alternative fabrication techniques are also discussed.

4. Fabrication

The fabrication of the new generation electrostatic micromotor with integrated feedback system is described in this section. For this work, the process flow of the previously developed micromotor has been modified to incorporate the photodiodes and through-holes. The most challenging part of the fabrication is integrating Aluminum (Al), a highly reactive metal, to the existing process. Consequently, new steps to protect the photodiode layer have been introduced to the fabrication increasing the complexity. A total of eleven masks have been used to complete the process. Detailed steps of the process are summarized in table 4.1 and the schematic of the wafer after each fabrication step can be seen in Fig. 4.1. The detailed process recipes are given in Appendix A.

STATOR		
Layer	Process	Details
1) Photodiode	Native oxide etching on the wafer	Wet etching using BOE 6:1 solution
	Aluminum deposition	DC sputtering of 0.3 μm thick Al
	Photolithography	For Al patterning using AZ5214E
	Al etching	Using wet etchant
	Photoresist stripping	Using Aleg 310 at 65°C
2) Alignment marks	Photolithography	For defining patterns using AZ9245 5 μm
	Si etching	RIE
	Photoresist stripping	Using acetone/methanol/IPA
3) First BCB for isolation	BCB deposition	BCB lithography – 3 μm

	BCB soft cure	In oven at 220°C for 40 minutes
	Photolithography	For protecting Al from next steps using AZ5214E
	Descum	RIE of BCB residues
4) Interconnect	Cr/Au deposition	DC sputtering of 0.3 µm thick Cr/Au
	Photolithography	For patterning Cr/Au using AZ9245, 5 µm
	Cr/Au etching	Using wet etchants
	Photoresist stripping	Using Aleg 310
5) Second BCB for isolation	BCB deposition	BCB lithography
	BCB soft cure	In oven at 220°C for 40 minutes
	Photolithography	For protecting Al from next step using AZ5214E
	Descum	RIE of BCB residues
	Photoresist stripping	Stripping using Aleg 310
6) Electrodes	Photolithography	Negative photolithography for liftoff using AZ5214E
	Descum	RIE to remove photoresist residues
	Cr/Au deposition	DC sputtering of 0.3 µm thick Cr/Au
	Lift off	Ultrasonic bath in acetone
7) Third BCB for passivation	BCB deposition	BCB lithography
	BCB soft cure	In oven at 220°C for 40 minutes
	Photolithography	For protecting Al from next step
	Descum	RIE of BCB residues
	Photoresist stripping	Stripping using Aleg 310
8) Trenches	Photolithography	Using AZ9245, 9 µm
	Si etching	DRIE for 135 µm trench

	Photoresist stripping	Uusing acetone/methanol/IPA
	BCB hard cure	In oven at 260°C
SLIDER		
1) Trenches, poles, holes	Photolithography	Using AZ9245, 9 µm
	Si etching	DRIE for 135 µm trench
	Photoresist stripping	Using acetone/methanol/IPA
2) Holes	Backside photolithography	Using AZ9245, 9 µm
	Si etching	DRIE for through holes
	Photoresist stripping	Using acetone/methanol/IPA
3) Wafer dicing	Dicing individual sliders	Using wafer saw
4) Cleaning	Removing residues	Ultrasonic bath in acetone

Table 4.1. Fabrication steps

STATOR FABRICATION

1) Al sputtering

2) Photolithography

3) Al wet etching and photoresist stripping

4) Photolithography

5) RIE and photoresist stripping

6) BCB lithography and soft cure

7) Photolithography for Al protection and Descum

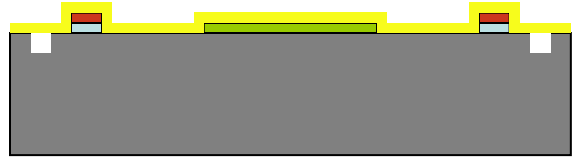
8) Cr/Au sputtering

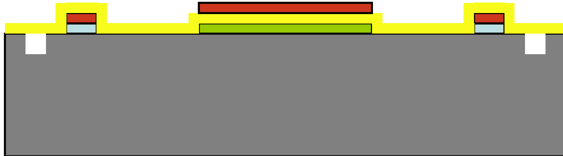
9) Photolithography for patterning Cr/Au

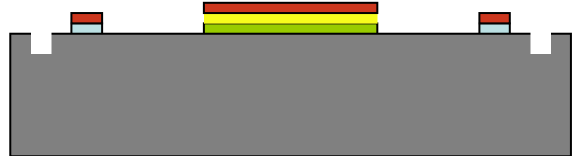
10) Cr/Au wet etching

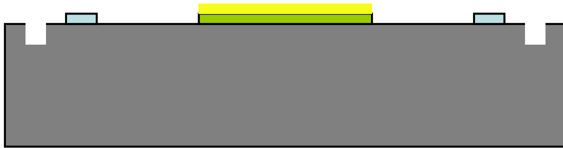
11) Photoresist stripping

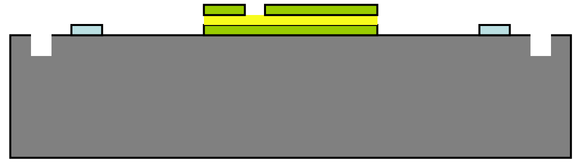
12) BCB lithography and soft cure

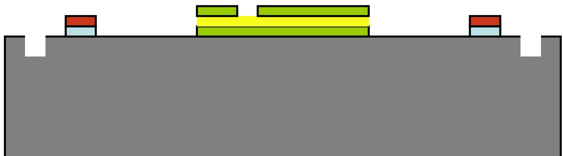
13) Photolithography for Al protection and Descum

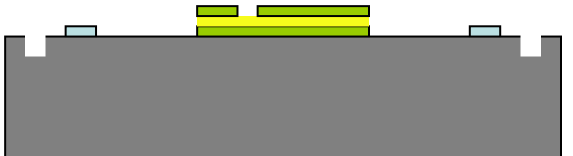
14) Photoresist stripping

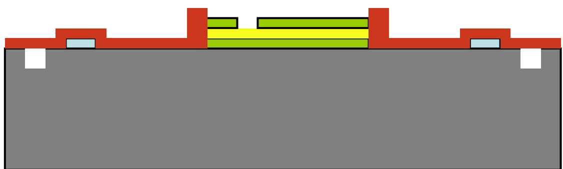
15) Photolithography for liftoff and Descum

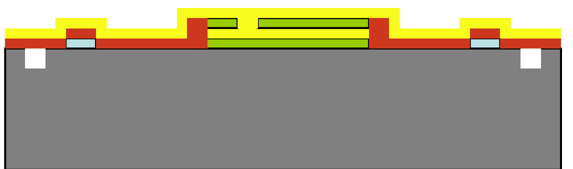
16) Cr/Au sputtering

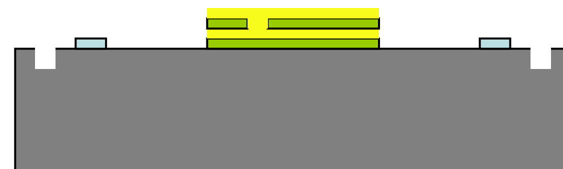
17) Lift off

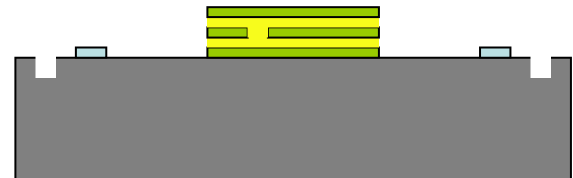
18) BCB lithography

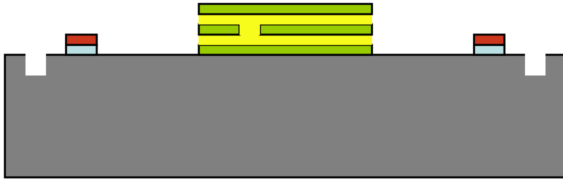

19) Photolithography for Al protection and Descum

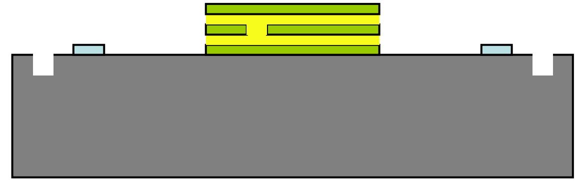

20) Photoresist stripping

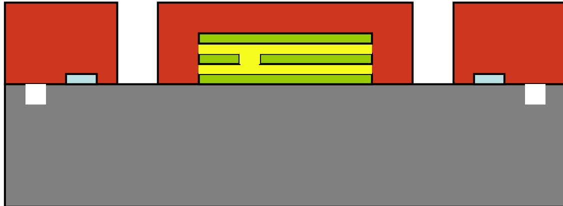

21) Photolithography for trenches

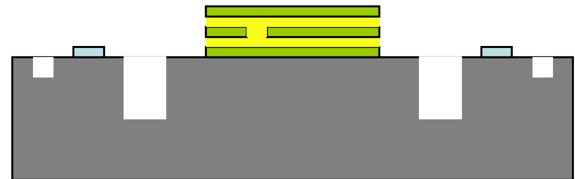

22) DRIE of trenches, photoresist stripping and BCB hard cure

SLIDER FABRICATION

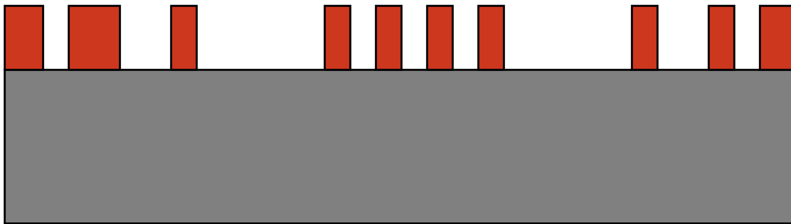

1) Photolithography for trenches, holes and poles

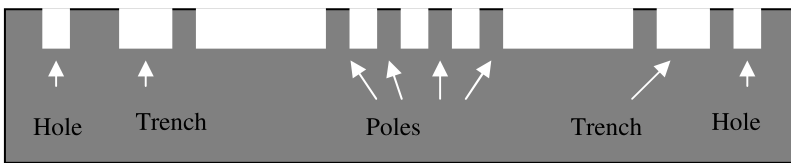

2) DRIE of trenches, holes and poles

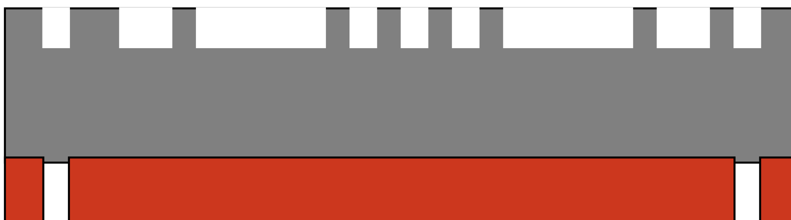

3) Backside lithography for etching holes

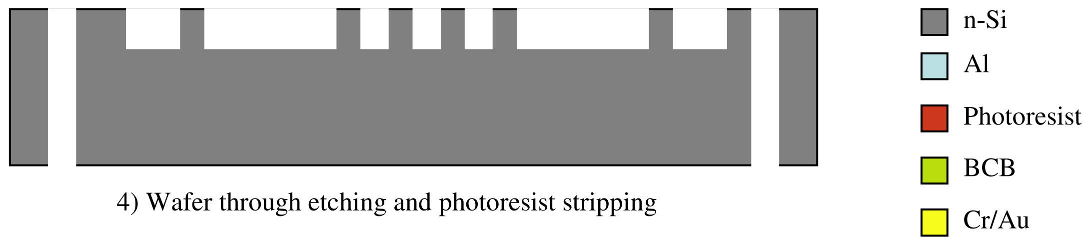

Figure 4.1. Schematics of the stator and slider after each fabrication step. The thicknesses of the layers are not drawn to scale.

4.1 Stator Fabrication

<1-0-0> n type 20-40 Ω.cm Si wafer has been selected as the starting substrate for the type of contact explained in the previous section. Cleanliness of the wafer is very crucial to have a good quality Schottky contact between Al and Si for photodiodes. Therefore fabrication starts with Al deposition and patterning on a new substrate for forming the photodiodes. First, native oxide layer on the wafer is etched using buffered oxide etch (BOE). Subsequently, Al deposition has been performed using DC sputtering method to a thickness of 0.3 µm. The deposition was followed by photolithography using AZ5214E photoresist and wet etching of Al. Figure 4.2 shows a picture of the photodiodes on the wafer after this step. Next, I-V tests described in the previous section have been performed on test structures to examine the quality of the Schottky contacts. The wafers on which the photodiodes worked as expected were selected to continue the fabrication of the micromotor.

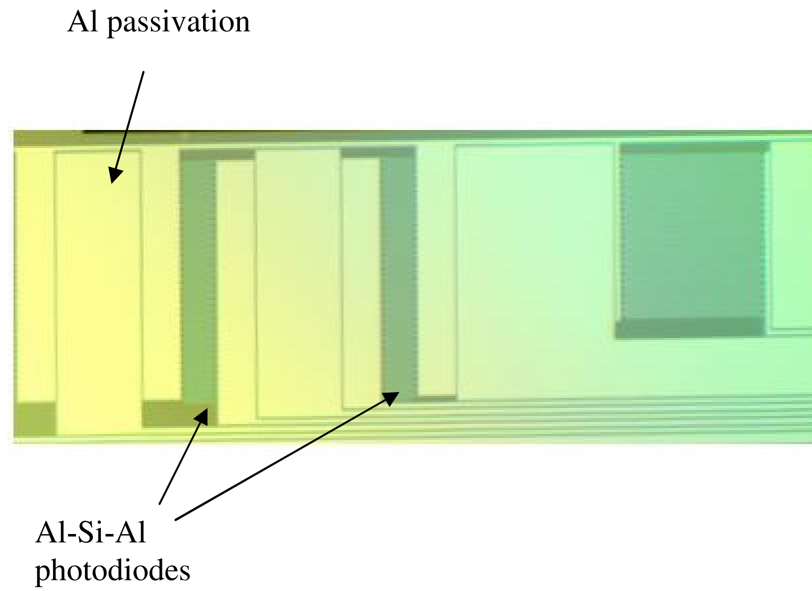

Figure 4.2. Picture of photodiodes and Al passivation to block the light reaching inactive Si surface.

The process was carried on with reactive ion etching (RIE) of the alignment marks on the wafer. All the masks used for the subsequent processes are aligned to these marks inherited from the previous micromotor fabrication, therefore the alignment of these marks to already deposited Al layer is very critical. Any misalignment would show its effect on the position sensing and feedback performance. Figure 4.3 demonstrates the successful alignment of the etched marks and photodiode layer. The marks are 5 μm – 7 μm in depth.

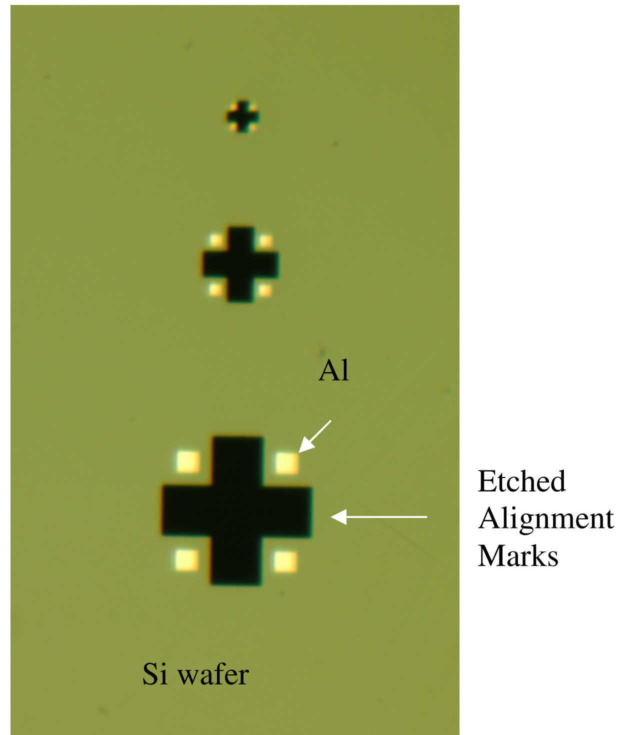

Figure 4.3. Alignment of Al layer and etched marks

RIE of alignment marks is followed by the first BCB layer deposition for the isolation of the interconnect layer from the substrate. BCB is a dielectric that can be patterned using ultraviolet light [77-79, 82]. Therefore BCB features are defined lithographically. The most important parameter in this process is the thickness of the BCB layer. The BCB should withstand the high voltages in the range of 100-150 volts. Also it should not be very thick to maintain the designed 10µm gap between the stator and slider. Reported dielectric breakdown of BCB is 300 V/µm [78] therefore a convenient final thickness of 2-3 µm was chosen for this layer. BCB lithography is followed by the soft curing which is done in a furnace at 220°C in nitrogen environment

[78, 82] for the partial polymerization of the film. Figure 4.4 shows the BCB thin film after the soft cure.

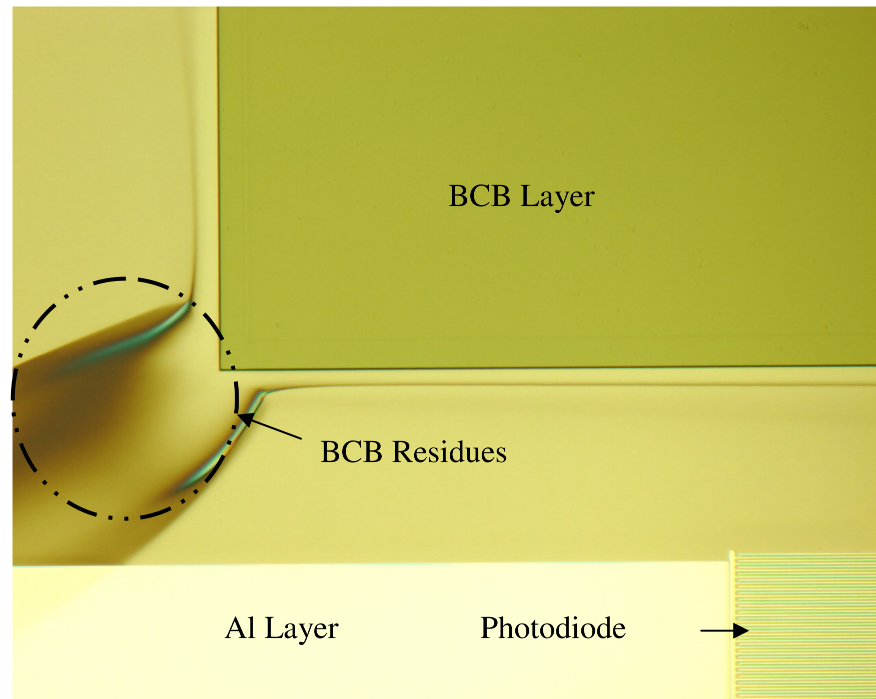

Figure 4.4. Picture of BCB after soft cure. Residues resulting from puddle development are also illustrated.

A short descum in RIE chamber is needed to remove the BCB residues. However descum affects the photodiode performance and increases the dark current drastically. This effect is attributed to the ions getting stuck on the silicon surface during RIE, contributing to the undesired surface currents. If the dark current is already substantial, the increase in photodiode current due to the illumination may become insignificant. Therefore, photodiodes need to be protected from descum step. To achieve this, a lithography step is performed and a photoresist layer is deposited on the photodiodes. This protection lithography is also needed later when the interconnect layer is being

defined, thus the photoresist is maintained on the photodiodes for a few consecutive fabrication steps. Next, Descum is done and first BCB process is completed.

The fabrication is continued with creating the interconnect layer on BCB. This is the layer on which the voltages are carried to the electrodes. In the previous micromotor fabrication, the interconnect layer was fabricated by Cr/Au deposition and wet etching. Since least number of modifications in the fabrication is aimed, the same step is followed. However depositing Cr/Au directly on photodiodes can not be performed since selective etching of Au and Cr is not possible on Al. The photoresist previously spun after the BCB soft cure is used as a protection mask one more time for this reason. 0.3 µm thick Cr and Au is sputtered on the wafer and interconnects are defined by another photolithography done on Cr/Au and wet etching. After the etching, both photoresist layers on Cr/Au and on Al are stripped. A different photoresist stripper, Aleg 310, is used this time since the stripper used in the previous micromotor fabrication, CLK 888, attacks and etches Al layer.

One problem observed at this step is that although a photoresist layer was protecting photodiodes, Al was still etched locally throughout the wafer. This is attributed to the existence of pinholes in the thin Cr/Au layer. During the development of the photoresist on Cr/Au, the developer may have gone through these pinholes and etch the underlying photoresist while Cr/Au etchants may have followed the same paths to etch Al. The picture of these defects is shown in Fig. 4.5.

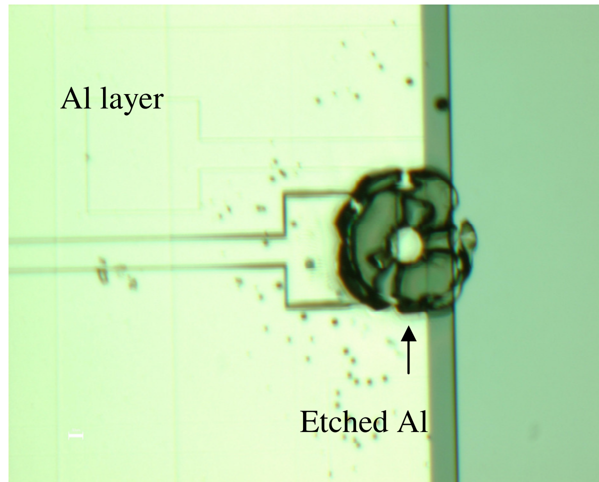

Figure 4.5. Picture of Al layer after Cr/Au wet etching and photoresist stripping. The pads fabricated for electrical connection to the photodiodes were partially etched.

As an alternative to Cr/Au sputtering and wet etching process, lift off could have been preferred and this would not require the protection of photodiodes from Cr/Au deposition and etching. However, this is not recommended [77, 79] as it decreases the interconnect layer fabrication yield.

Next, another BCB layer is deposited on top of interconnect layer for the isolation between this layer and the electrodes. One phase is connected to every sixth electrode through the vias on this BCB layer. The procedure followed here is the same as the first BCB layer except that the photoresist to protect the photodiode layer is stripped after descum since there is no need for protection in the following step.

Subsequently, Cr/Au is deposited to a thickness of 0.3 μm for forming the electrode layer. For patterning, liftoff is preferred over wet etching since previous experiences showed that higher fabrication yield is attained for this layer using liftoff [77, 79]. During this step, photodiodes did not need any protection as mentioned above. Photolithography is performed, Cr/Au is sputtered and liftoff is done to complete

fabrication of the electrode layer. Electrodes are connected to underlying interconnect layer through the vias on the second BCB layer.

A third BCB layer is deposited exactly the same as the second BCB layer for the passivation of the electrodes. This mask could have been changed to passivate the photodiodes as well. However even though the photodiodes were not passivated, no significant change in photodiode current over time is observed during testing. Therefore for the sake of low fabrication cost, integrated photodiodes are not passivated.

The final process of stator fabrication is DRIE of microball trenches. This step is crucial and extra attention has to be paid to the etch depth. The resulting etch dept should yield a final stator-slider gap of around 10 µm. 9 µm thick AZ9245 photoresist is used for lithography to withstand the long DRIE etch. An average etch depth of 134-137 µm was achieved after the DRIE. Next, the stator was put in furnace for 1 hour at 260°C for the completion of polymerization of BCB layers. The wafer is cooled down slowly to room temperature and the stator fabrication is completed.

4.2 Slider Fabrication

The slider wafer has to be highly conductive for the image charges to move from one pole to the next easily. Also the need for backside alignment between the mask and the wafer makes it mandatory to use infrared light during the alignment. When either side of the wafer is not polished, there is a lot of light scattering on the unpolished surface, making it impossible to see back and front surfaces at the same time. Therefore another requirement for the wafer is that it should be double side polished. Due to these

restrictions, slider wafer is chosen to be highly conductive p type double side polished Si wafer.

Slider fabrication starts with the lithography and DRIE to define the trenches, poles and the holes. This step is also very critical for maintaining a 10 μm gap. An average etch depth of 128 μm – 134 μm was achieved after the DRIE. The variation in the etch depth is inevitable throughout the wafer due to the big etch area on the slider wafer (DRIE loading effect).

Next, a photolithography step is performed on the backside of the wafer. Using the infrared view feature of the mask aligner, backside mask is aligned to the front side of the wafer. Another DRIE is performed on the backside and fabrication of the holes is completed. Finally, the sliders are diced using dicing saw and cleaned in an ultrasonic acetone bath. The picture of a complete device is shown in Fig 4.6.

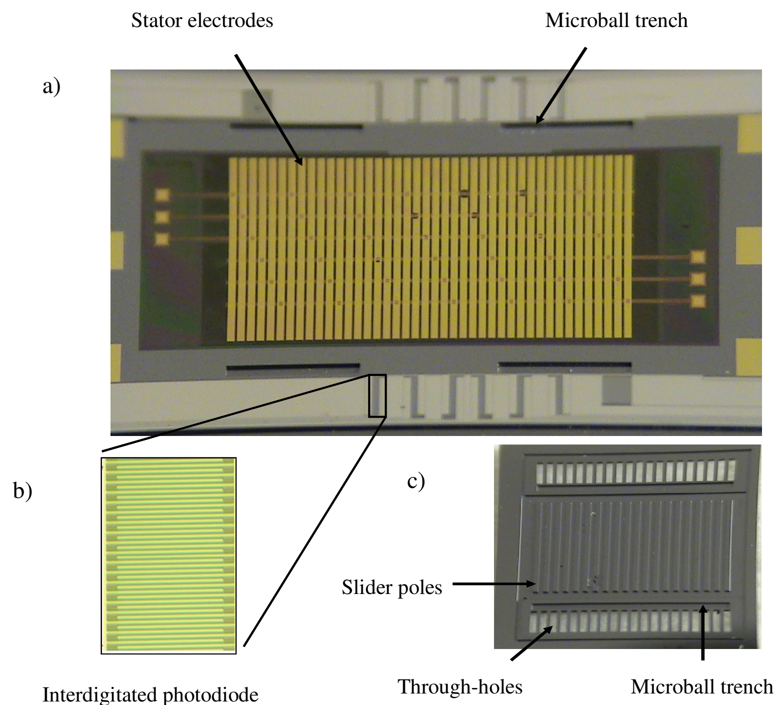

Figure 4.6. Picture of a) fabricated stator, b) close view of interdigitated photodiodes, c) fabricated slider showing bottom view.

Another process flow could have been followed to fabricate the slider. The trenches and poles could have been defined in the first DRIE, as in the previous fabrication, and the whole hole etch could have been performed on the backside DRIE, instead of splitting it between the two DRIE steps. However maintaining a constant hole width through the wafer is very difficult and if not achieved, this could negatively affect the feedback system performance by decreasing position sensing accuracy. Therefore it is more advantageous to etch the holes in two DRIE steps.

After the fabrication, sliders with 30 μm holes were damaged due to the fragility of the Si pieces between the holes and could not be used in the experiments. Therefore all the tests have been performed on 90 μm and 180 μm electrode width designs, as described in Test Results chapter.

4.3 Summary

The fabrication process of the micromotor with integrated photodiodes and holes is explained in detail in this chapter. Process steps, important fabrication parameters are given and alternative fabrication techniques are discussed. The details of the process are provided in recipes in Appendix A. The following chapter discusses the test setup, control algorithms and test results with open and closed-loop configurations.

5. Test Results

This chapter explains the test setup, system operation, and the test results with feedback and closed-loop configurations in comparison to open-loop excitation for the micromotors with 90µm and 180µm electrode widths. The feedback and closed-loop terms are distinguished by the terminology. While the term “feedback configuration” can be used for any kind of system involving feedback signal, closed-loop systems operate based on the error between the desired and current states of the control variable. The use of the closed-loop systems results in a higher performance with smaller settling times and therefore these systems are preferred over basic feedback configurations for implementation. The chapter ends with the summary of the test results.

5.1 Test Setup

The setup consists of photodiode signal processing circuits (amplifiers, comparators, microcontroller) electrically connected to the micromotor system. A picture of the test setup is shown in Fig 5.1 and 5.2 below.

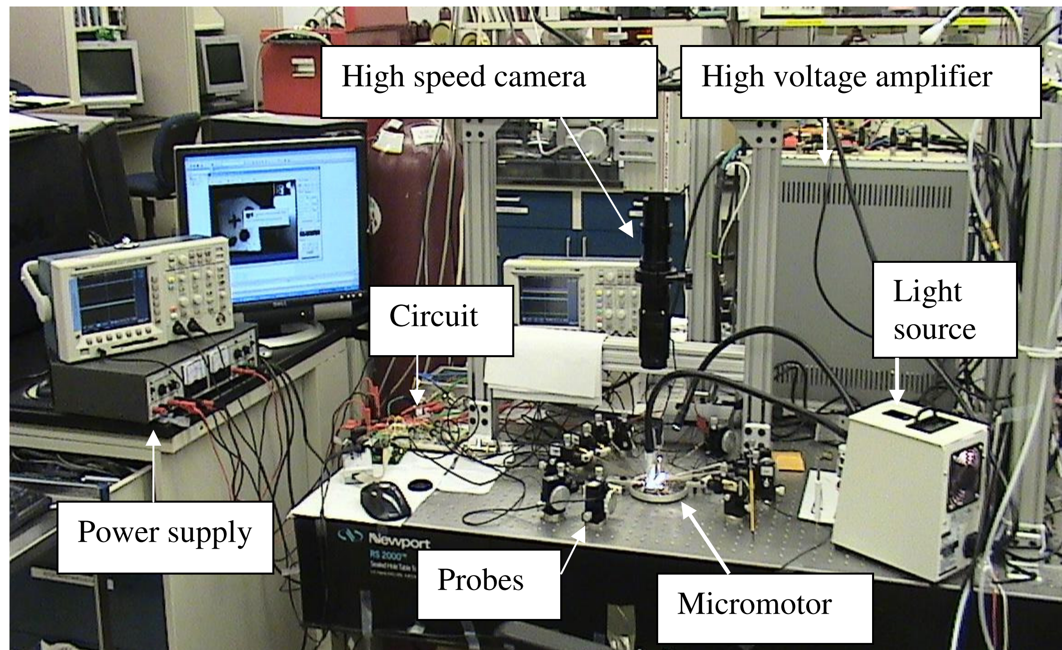

Figure 5.1: Picture showing the individual elements of the test setup.

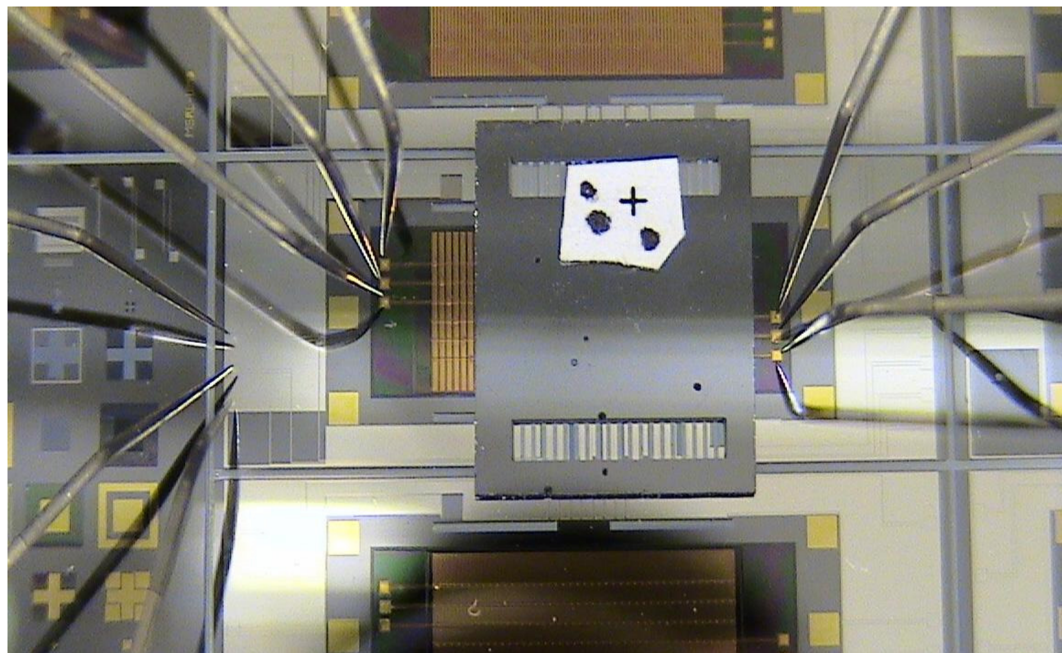

Figure 5.2: Closer view of the micromotor under test.

Ten probes are utilized for the tests. Six of these probes are used for the electrical excitation of the motor and the other four are for the electrical connection to the

photodiodes. One of these four probes is used for the voltage bias to the photodiodes and the remaining three are connected to three photodiodes aligned with the different phases (A,B,C) of the motor. A light source is employed for the illumination of the photodiodes.

The circuit consists of an interface circuit between the photodiodes, a microcontroller, and several opamp amplifiers for the amplification of signals at different stages. The first stage is the opamp transimpedance amplifier which converts the photodiode current variation into a voltage varying typically between 0-6 volts. The maximum microconotroller input voltage is 3.3 volts, therefore there are additional stages between the transimpedance amplifier and the microcontroller to reduce the voltage variation to 0-3.3 volts. These stages differ in feedback and closed-loop configurations and they will be explained in the related subsections. Microcontroller outputs are sent to the high voltage amplifier having a gain value of 15. To make use of the full voltage swing of the high voltage amplifier (0-150 volts), the microcontroller outputs, with a maximum value of 3.3 volts, are pre-amplified by opamp amplifiers with a gain of 3. Finally, the high voltage amplifier outputs are applied to the micromotor electrodes using the probes shown in Fig. 5.1. A picture of the circuit is shown in Fig. 5.3.

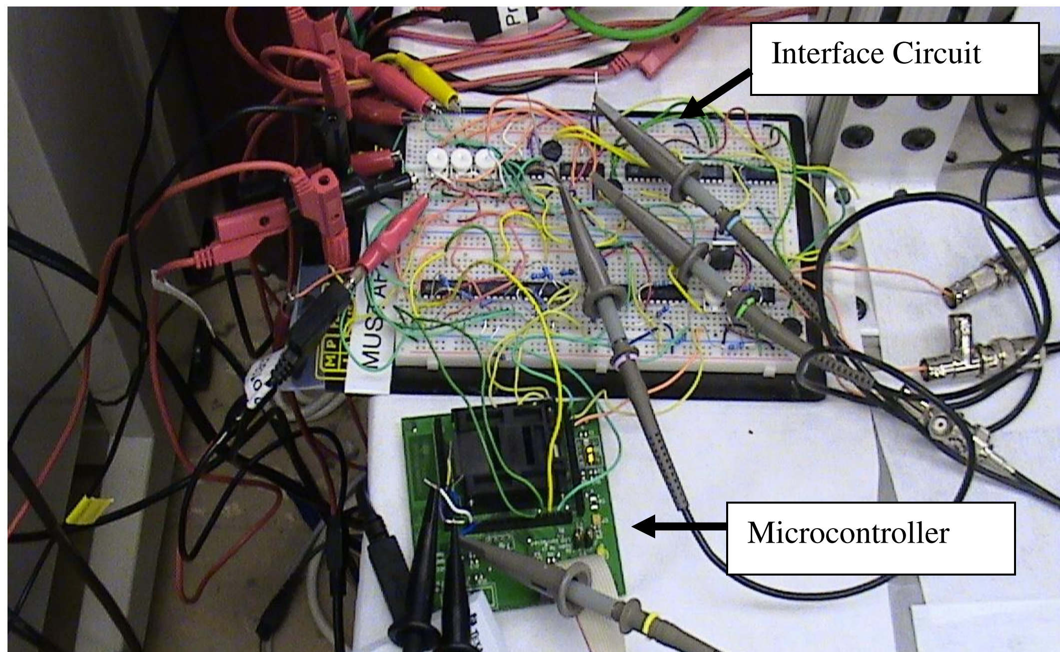

Figure 5.3: Picture of the circuit

The microcontroller used in these experiments is Texas Instruments MSP430F1612. It is programmed using a computer and C++ programming language in combination with IAR Workbench program. While three analog inputs for the photodiode signals are used in all the experiments, the number of microcontroller outputs change in the feedback and closed-loop configurations. This will be briefly discussed at the beginning of each section.

Open-loop tests are performed using the microcontroller ignoring the photodiode signals. On the other hand control algorithms have been implemented to the controller for the feedback and closed-loop designs. In these cases, the microcontroller reads the photodiode signals and reacts according to the designed algorithm. While the motor is running, a high speed camera and an image tracking software is used to independently measure the slider displacement and compare with the desired motor behavior.

5.2 Feedback Configuration

In this configuration, photodiode signals are used to sense the discrete electrode-pole alignments and excite the electrodes. When an alignment is detected for one phase, the microcontroller turns off the voltage applied to that phase and turns on the voltage for the next phase using the control algorithm. Therefore, the continuation of the motion depends on the alignment events.

A set of comparators are used to digitize the alignment information from the photodiodes for this system as shown in Fig. 3.10. When the photodiode current is at its maximum, corresponding to maximum alignment, the comparator associated with that photodiode gives a binary high signal of 1.5 volts. This signal is input to the microcontroller, informing the microcontroller about an alignment with the corresponding phase. According to the algorithm designed for different tasks, the microcontroller makes decisions for the six outputs going to the motor phases A, B, C, D, E, and F. The voltages applied to the micromotor are 150 V p-p 33% duty cycle square waves (phase A,B,C: 0 to +150 V, phase D,E,F: 0 to -150 V and phases are such that D=-A, E=-B, F=-C). The frequency of the applied sequential voltages determines the stepping speed.

5.2.1 Position Feedback

This experiment is intended for proving the functionality of the system and shows the mechanism described above. In this experiment, the micromotor is desired to be moved in discrete steps for different number of steps at different stepping speeds in two directions, forward and backward, periodically. To put more variety in the motion, the

slider is kept stationary for a short period of time when the direction is switched from forward to backward only.

A program written in C++ language is developed for this experiment. In this algorithm, the microcontroller constantly looks for alignment signals coming from the photodiodes and comparators as explained above. Receiving a phase alignment signal, the controller decides on what phase to be excited next according to the number of steps desired to be taken in each direction. Next, the system enters in a delay state for the slider to settle down on the excited electrode. The duration of this delay state determines the stepping speed. If the direction is switched from forward to backward, there is an additional delay state the system enters. Photodiode signals are ignored during these delay time intervals. Finally the controller exits this state and returns to the initial state where it expects alignment signal from the previously excited phase. Figure 5.4 shows the basic logic flow diagram of the algorithm. The complete program is given in appendix B.

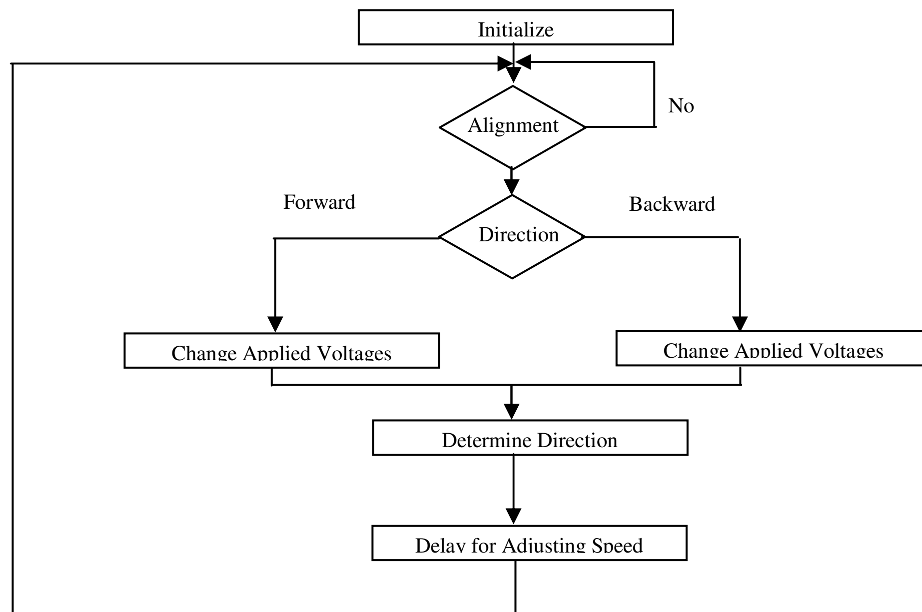

Figure 5.4: The logic flow for position feedback.

The algorithm runs the slider 4 steps forward at 1.5 steps/s, stops it for 2 seconds and moves it backward 3 steps at 4 steps/s. The resulting motion for the micromotor with 180 µm wide electrodes is shown in Fig. 5.5 below.

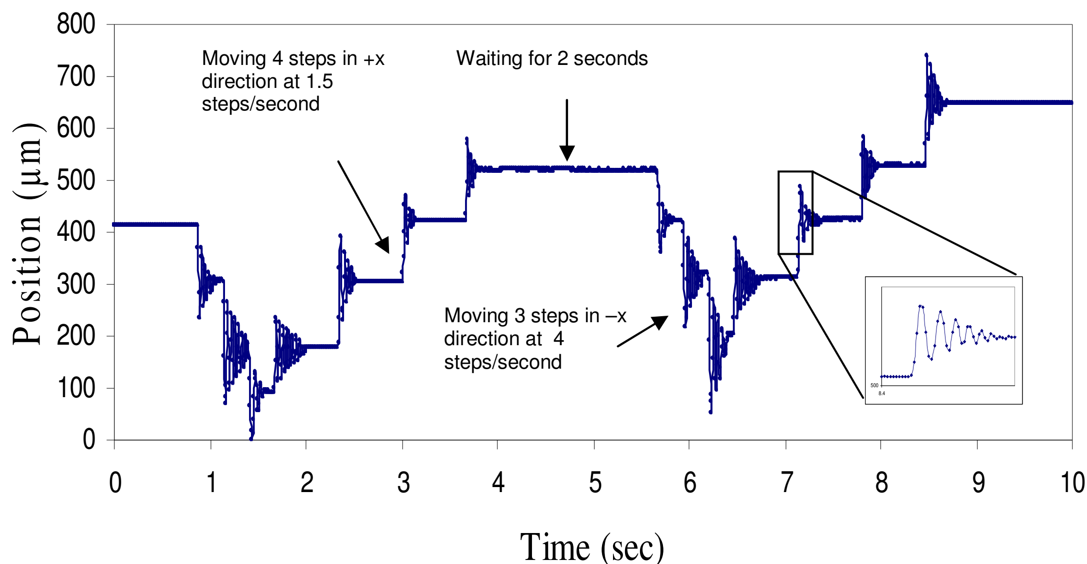

Figure 5.5: Slider motion with position feedback algorithm for 180 µm electrode design.

The slider follows the algorithm as shown in Figure 5.5, proving the successful use of the feedback signals. Every step in the graph corresponds to one electrode-pole alignment and the device inherently takes steps of the two thirds of electrode width, 120 µm in this case. The photodiode signals and microcontroller voltage outputs resulting in this motion are given in Fig. and Fig. 5.7 respectively.

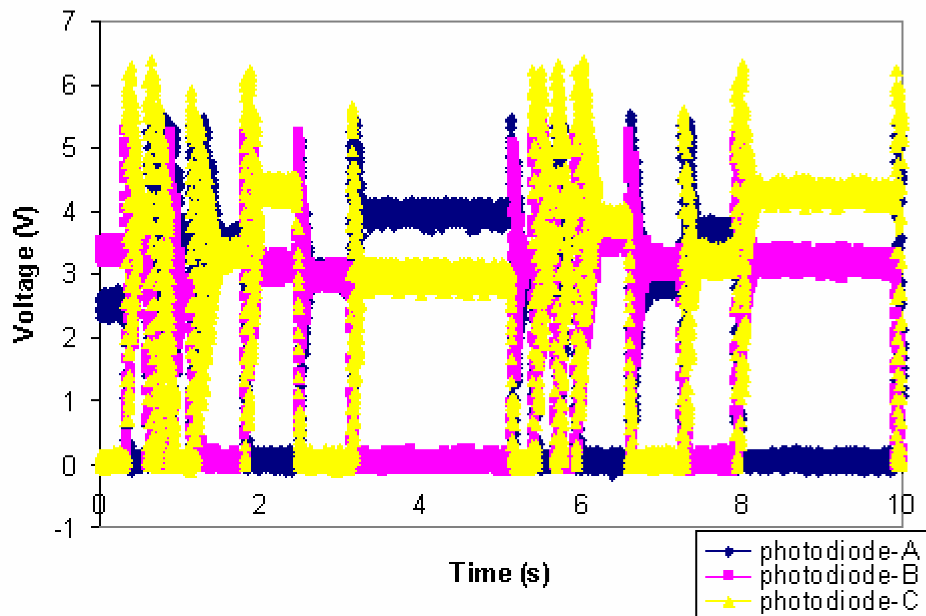

Figure 5.6: Photodiode signals during the motion

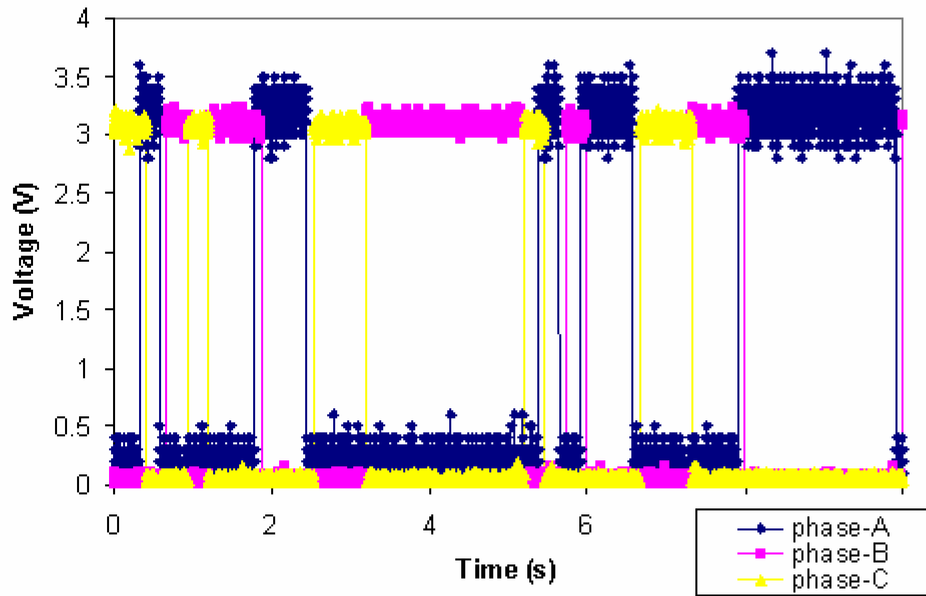

Figure 5.7: Corresponding microcontroller output voltages.

It can be seen in the Fig. 5.6 that the photodiode signals have 120° phase difference that is equal to the phase difference between electrode phases. When a

photodiode and a hole align, the photodiode output voltage goes to zero. However when there is misalignment, the voltage goes up to a value between 0 and 6 Volts. The voltages at discrete misaligned states (corresponding to each step) of the photodiodes are different due to the amount of light they receive and their slightly different characteristics. However this difference does not affect the feedback performance since these voltages are compared to a very low voltage value (0.4 volts) by comparators and the binary result is sent to the microcontroller. Also since the data acquisition is not synchronized with the camera and the oscilloscope, there is a slight delay between the voltage data and the motion in Fig. 5.5.

The microcontroller outputs are 0-3 volts square waves as seen in Fig. 5.7. As explained previously, these voltages are amplified to 150 volts (for phases A, B, C) and -150 volts (for phases D, E, F) using a HVA and applied to the six phases of the motor.

Oscillations in slider motion after each step are observed (Figs. 5.5 and 5.6). These oscillations result from the electrostatic spring force exerted by the excited electrodes on the slider poles. The friction is not enough to over damp (or critically damp) the motion. Therefore, the slider goes back and forth over the excited electrode until it loses its kinetic energy against the friction force and settles down on the equilibrium point. Similar oscillations are also observed in the micromotor with 90 µm electrode width as shown in Fig. 5.8. Each step in this motor is 60 µm long which is again two thirds of the electrode width. Since the photodiode signals and microcontroller outputs look similar, they are not shown for the rest of the Feedback Configuration section.

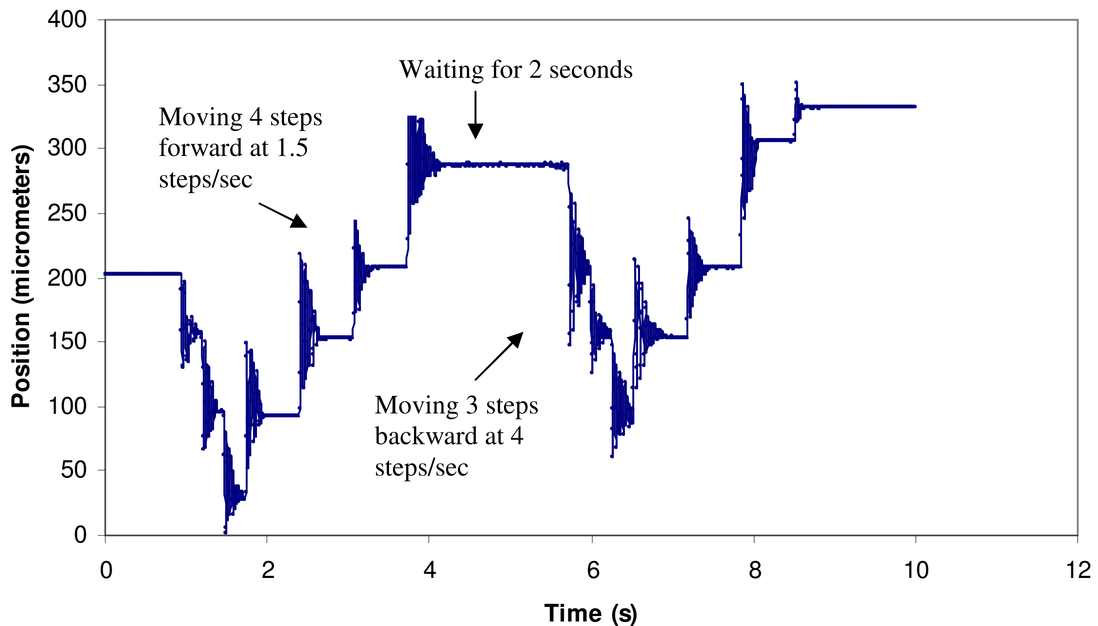

Figure 5.8: Slider motion with position feedback algorithm for 90 μm electrode design.

As the stepping speed is increased for both of the designs, the oscillations start to affect the uniform motion severely. If the next electrode is excited before the slider settles down, the slider starts to move to the next electrode with an initial kinetic energy which prevents the slider to stop or oscillate around the new equilibrium point. This kinetic energy results in the slider to pass the next electrode and stop on another one, resulting in loss of synchronization and control over the motion. The next subsection describes the use of the feedback signals to avoid the loss of synchronization in such cases.

5.2.2 Acceleration and Critical Speed Detection

This experiment aims to detect the oscillations in the motion using the photodiode signals to adjust the speed such that the critical speed that results in the loss of

synchronization is never exceeded. Two algorithms have been developed to accelerate the slider from rest with and without the photodiode feedback signals. The acceleration without the feedback configuration is simply based on increasing of the output voltage frequency, on the other hand the algorithm that uses the photodiode signals is fairly complex. In short, the microcontroller looks for the sequence of the photodiode alignments for detecting the oscillations while increasing the output voltage frequency for speeding up the slider. If these oscillations do not vanish before the next signal is applied, the frequency is not increased anymore and kept constant to avoid crossing the stability limit. Figure 5.9 shows the resulting slider motions with and without using the feedback signals for 180 µm electrode design.

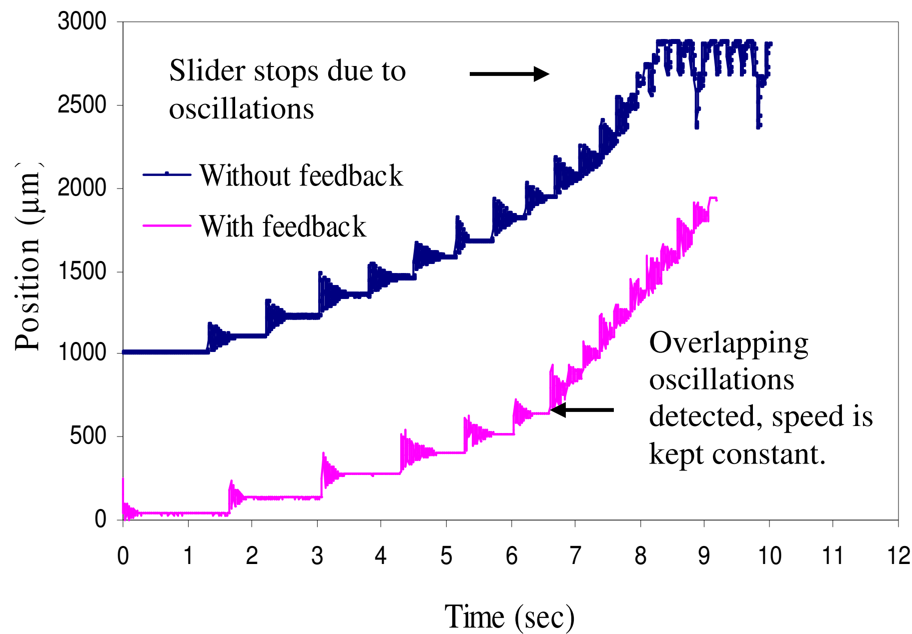

Figure 5.9: Acceleration of the slider with and without the feedback signals for 180 µm electrode design.

The parabolic section of the position versus time graph corresponds to the acceleration. As it can be seen from the graph above, the constant acceleration with open-

loop excitation results in the slider to lose synchronization and eventually stop. On the other hand, the microcontroller detects the oscillations and stops the acceleration automatically using the photodiode signals as feedback. The speed is kept constant for the rest of the motion. Using this method, the highest speed was measured to be 0.5 mm/s. Figure 5.10 shows the acceleration of the slider using the photodiode feedback signals for the 90 μm electrode design at 150 volts. The maximum speed was measured to be 0.15 mm/s for this micromotor design.

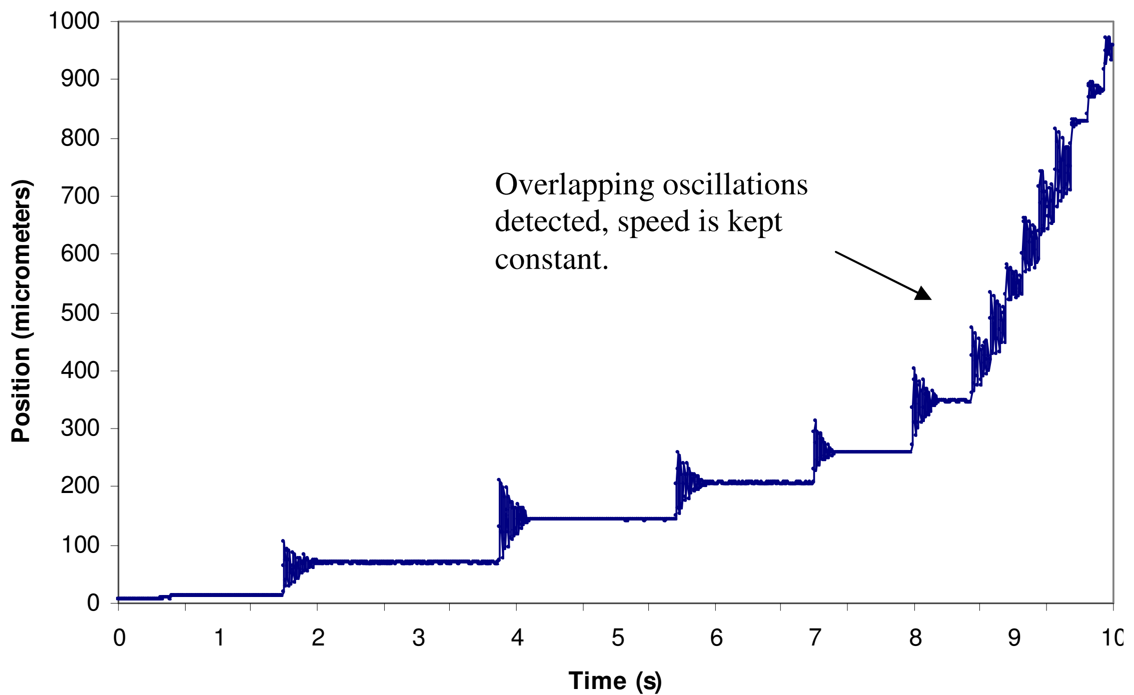

Figure 5.10: Acceleration of the slider at 150 volts for the 90 μm electrode design.

5.2.3 Overcoming Friction Barriers

It is occasionally observed that the slider can not continue its motion in one direction even though the excitation is applied. This is attributed to the increase in the friction that may be due to several effects (the wear profile of the trench, surface

roughness, balls located at the end of the trench, etc…). Feedback configuration is used to solve this problem. An algorithm to sense these friction barriers and change the voltage sequence is developed. The algorithm applies necessary voltages and tracks the slider using the photodiode signals. If an alignment signal is not received from the photodiode position sensor of the excited phase, this shows that the slider is stuck somewhere on the way between the previously and newly excited electrodes. Then the slider is pulled back one step and sent forward again. This loop continues until the slider goes over the barrier and continues its motion. Figures 5.11 and 5.12 show how the slider reacts to such barriers when feedback system is used in motors with 180 μm and 90 μm electrode designs respectively.

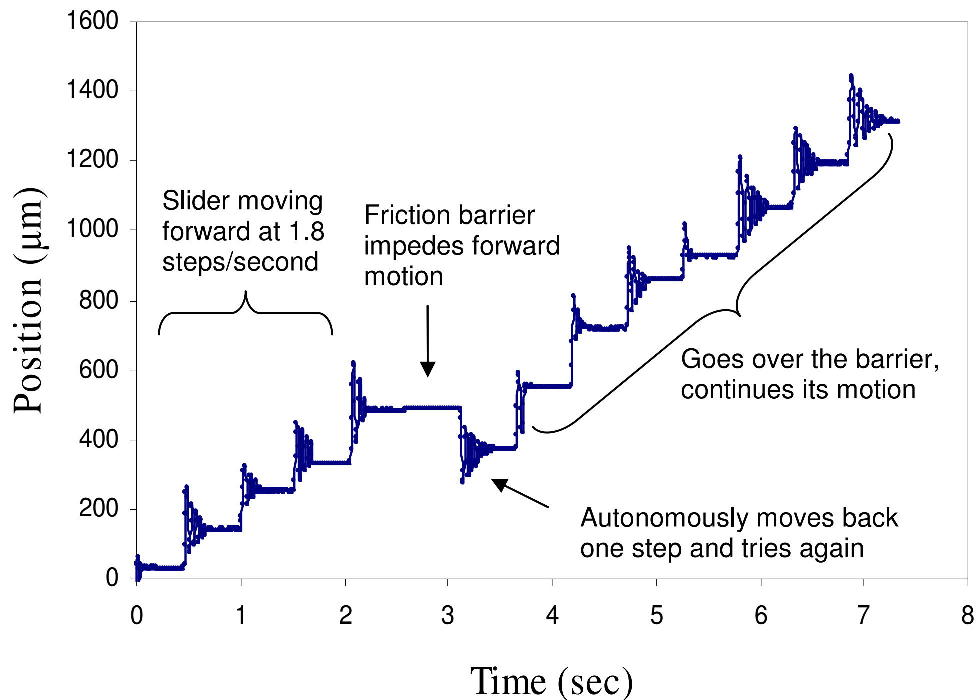

Figure 5.11: The slider response to friction barriers for 180μm electrode design.

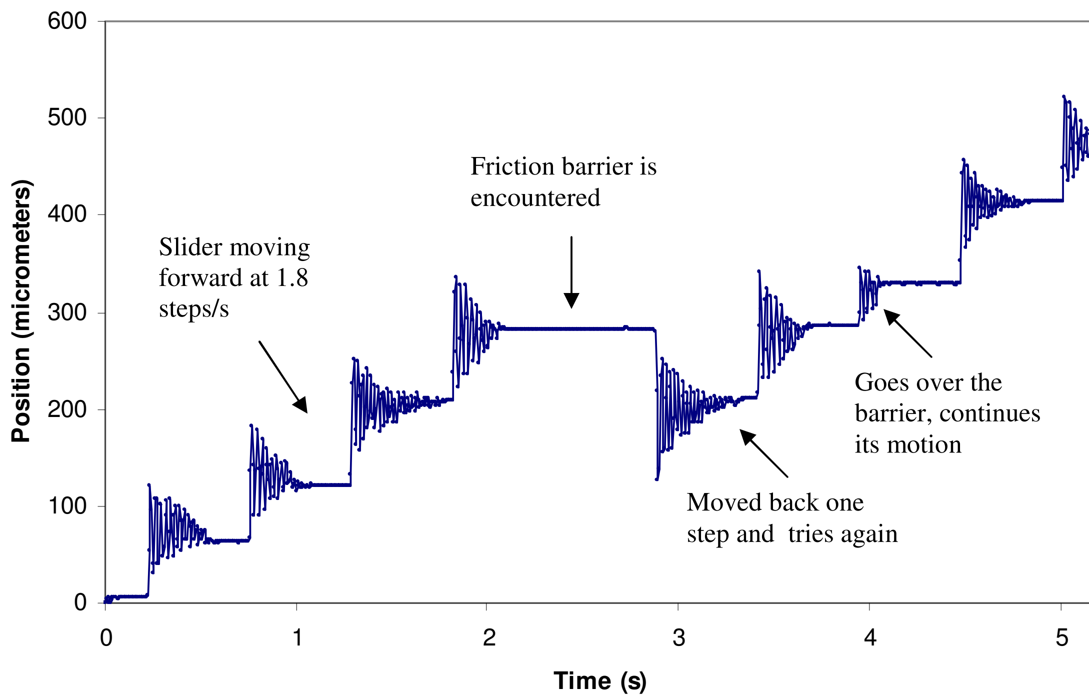

Figure 5.12: The slider response to friction barriers for 90µm electrode design.

The slider is observed to meet these barriers usually on an electrode rather than between electrodes as it can be seen from the graphs. However, this algorithm also works when the slider gets stuck between the electrodes. Using this system, the motor can autonomously change the excitation sequence and overcome friction barriers when the friction force is still low enough to be overcome by the electrostatic force.

5.3 Closed-Loop Position Control

Closed-loop systems operate based on the error between the desired and current value of the control variable of interest. If implemented with correct control parameters, these systems improve the system performance in terms of settling time, speed, and reliability which are important factors for a micropositioner. Therefore closed-loop

position control is implemented in the micromotor by changing the interface circuit and the controller algorithm. Proportional control law is used for the sake of low algorithm complexity.

5.3.1 System Operation

For this system, the interface circuit between the photodiodes and the controller is changed slightly. Comparators are eliminated from the circuit and photodiode signals are amplified with a gain of less than 1, making the maximum photodiode feedback signal voltage slightly less than 3.3 volts. This allows these signals to be input to the microcontroller directly. The photodiode signals are not ignored at any given time, enabling the microcontroller to calculate the position relative to the starting point and calculate the error between the measured and desired distances. Another change in the system is that, sinusoidal waves are used instead of 33% duty cycle square waves to create additional damping and achieve smoother motion. The frequency of the three-phase sinusoidal waves determines the slider speed. The available two analog and one digital outputs of the controller together with a DAC (digital to analog converter), made by an opamp and several resistors, are used to create sinusoidal waves. Figure 5.13 shows the system diagram.

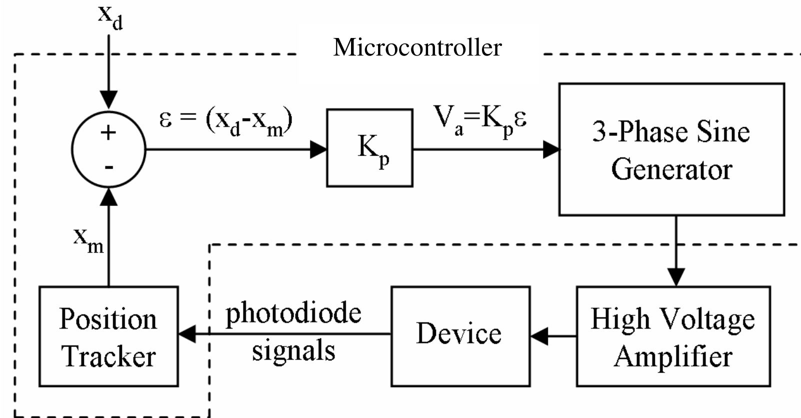

Figure 5.13: Closed loop position control system diagram, where x_d is desired position, x_m is measured current position, V_a is speed, K_p is proportional constant and ε is error. Position tracker, K_p, and 3-phase sine generator are parts of the code implemented in the controller. The circuit composed of several amplifiers between the photodiodes and the microcontroller is not explicitly drawn.

The closed-loop position control system works as follows: The microcontroller generates three phase sinusoidal voltages using a subprogram in the code and modifies the frequency, that determines the slider speed, based on the error between the measured and desired distances. By tracking the photodiode alignment signals, the current position is measured and subtracted from the desired position value. The system can also measure the position of the slider when it is not aligned with any of the phases. However there are unresolved issues with noise and microcontroller capability that limits the accuracy of the measurement. Therefore the microcontroller updates the speed when there is a full alignment between the slider poles and one stator phase for maintaining the reliability of the control system. When one photodiode signal goes to zero (full alignment state), the frequency of the signals is decreased by an amount equal to the multiplication of the proportional value, K_p, and the decrease in error to reduce the speed. As the slider approaches to the target, the speed goes to zero. The code written for this algorithm is given in Appendix B.

5.3.2 System Step Response

The system response to a desired step in position is characterized for different step heights at different voltages for motors with 180 μm and 90 μm electrode designs. The term "step" refers to a travel distance, rather than individual steps that the slider takes. Since this is a stepper motor, the traveling distances are in multiples of slider step sizes which are 120 μm for 180 μm electrode design and 60 μm for 90 μm electrode designs. Figure 5.14 shows the slider motion for a desired traveling distance of 1080 μm for 180 μm electrode design with a K_p value and voltage of 16 and 150V respectively.

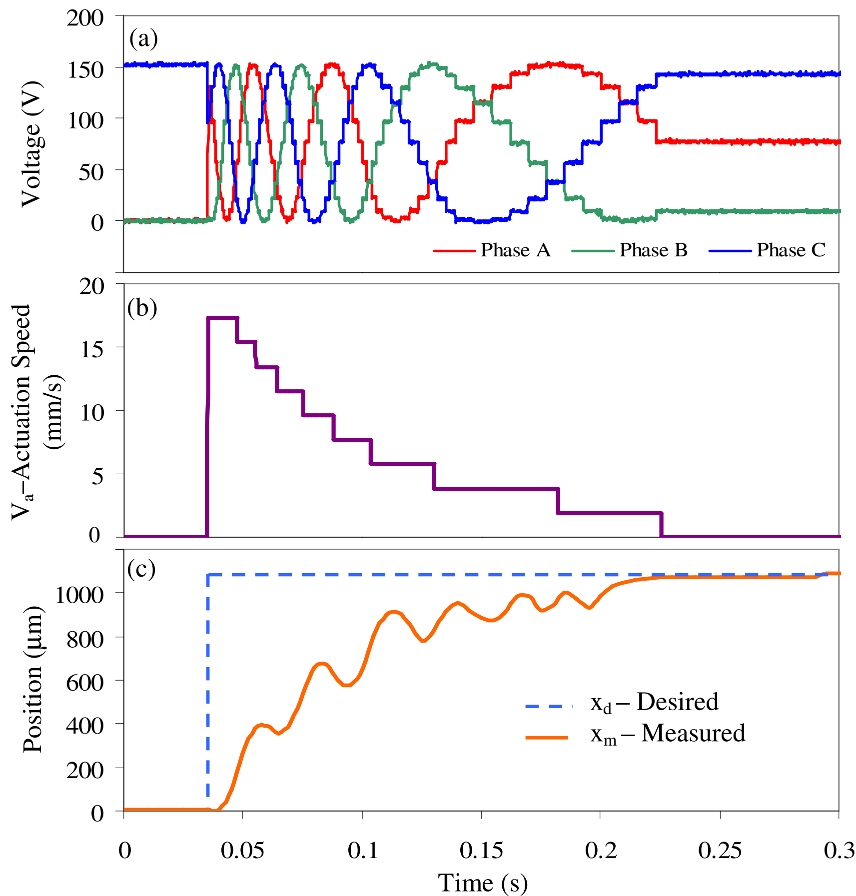

Figure 5.14: (a) Three phase sinusoidal microcontroller output voltages, (b) calculated slider speed, (c) slider motion tracked by the camera. All three graphs have the same time scale, K_p is set to be 16, and peak sinusoidal voltage is 150 volts. The micromotor used in this experiment has 180 μm wide electrodes.

The sinusoidal microcontroller outputs shown in Fig 5.14 (a) are not perfectly smooth since the microcontroller does not have infinite analog output resolution. The voltages could have been made smoother however the trade off would be the decrease in the highest output frequency. In this configuration, the full sinusoidal wave is divided into 24 discrete levels and the smallest period of the two adjacent sinusoids is 5.85 ms, or 171 Hz.

Figure 5.14 (c) shows the desired and resulting positions. At time equals 0.04s, the desired position goes to 1080 μm and the current position is 0. This triggers the control system to start applying forward excitation. Since the error at this time instant is large, the initial applied frequency and the corresponding speed is high as it can be seen in Fig 5.14 (a) and (b). As the slider moves forward, the error goes down. As a result, the applied frequency and the speed decrease. The general trend of the slider displacement shows this decrease in the speed. Finally the slider settles down on the desired position and the frequency is set to zero, showing successful closed-loop control on the position.

The discrete nature of stator electrodes, discrete changes in the applied frequencies and random friction behavior are believed to cause the instantaneous change in the direction of the slider. However, these do not represent loss of synchronization as the slider follows the excitation throughout the entire motion, and the amplitude of the reverse movement is relatively small. Same experiment has been repeated for different K_p values and the results are illustrated in Fig. 5.15.

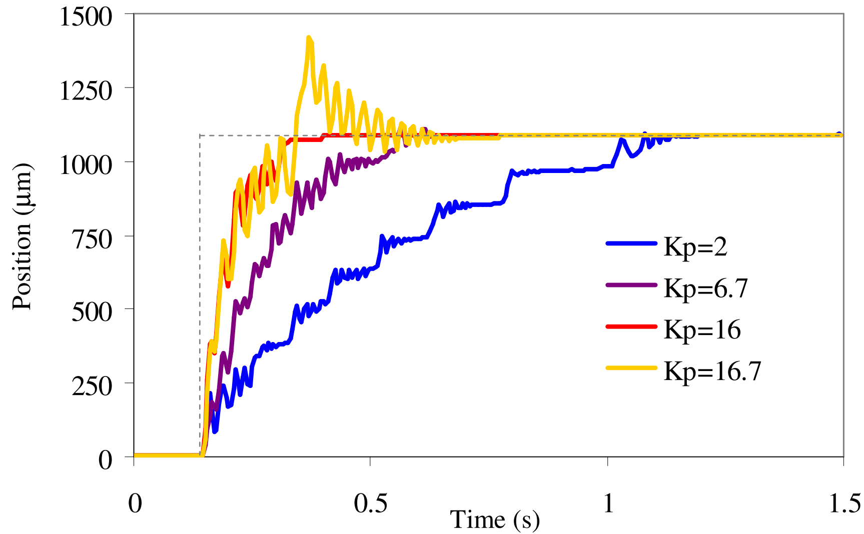

Figure 5.15: Slider trajectories for a desired displacement of 1080 µm for different K_p values at 150 volts sinusoidal peak voltage. The micromotor used in this experiment has 180 µm wide electrodes.

The slider overshoots for K_p values higher than 16 and the synchronization is lost for the K_p values greater than 16.7. The maximum synchronous speed that the slider can follow without an overshoot for the given traveling distance is calculated to be 17.28 mm/s and the initial instantaneous speed was measured to be 19.5 mm/s. For low K_p's, the individual slider steps corresponding to each electrode-pole alignments can be seen as the slider moves. One important fact to notice is that the oscillations are less pronounced. This is a direct result of additional electrical damping created by continuous sinusoidal voltages.

Settling time is defined to be the time it takes the slider to settle down within 10% of the desired position. The settling times for different K_p values for the motor with 180 µm electrodes traveling 1080 µm are shown in Fig. 5.16.

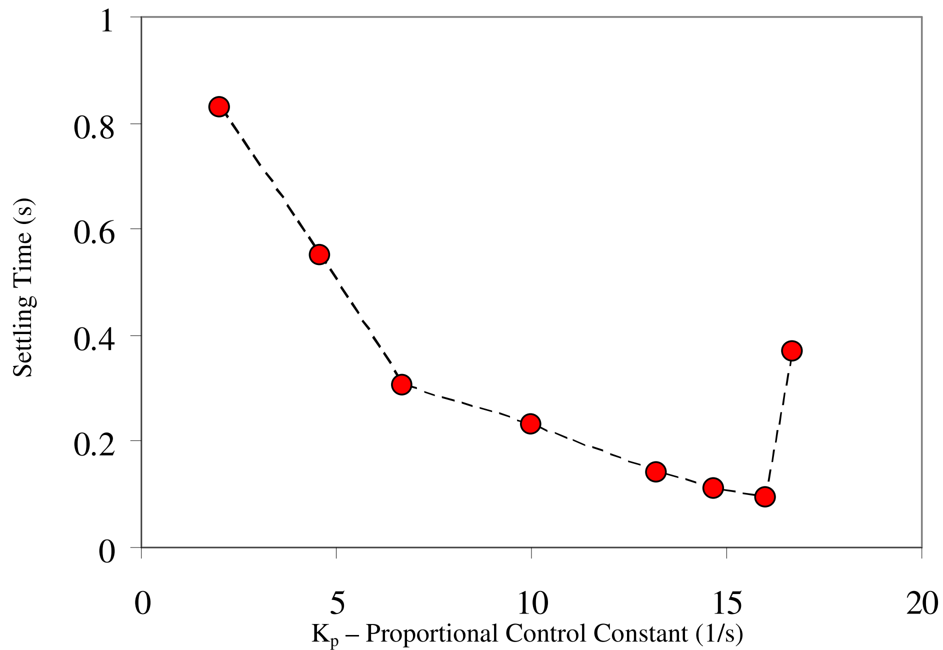

Figure 5.16: Settling time versus for K_p for 180 µm electrode design traveling 1080 µm at 150 volts peak sinusoidal voltage. The micromotor used in this experiment has 180 µm wide electrodes.

As it can be seen from the Figure 5.16, the settling time decreases until the slider starts to overshoot. Although the slider finally settles down on the desired point for the values of K_p greater than 16.7, the measured settling times do not show repeatability due to the loss of synchronization and unpredictable slider behavior.

A typical slider response to a desired traveling distance of 1080 µm for the motor with 90 µm electrodes at an applied sinusoidal voltage with 150 volts peak value for a K_p of 10 is shown in Fig. 5.17.

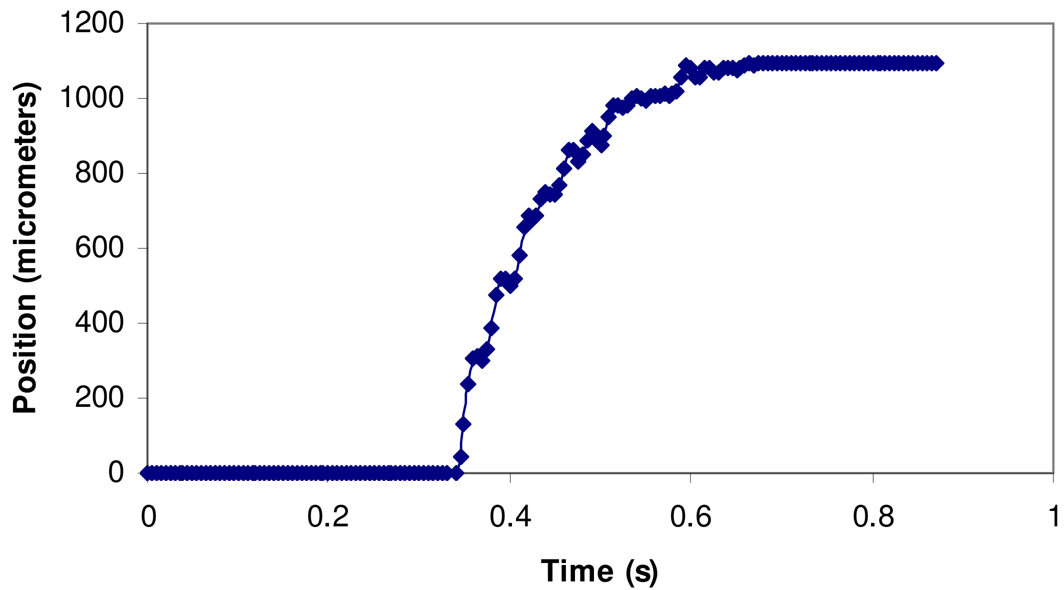

Figure 5.17: The slider response to a desired traveling distance of 1080 μm for a K_p of 10 at an applied maximum peak voltage of 150 volts. The micromotor used in this experiment has 90 μm wide electrodes.

The maximum synchronous speed and the settling time are 10.8 mm/s and 0.17 s respectively for this motor. This experiment is performed at the highest frequency the microcontroller could output, therefore K_p values greater than 10 could not be tested. It is believed that the slider for this motor design could be moved faster than 10.8 mm/s and that smaller settling times are achievable. The motion is smoother for this motor and the amplitude of reverse movement is smaller due to the narrower electrode design (90 μm wide).

The same tests have been performed on the two motor designs for different K_p values for different traveling distances at various peak voltages to study the motor characteristics and find the optimal operating parameters. Figures 5.18, 5.19, and 5.20 show the settling time versus K_p graphs for the motor with 180 μm electrodes at various traveling distance and voltage combinations.

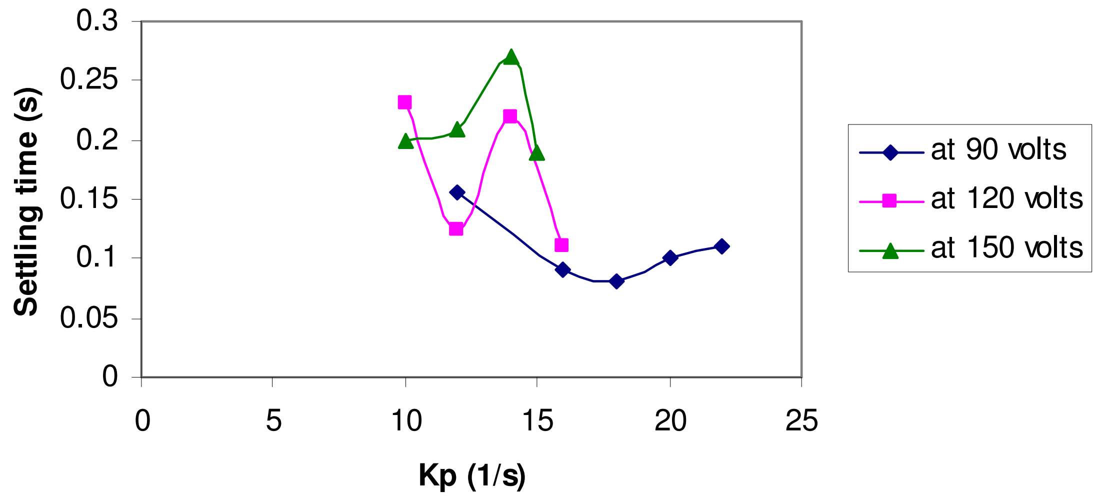

Figure 5.18: K_p versus settling time curve for 180 µm electrode design at different voltage values for 360 µm travel distance.

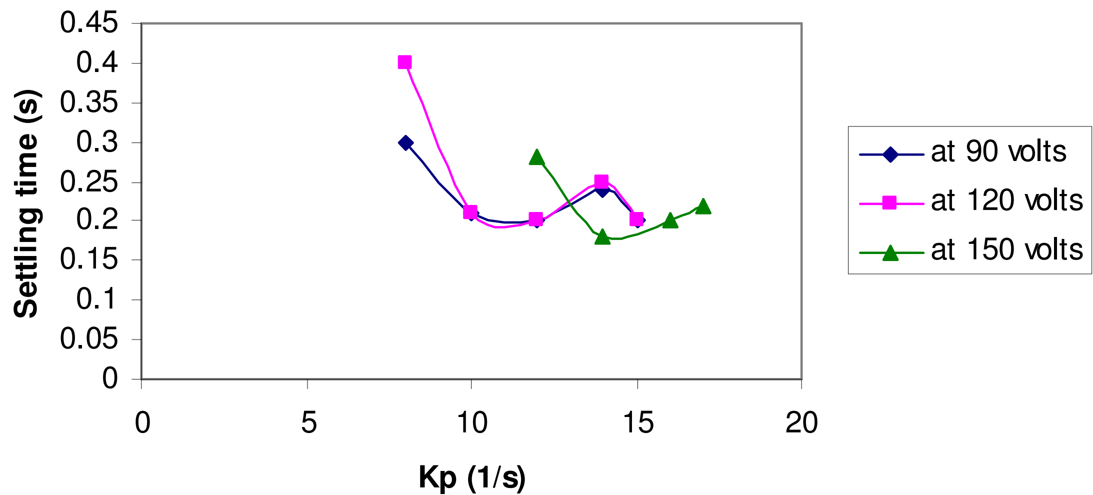

Figure 5.19: K_p versus settling time curve for 180 µm electrode design at different voltage values for 720 µm travel distance.

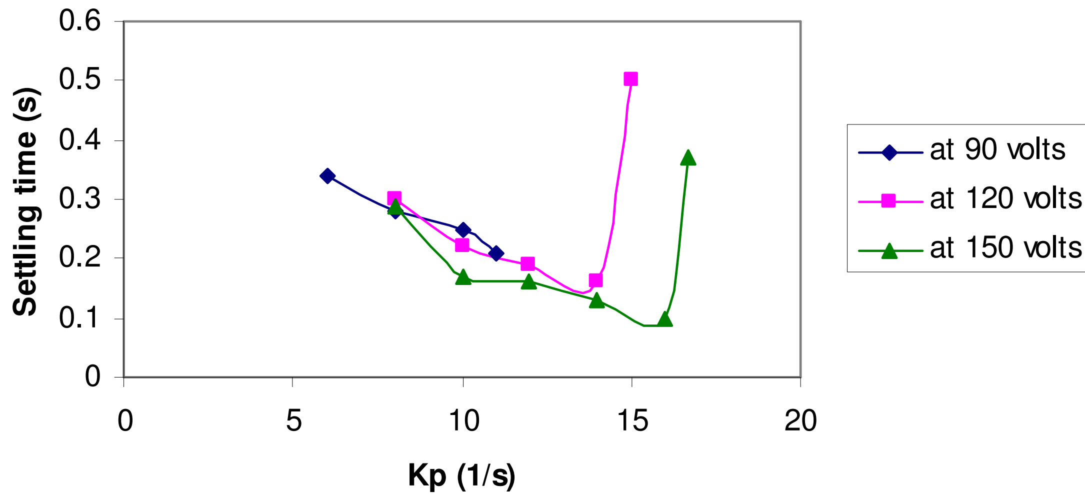

Figure 5.20: K_p versus settling time curve for 180 μm electrode design at different voltage values for 1080 μm travel distance.

The slider can not follow the signals and lose synchronization for the K_p values above what is shown in the graphs. Therefore the settling time data for higher K_p's are not presented. Since the micromotor did not operate reliably under 90 volts, lower voltage data are not included. Also, the unexpected increase in settling time on Fig. 5.18 and Fig. 5.19 is believed to be due to small step size resulting in small ball rotation and random friction. It can be observed from the graphs that as the step size increases, higher voltages favor smaller settling times through the use of high K_p values. The electrostatic springs creating oscillations and the amount of ball rotation are believed to have effect on this result. Figure 5.21 show the slider traveling 2040 μm at 150 volts for the same electrode design. The repeatability for the same distance at lower voltages could not be achieved, consequently it is not possible to compare the outcome with the previous

experiments. The initial synchronous speed was calculated to be 20.4 mm/s and the measured initial instantaneous speed was 23.84 mm/s.

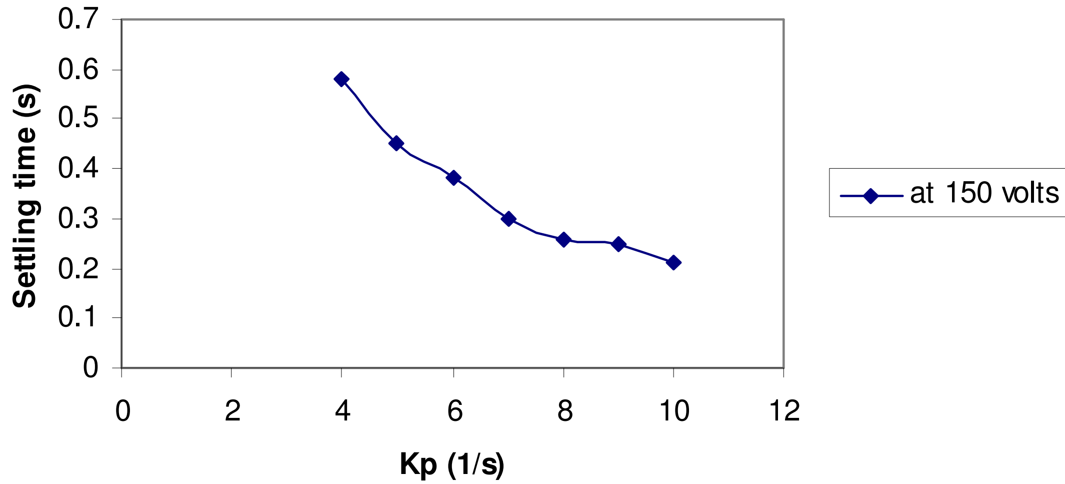

Figure 5.21: K_p versus settling time curve for 180 μm electrode design at 150 volts for 1080 μm travel distance.

Similar type of behavior is observed for the micromotor with 90 μm electrode design. However this motor did not work at 90 volts and this is directly related to the fabrication imperfections and the thickness of the air gap between the stator and slider. Figures 5.22, 5.23, and 5.24 show the results for different travel distances at 120 and 150 volts.

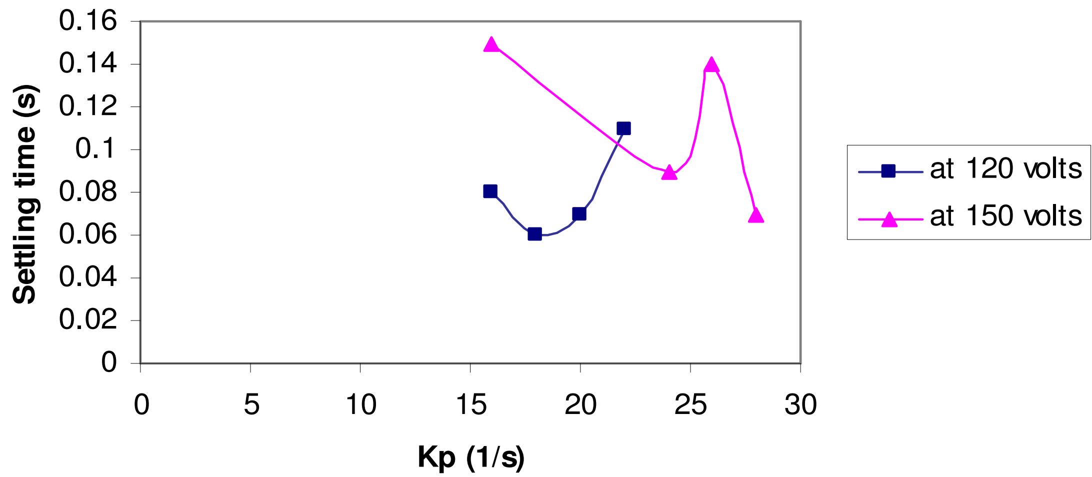

Figure 5.22: K_p versus settling time curve for 90 µm electrode design at 120 and 150 volts for 360 µm travel distance. The general trend of the line shows a decrease in settling time with increasing K_p. Unexpected increase in settling time for several K_p values are observed due to the similar reasons explained for the micromotor with 180 µm wide electrodes.

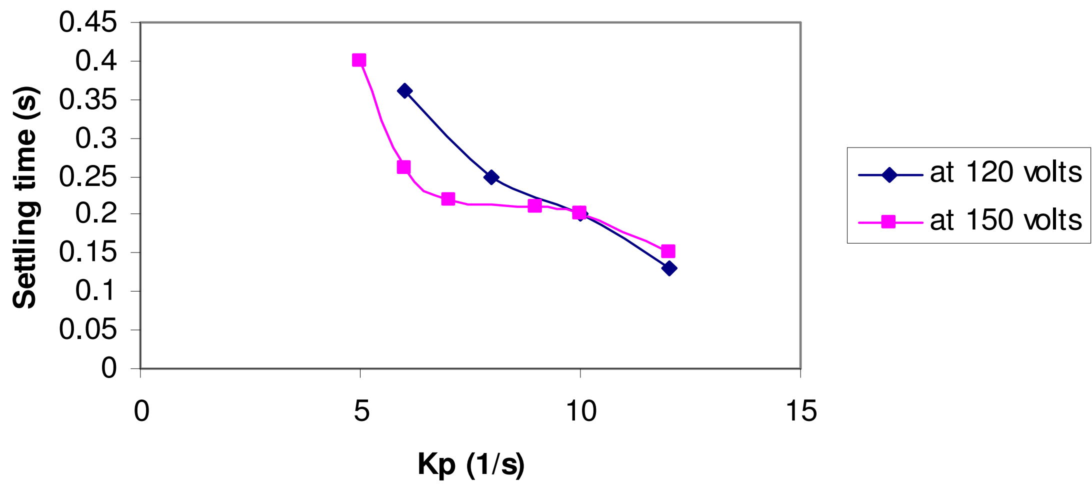

Figure 5.23: K_p versus settling time curve for 90 µm electrode design at 120 and 150 volts for 720 µm travel distance.

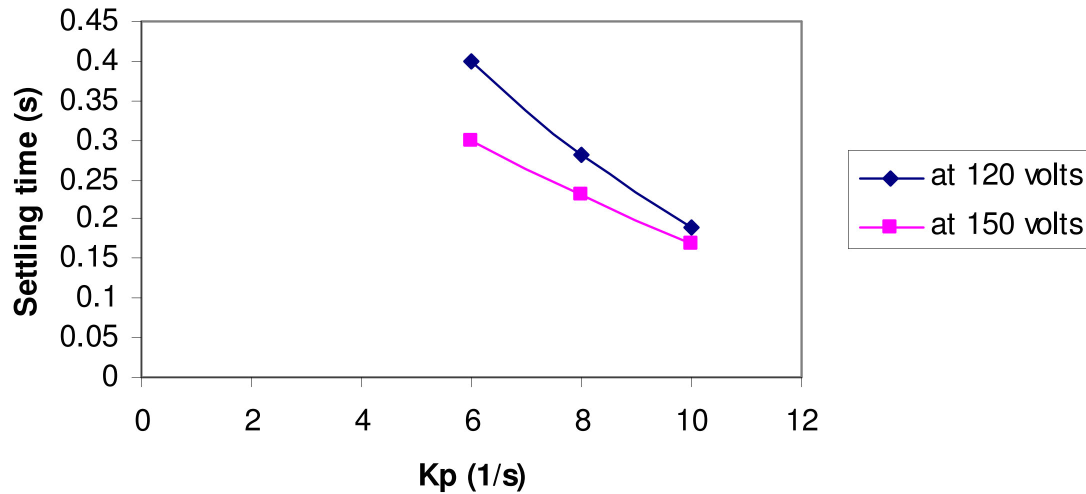

Figure 5.24: K_p versus settling time curve for 90 µm electrode design at 120 and 150 volts for 1080 µm travel distance.

The maximum synchronous speed is calculated to be 10.8 mm/s and the initial instantaneous maximum speed was measured to be 15.5 mm/s. Due to the limited output frequency capability of the microcontroller, the slider could not be moved faster as stated previously. The device is expected to move at higher speeds with a faster controller. This motor design is also tested for a traveling distance of 2040 µm, but complete set of data for different K_p could not be obtained due to the repeatability issues. Figure 5.25 shows one successful experiment with slider traveling 2040 µm for 90 µm electrode design at 150 volts with a K_p value of 5, corresponding to an initial synchronous speed of 10.2 mm/s.

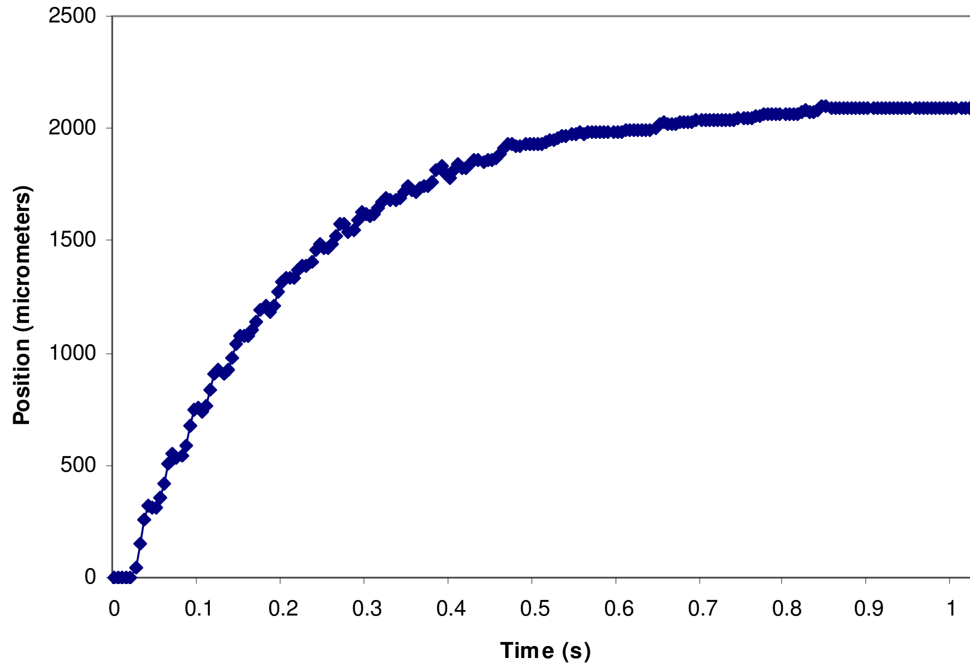

Figure 5.25: Position versus time graph for the slider traveling 2040 µm on 90 µm electrode design at 150 volts with a K_p value of 5. The initial synchronous speed is 10.2 mm/s and the initial instantaneous speed is 15.3 mm/s.

The tests described above were performed for analyzing the step response of the micromotor. Next section explains the experiments performed for evaluating the use of this micromotor as a micropositioner.

5.4 Micromotor Tests for Micropositioning Applications

In all the tests described above, the slider moved with respect to a random frame of reference, i.e. the initial position is assumed to be the reference. However, it is crucial for a micropositioner system to know the absolute position relative to a defined origin during the operation rather than moving with respect to the random initial position. Consequently, a set of coordinates can be given to the micromotor for positioning instead

of calculating and inputting the distance it is desired to travel each time. An algorithm has been developed to implement this important feature. This algorithm runs the slider to the furthest point possible in one direction at a constant speed. The system detects this point when the slider does not respond to the excitation and defines it as the origin. Next, voltages are applied to move the slider to the desired coordinate. Figure 5.26 shows the slider finding the origin and moving to the x coordinate of 1440 µm.

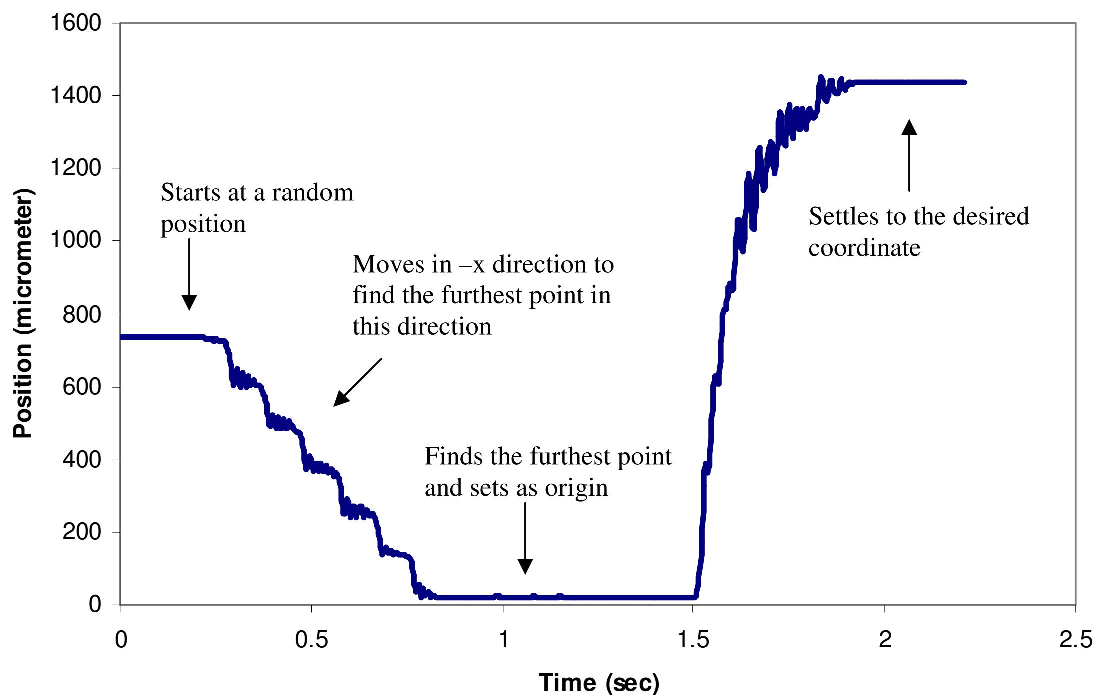

Figure 5.26: Slider setting the origin and moving to the x coordinate of 1440 µm. The test is performed on the motor with 180 µm electrodes at 150 volts with $K_p = 10$.

It is also very important for the system to respond and tolerate any outside disturbances that the device may experience. If the slider is displaced from the desired position by an outside source, the system should track the new location of the slider and return it back to the target. Figure 5.27 shows the slider reacting to such disturbances using an algorithm developed for implementing this feature.

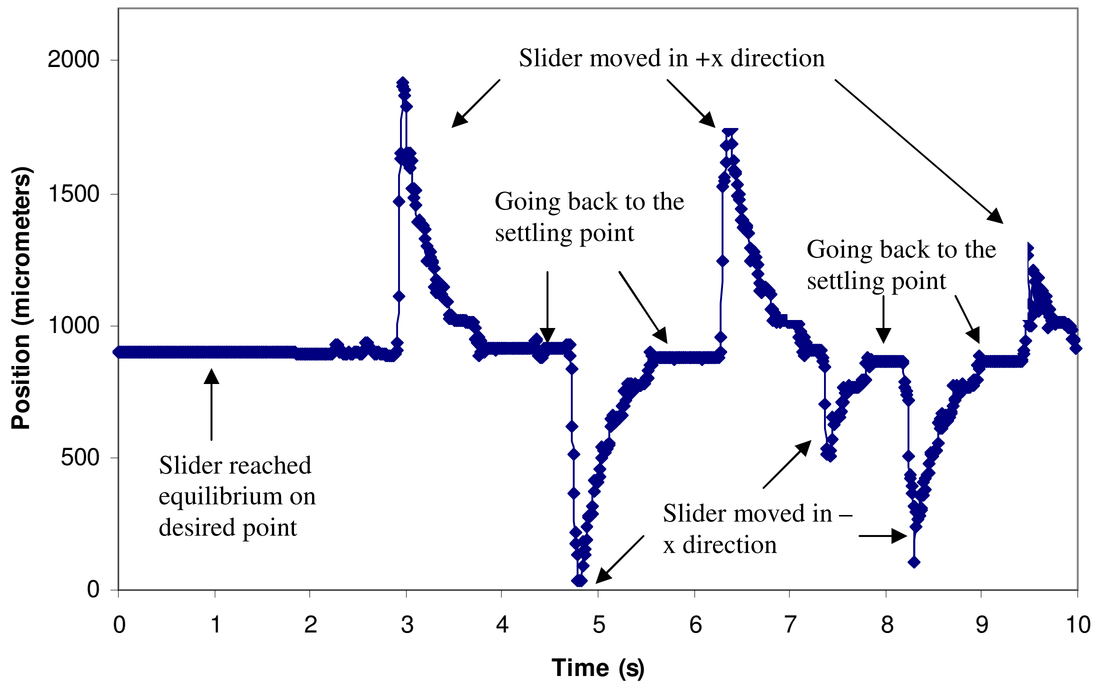

Figure 5.27: Slider response to the disturbances created by moving the slider manually with a pair of tweezers. This test has been performed on 180 μm design at 150 volts for $K_p = 3.3$.

The figure above shows the slider going back to the original settling coordinate after displaced by a pair of tweezers. This autonomous response is independent of the direction and amplitude of the disturbance. As a result, the reliability of the system is improved and the system keeps its functionality in the presence of outside effects resulting in undesired displacements. This is a big advantage of closed-loop position control system and could not be achieved using open-loop excitation. The system can reliably respond as long as the displacement does not happen faster than 50-100 mm/s, above which the microcontroller will be slow to read photodiode signals.

Finally, the device is run continuously between the same two points with and without the closed-loop system to evaluate the reliability in continuous micromotor

operation and compare with open-loop excitation. The resulting slider motion with open-loop and closed-loop systems are shown in Fig. 5.28 and Fig. 29 respectively.

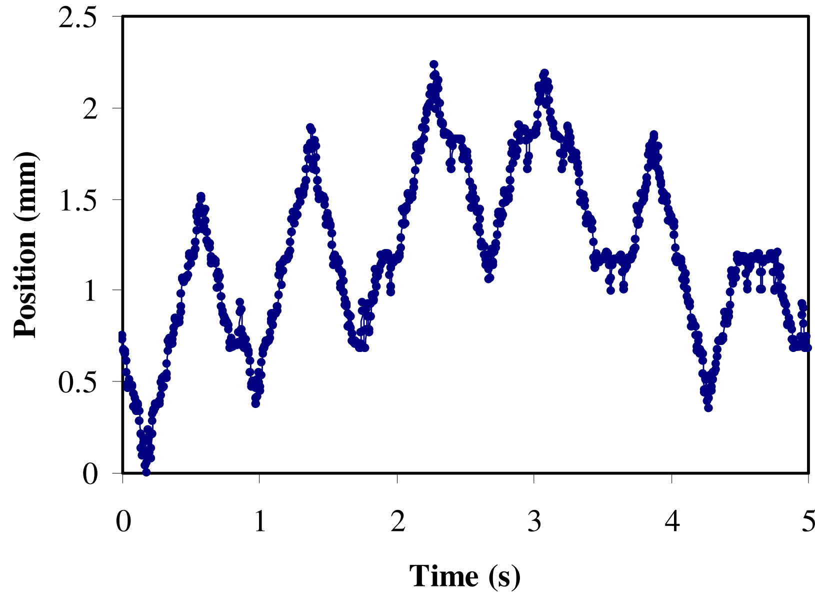

Figure 5.28: The slider toggling between two points continuously using open-loop system with sinusoidal voltages. The test is performed on the motor with 180 μm electrode design at 150 volts.

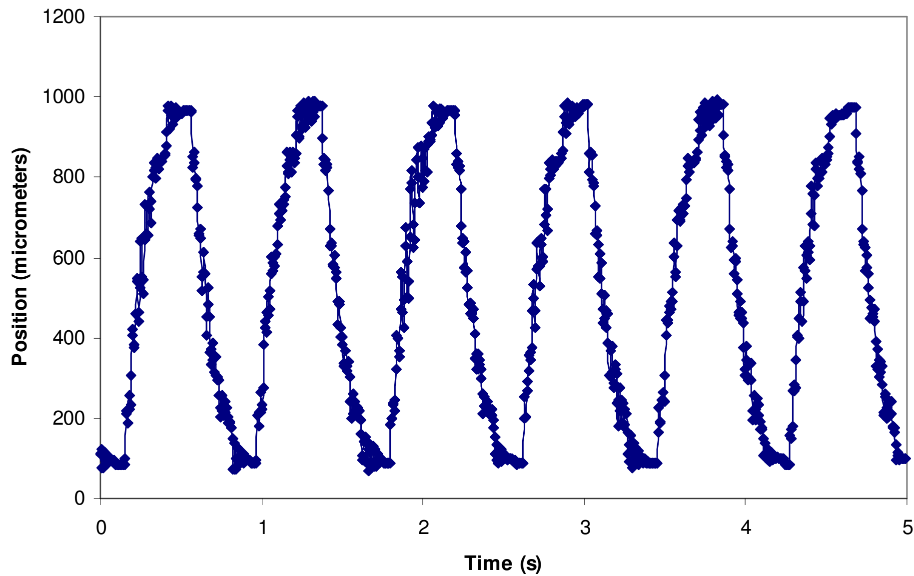

Figure 5.29: The slider toggling between two points continuously using closed-loop system. The test is performed on the motor with 180 μm electrode design at 150 volts with $K_p = 6.7$.

As it can be seen from Fig. 5.29, continuous operation does not have any effect on the system performance and positioning accuracy. This is a big improvement over open-loop excitation demonstrated in figures 2.7, 2.8, and 5.28.

5.5 Summary

This chapter explains the results of the closed-loop excitation of the micromotors with 90 µm and 180 µm wide electrodes. The feedback configuration and the algorithms developed for the microcontroller are described in detail. Successful operation using the feedback signals has been demonstrated. Detection of the oscillations at each slider step is achieved and used for maintaining a stable motion. Friction barriers were detected by using the photodiode signals and were overcome through the modification of the signal sequence.

Closed-loop position control system using the proportional control law is implemented in the device. This system changes the applied voltage frequency, that determines the speed, depending on the position of the slider. Device step response is studied and characterized for different step heights at different voltages. Highest synchronous speeds of 20.4 mm/s and 10.8 mm/s are achieved for the motors with 180 µm and 90 µm electrodes respectively. The device is also tested for micropositioner applications. Coordinate-based positioning in reference to an origin and autonomous response to outside disturbances have been demonstrated. Finally, the device is shown to operate continuously without any degradation in the positioning performance. Next chapter summarizes the content of the thesis and underlines the key accomplishments.

6. Conclusion

6.1 Summary

A closed-loop position control system based on optical position sensing has been designed and implemented into a linear variable capacitance micromotor for long-range micropositioning applications. Metal-semiconductor-metal photodiodes are incorporated into the micromotor for electrode-pole alignment detection. Electrical circuits together with a microcontroller have been designed to process photodiode signals and apply actuation voltages. This system allows for the micromotor to keep the synchronization between the motion and electrical excitation, improving accuracy, stability, and reliability.

Metal-semiconductor-metal photodiodes made of aluminum and silicon have been selected due to simpler fabrication and integration into the stator. An interdigitated structure has been designed to maximize the photoactive area. Test results showed that the increase in the output current was easily detectable in the presence of light. Based on the initial test results, the critical photodiode parameters such as finger width and finger spacing were determined. The photodiodes are located in the available peripheral area on the stator to avoid the redesign of all the masks, reducing the design cost. The width of the photodiodes and corresponding holes are selected to match that of electrodes and poles to relate the electrode-pole alignment onto the photodiode output current.

The fabrication sequence of the micromotor was modified to incorporate photodiodes on the stator and through holes in the slider. First, the photodiode layer was formed to have a good quality Schottky contact between the silicon substrate and

aluminum. This layer was covered with a photoresist mask during process steps for protection against chromium and gold etchants. Although this method has been shown to be functional, aluminum was observed to be etched locally under the photoresist. This is believed to be caused by the photoresist developer and metal etchants going through the pin holes in the sputtered chromium/gold layer. A total of eleven optical masks and thirteen lithography steps were used in the fabrication process.

A test setup has been used to investigate the micromotor performance with the control system. Electronic circuits consisting of amplifiers have been designed and implemented as an interface between the photodiode signals and microcontroller input stage. The control algorithms are developed in C++ computer language. Test results showed the successful excitation of the micromotor with photodiode signals used as feedback.

A closed-loop position control system has been implemented based on the error between the desired and current slider locations. Proportional control law was used and the effect of the proportionality constant has been investigated for various stepping distances and actuation voltages. A minimum settling time of 0.1s was achieved for a 1mm step at 150V. Closed-loop excitation has enabled sustained synchronous motion and a maximum speed of 20.4mm/s, representing a threefold increase as compared to open-loop operation. Implementing this control system, the device was shown to establish a necessary frame of reference for accurate positioning and respond autonomously to external disturbances. These are direct results of the use of feedback sensors and could not otherwise be achieved.

The integration of photodiode sensors and feedback loop enabled this device to be reliably used in long-range positioning applications. The closed-loop position control system presented in this work demonstrates the feasibility and functionality of smart microsystems using integrated feedback sensors.

6.2 Future Work

Future work will focus on the improvement of the overall system and the control architecture. The photodiode electrodes excluding the fingers will be fabricated on an insulating layer such as SiO_2 to further reduce the dark current. This will reduce the sensor noise and increase the position sensing resolution. Consequently, a more accurate and clearer signal will be fed into the microcontroller, allowing for a more precise position sensing.

The control algorithms will be improved to change the slider speed continuously rather than at full phase alignment states. This will result in a more gradual decrease in the slider speed and a smoother motion. Therefore high speeds and low device settling times can be achieved. Moreover, proportional-integral-derivative (PID) control law will be used to enhance the dynamic performance. Finally, the implementation of this control system in other micromachines will be investigated.

Appendix A: Process Recipes

Photolithography

	AZ5214E	**AZ9245**	**AZ9245**
Thickness	1.6 µm	5 µm	9 µm
Spin	3000 rpm, 30 sec	1750 rpm – 5 sec, 3600 rpm – 40 sec	300 rpm – 5 sec, 1000 rpm – 40 sec
Soft bake	Hot plate 100 °C, 60 sec	Hot plate 110 °C, 90 sec	Hot plate 110 °C, 120 sec
Exposure	40 mJ/cm^2 at 405 nm	300 mJ/cm^2 at 405 nm	720 mJ/cm^2 at 405 nm
Post exposure bake	Hot plate, 125 °C, 45 sec	No	No
Flood exposure	1200 mJ/cm^2 at 405 nm	No	No
Develop	AZ400K 1:6, 120 sec	AZ400K 1:3, 180 sec	AZ400K 1:3, 180 sec
Hard bake	No	No	No
Strip	Aleg 310	Acetone/Methanol/IPA	Acetone/Methanol/IPA

BCB 4024-40 Lithography

Thickness	~ 3 µm
Adhesion promoter	AP 3000, spinned at 3000 rpm for 30 sec
Spin	500 rpm – 8 sec, 5000 rpm – 30 sec
Soft bake	Hot plate 65 °C, 90 sec
Exposure	150 mJ/cm^2 at 365 nm
Pre develop bake	Hot plate 55 °C, 30 sec
Development	Puddle development, DS 2100 spinned at 100 rpm – 8 sec, dried at 3000 rpm – 30 sec
Post develop bake	Hot plate 65 °C, 60 sec
Soft cure / Hard cure	220 °C 50 min / 260 °C 60 min, in furnace with N_2 flow at 5ml/min
Descum	RIE chamber, O_2/ CF_4 : 90sccm/10sccm, 30 sec

DC Sputtering

	Al	Cr	Au
Thickness	0.3 µm	0.05 µm	0.2 µm
Target Conditioning	5 mtorr, 200 W, 10 min	5 mtorr, 200 W, 10 min	5 mtorr, 200 W, 10 min

Ar Pressure	5 mtorr	5 mtorr	5 mtorr
Power	200 W	200 W	200 W
Temperature	Room temperature	Room temperature	Room temperature
Time	40 min	8 min	20 min

Wet Etching

	Al	Cr	Au
Etchant	Al etchant type D, at 50 °C	Cr etchant TFD, at 50 °C	Au etchant TFA, room temp

RIE

	Si
Gases	SF_6/ O_2 : 40sccm/20sccm
Pressure	200 mtorr
Power	100 W
Time	7 min
Etch Depth	5-6 µm

DRIE of Silicon

	Pass Cycle	Etch Cycle
Coil RF	600 W	600 W
Plate RF	0 W	10W
C_4F_8	100 sccm	0 sccm
SF_6	0 sccm	130 sccm
Cycle time	3 sec	10 sec

Lift off

- 5 minute degas process
- 60 minutes ultrasonic vibrations in water. The wafers were placed in a wafer boat filled with acetone.

Appendix B: Microcontroller Programs

Open Loop Drive

```
#include  <msp430x16x.h>

//DAC1 = PHASE A,  DAC0 = PHASE B, DIGITAL OUT = PHASE C

void main(void)
{

  WDTCTL = WDTPW + WDTHOLD;                 // Stop watchdog timer

  //DAC12_0DAT = 0x0666;                    // 1V

  P4DIR |= 0x01;
  P3DIR |= 0xFF;

 ADC12CTL0 = REF2_5V + REFON;
  DAC12_1CTL = DAC12IR + DAC12AMP_6;   // Internal ref gain 1
  DAC12_0CTL = DAC12IR + DAC12AMP_6;   // Internal ref gain 1

  for (;;)
  {
    volatile unsigned int i,k;

    for (k=1;k<3;k++) {
    i = 12000;
    do {
      i=i-1;
      if (i<=12000 & i>8000) {

       DAC12_0DAT=0x000;
       DAC12_1DAT=0xFFF;
       P3OUT = 0x00;}
      if (i<=8000 & i>4000) {

       DAC12_0DAT=0x000;
       DAC12_1DAT=0x000;
       P3OUT = 0xFF; }
      if (i<=4000 & i>0){

       DAC12_0DAT=0xFFF;
      DAC12_1DAT=0x000;
       P3OUT = 0x00;}
```

```
    }
    while (i!=0);
    }

    for (k=1;k<3;k++) {
    i = 12000;
    do {
      i=i-1;
      if (i<=12000 & i>8000) {
       DAC12_1DAT=0xFFF;
       DAC12_0DAT=0x000;
       P3OUT = 0x00;}
      if (i<=8000 & i>4000) {
       DAC12_1DAT=0x000;
       DAC12_0DAT=0xFFF;
       P3OUT = 0x00; }
          if (i<=4000 & i>0) {
       DAC12_1DAT=0x000;
       DAC12_0DAT=0x000;
           P3OUT = 0xFF;}
  }
    while (i!=0);
    }
  }
}
```

Steping Control

```
#include  <msp430x14x.h>

    volatile unsigned int i, cycle, speedright, speedleft, startingspeed;
    volatile unsigned int moveleft, moveright,ignorerest;
    volatile char nextelectrode;

void main(void)
{
  WDTCTL = WDTPW+WDTHOLD;                   // Stop watchdog timer
  P6SEL = 0x07;                             // Enable A/D channel inputs
  P1DIR |= 0xEF;
  P5DIR |= 0xFF;

speedright=50000;                // speed is inversely proportional to this number
speedleft=20000;
cycle=0;
```

```
moveleft=3;
moveright=4;
startingspeed=500;
nextelectrode='a';
ignorerest=0;

   i = startingspeed;        //starter
   do {
     i=i-1;
          P1OUT |= 0x88;
          P1OUT &= ~0x66;
          P5OUT |= 0x88;
          P5OUT &= ~0x66;
     }
     while (i != 0);
   i = startingspeed;
   do {
     i=i-1;
          P1OUT |= 0x44;
          P1OUT &= ~0xAA;
          P5OUT |= 0x44;
         P5OUT &= ~0xAA;
   }
   while (i != 0);
   do {
     i=i-1;
          P1OUT |= 0x22;
          P1OUT &= ~0xCC;
          P5OUT |= 0x22;
         P5OUT &= ~0xCC;
   }
     while (i != 0);


  ADC12CTL0 = ADC12ON+MSC+SHT0_1;          // Turn on ADC12, extend sampling
time
                                          // to avoid overflow of results
  ADC12CTL1 = SHP + CONSEQ_3;              // Use sampling timer, repeated sequence
  ADC12MCTL0 = INCH_0;                     // ref+=AVcc, channel = A0
  ADC12MCTL1 = INCH_1;                     // ref+=AVcc, channel = A1
  ADC12MCTL2 = INCH_2 + EOS;               // ref+=AVcc, channel = A2
  ADC12IE = 0x04;                          // Enable ADC12IFG.2
  ADC12CTL0 |= ENC;                        // Enable conversions
  ADC12CTL0 |= ADC12SC;                    // Start conversion
  _BIS_SR(LPM0_bits + GIE);                // Enter LPM0, Enable interrupts
```

```
}

#pragma vector=ADC_VECTOR
__interrupt void ADC12ISR (void)
{

  if (cycle < moveright) {              //  moves moveright/2 electrodes right
     //P5OUT |= 0x01;

       if (nextelectrode=='a'){
       if (ADC12MEM2 > 0x400){
       P1OUT |= 0x22;
       P1OUT &= ~0xCC;
       P5OUT |= 0x22;
       P5OUT &= ~0xCC;
       P5OUT ^= 0x01;
       nextelectrode='c';
       cycle=cycle+1;
       ignorerest=1;
       i = speedright;
       do (i--);
       while (i != 0);
      }
    }
    if (ignorerest==0){
       if (nextelectrode=='c'){
       if (ADC12MEM0 > 0x400){
       P1OUT |= 0x44;
       P1OUT &= ~0xAA;
       P5OUT |= 0x44;
       P5OUT &= ~0xAA;
       P5OUT ^= 0x01;
       nextelectrode='b';
       cycle=cycle+1;
       ignorerest=1;
       i = speedright;
       do (i--);
       while (i != 0);
       }
    }
    }

    if (ignorerest==0){
    if (nextelectrode=='b'){
       if (ADC12MEM1 > 0x400 ){
       P1OUT |= 0x88;
```

```
        P1OUT &= ~0x66;
        P5OUT |= 0x88;
        P5OUT &= ~0x66;
        P5OUT ^= 0x01;
        nextelectrode='a';
        cycle=cycle+1;
        i = speedright;
        do (i--);
        while (i != 0);
        }
    }
    }

}
  if (cycle > moveright){                    //moves moveleft/2 electrode left
     //P5OUT &= ~0x01;

    if (nextelectrode=='a'){
        if (ADC12MEM2 > 0x400){
        P1OUT |= 0x44;
        P1OUT &= ~0xAA;
        P5OUT |= 0x44;
        P5OUT &= ~0xAA;
        P5OUT ^= 0x01;
        nextelectrode='b';
        cycle=cycle+1;
        ignorerest=1;
        i = speedleft;
        do (i--);
        while (i != 0);
        }
    }

    if (ignorerest==0){
    if (nextelectrode=='b'){
        if (ADC12MEM1 > 0x400){
        P1OUT |= 0x22;
        P1OUT &= ~0xCC;
        P5OUT |= 0x22;
        P5OUT &= ~0xCC;
        P5OUT ^= 0x01;
        nextelectrode='c';
        cycle=cycle+1;
        ignorerest=1;
        i = speedleft;
        do (i--);
```

```
        while (i != 0);
        }
    }
    }

    if (ignorerest==0){
    if (nextelectrode=='c'){
        if (ADC12MEM0 > 0x400){
        P1OUT |= 0x88;
        P1OUT &= ~0x66;
        P5OUT |= 0x88;
        P5OUT &= ~0x66;
        P5OUT ^= 0x01;
        nextelectrode='a';
        cycle=cycle+1;
        i = speedleft;
        do (i--);
        while (i != 0);
        }
    }
    }
}

  if (cycle==moveright){
    i = speedright;
        do (i--);
        while (i != 0);
        i = speedright;
        do (i--);
        while (i != 0);
    cycle=cycle+1;
    }

  if (cycle>=moveleft+moveright+1){
    cycle=0;}
    ignorerest=0;
}
```

Critical Speed Detection

```
#include  <msp430x14x.h>

    volatile unsigned int i, j, cycle, speed, startingspeed, accelerate;
    volatile unsigned int moveleft, moveright,ignorerest, check, treshold;
    volatile char nextelectrode, currentpd, lastpd;
```

```
void main(void)
{
  WDTCTL = WDTPW+WDTHOLD;                  // Stop watchdog timer
  P6SEL = 0x07;                            // Enable A/D channel inputs
  P1DIR |= 0xEF;
  P5DIR |= 0xFF;

speed=30000;              // speed is inversely proportional to this number
cycle=0;
moveleft=0;
moveright=20;
startingspeed=500;
nextelectrode='b';
ignorerest=0;
i=0;
accelerate=4000;
check=1;
treshold=0.9*speed;

  ADC12CTL0 = ADC12ON+MSC+SHT0_1;          // Turn on ADC12, extend sampling
time
                                           // to avoid overflow of results
  ADC12CTL1 = SHP + CONSEQ_3;              // Use sampling timer, repeated sequence
  ADC12MCTL0 = INCH_0;                     // ref+=AVcc, channel = A0
  ADC12MCTL1 = INCH_1;                     // ref+=AVcc, channel = A1
  ADC12MCTL2 = INCH_2 + EOS;               // ref+=AVcc, channel = A2
  ADC12IE = 0x04;                          // Enable ADC12IFG.2
  ADC12CTL0 |= ENC;                        // Enable conversions
  ADC12CTL0 |= ADC12SC;                    // Start conversion
  _BIS_SR(LPM0_bits + GIE);                // Enter LPM0, Enable interrupts

}

#pragma vector=ADC_VECTOR
__interrupt void ADC12ISR (void)
{

  if (i==0){
  if (cycle < moveright) {            //  moves moveright/2 electrodes right
     //P5OUT |= 0x01;

       if (nextelectrode=='a'){
       if (ADC12MEM2 > 0x400){
       P1OUT |= 0x22;
       P1OUT &= ~0xCC;
```

```
        P5OUT |= 0x22;
        P5OUT &= ~0xCC;
        nextelectrode='c';
        cycle=cycle+1;
        ignorerest=1;
      }
    }
    if (ignorerest==0){
        if (nextelectrode=='c'){
        if (ADC12MEM0 > 0x400){
        P1OUT |= 0x44;
        P1OUT &= ~0xAA;
        P5OUT |= 0x44;
        P5OUT &= ~0xAA;
        //P5OUT ^= 0x01;
        nextelectrode='b';
        cycle=cycle+1;
        ignorerest=1;
        }
    }
    }

    if (ignorerest==0){
    if (nextelectrode=='b'){
        if (ADC12MEM1 > 0x400 ){
        P1OUT |= 0x88;
        P1OUT &= ~0x66;
        P5OUT |= 0x88;
        P5OUT &= ~0x66;
        //P5OUT ^= 0x01;
        nextelectrode='a';
        cycle=cycle+1;
        ignorerest=1;
        }
    }
    }

}


  if (cycle > moveright){                    //moves moveleft/2 electrode left
      //P5OUT &= ~0x01;

    if (nextelectrode=='a'){
        if (ADC12MEM2 > 0x400){
        P1OUT |= 0x44;
```

```
        P1OUT &= ~0xAA;
        P5OUT |= 0x44;
        P5OUT &= ~0xAA;
        //P5OUT ^= 0x01;
        nextelectrode='b';
        cycle=cycle+1;
        ignorerest=1;
        }
    }

    if (ignorerest==0){
    if (nextelectrode=='b'){
        if (ADC12MEM1 > 0x400){
        P1OUT |= 0x22;
        P1OUT &= ~0xCC;
        P5OUT |= 0x22;
        P5OUT &= ~0xCC;
        //P5OUT ^= 0x01;
        nextelectrode='c';
        cycle=cycle+1;
        ignorerest=1;
        }
    }
    }

    if (ignorerest==0){
    if (nextelectrode=='c'){
        if (ADC12MEM0 > 0x400){
        P1OUT |= 0x88;
        P1OUT &= ~0x66;
        P5OUT |= 0x88;
        P5OUT &= ~0x66;
        //P5OUT ^= 0x01;
        nextelectrode='a';
        cycle=cycle+1;
        ignorerest=1;
        }
    }
    }
}

  if (cycle==moveright){

    cycle=cycle+1;}

  if (cycle>=moveleft+moveright+1){
```

```
    cycle=0;}

  if (ignorerest==1){
    i=1;}
    ignorerest=0;

 }
if (i>0){
  //P5OUT ^= 0x01;
  i=i+1;
  if (check==1){
  if (i>=treshold){
    //P5OUT ^= 0x01;
    if (nextelectrode=='a'){
      if (ADC12MEM2 > 0x400){
        check=1;}
      if(ADC12MEM0 > 0x400 || ADC12MEM1 > 0x400){
        check=0;}
    }
    if (nextelectrode=='b'){
      if (ADC12MEM1 > 0x400){
        check=1;}
      if(ADC12MEM0 > 0x400 || ADC12MEM2 > 0x400){
        check=0;}
    }
  if (nextelectrode=='c'){
      if (ADC12MEM0 > 0x400){
        check=1;}
      if(ADC12MEM2 > 0x400 || ADC12MEM1 > 0x400){
        check=0;}
    }
   }
   }
  if (i==speed){
    if (check==1){
      speed=speed-accelerate;
      P5OUT ^= 0x01;
    treshold=0.9*speed;}
    i=0;}

 }

 }
```

Overcoming Friction Barriers

```
#include  <msp430x14x.h>

    volatile unsigned int i, cycle, speed, startingspeed, inbetween;
    volatile unsigned int moveleft, moveright,ignorerest;
    volatile char nextelectrode;

void main(void)
{
  WDTCTL = WDTPW+WDTHOLD;                  // Stop watchdog timer
  P6SEL = 0x07;                            // Enable A/D channel inputs
  P1DIR |= 0xEF;
  P5DIR |= 0xFF;

speed=40000;               // speed is inversely proportional to this number
cycle=0;
moveleft=100;
moveright=0;
startingspeed=500;
nextelectrode='a';
ignorerest=0;
inbetween=0;

    i = startingspeed;         //starter
    do {
      i=i-1;
          P1OUT |= 0x88;
          P1OUT &= ~0x66;
          P5OUT |= 0x88;
          P5OUT &= ~0x66;
      }
      while (i != 0);
    i = startingspeed;
    do {
      i=i-1;
          P1OUT |= 0x44;
          P1OUT &= ~0xAA;
          P5OUT |= 0x44;
         P5OUT &= ~0xAA;
    }
    while (i != 0);
    do {
      i=i-1;
          P1OUT |= 0x22;
          P1OUT &= ~0xCC;
```

```
         P5OUT |= 0x22;
        P5OUT &= ~0xCC;
   }
    while (i != 0);


  ADC12CTL0 = ADC12ON+MSC+SHT0_1;           // Turn on ADC12, extend sampling
time
                                    // to avoid overflow of results
  ADC12CTL1 = SHP + CONSEQ_3;              // Use sampling timer, repeated sequence
  ADC12MCTL0 = INCH_0;                    // ref+=AVcc, channel = A0
  ADC12MCTL1 = INCH_1;                    // ref+=AVcc, channel = A1
  ADC12MCTL2 = INCH_2 + EOS;              // ref+=AVcc, channel = A2
  ADC12IE = 0x04;                         // Enable ADC12IFG.2
  ADC12CTL0 |= ENC;                       // Enable conversions
  ADC12CTL0 |= ADC12SC;                   // Start conversion
  _BIS_SR(LPM0_bits + GIE);               // Enter LPM0, Enable interrupts

}

#pragma vector=ADC_VECTOR
__interrupt void ADC12ISR (void)
{

  if (cycle < moveright) {             //  moves moveright/2 electrodes right
     //P5OUT |= 0x01;

       if (nextelectrode=='a'){
       if (ADC12MEM2 > 0x400 || ADC12MEM1 > 0x400 && ADC12MEM0 < 0x400){
       P1OUT |= 0x22;
       P1OUT &= ~0xCC;
       P5OUT |= 0x22;
       P5OUT &= ~0xCC;
       P5OUT ^= 0x01;
       nextelectrode='c';
       if (ADC12MEM2 > 0x400){
         cycle=cycle+1;
       }
       if (ADC12MEM1 > 0x400){
       cycle=cycle-2;}
       ignorerest=1;
       inbetween=0;
     }
       if (ADC12MEM0 > 0x400) {
       P1OUT |= 0x44;
       P1OUT &= ~0xAA;
```

```
    P5OUT |= 0x44;
    P5OUT &= ~0xAA;
    P5OUT ^= 0x01;
    nextelectrode='b';
    cycle=cycle+2;
    ignorerest=1;
    inbetween=0;
    }
    i = speed;
    do (i--);
    while (i != 0);
  }
  if (ignorerest==0){
    if (nextelectrode=='c'){
    if (ADC12MEM0 > 0x400 || ADC12MEM2 > 0x400 && ADC12MEM1 < 0x400){
    P1OUT |= 0x44;
    P1OUT &= ~0xAA;
    P5OUT |= 0x44;
    P5OUT &= ~0xAA;
    P5OUT ^= 0x01;
    nextelectrode='b';
    if (ADC12MEM0 > 0x400){
      cycle=cycle+1;
    }
    if (ADC12MEM2 > 0x400){
    cycle=cycle-2;}
    ignorerest=1;
    inbetween=0;
    }
    if (ADC12MEM1 > 0x400) {
    P1OUT |= 0x88;
    P1OUT &= ~0x66;
    P5OUT |= 0x88;
    P5OUT &= ~0x66;
    P5OUT ^= 0x01;
    nextelectrode='a';
    cycle=cycle+2;
    ignorerest=1;
    inbetween=0;
    }
    i = speed;
    do (i--);
    while (i != 0);
  }
  }
```

```
if (ignorerest==0){
if (nextelectrode=='b'){
   if (ADC12MEM1 > 0x400 || ADC12MEM0 > 0x400 && ADC12MEM2 < 0x400){
   P1OUT |= 0x88;
   P1OUT &= ~0x66;
   P5OUT |= 0x88;
   P5OUT &= ~0x66;
   P5OUT ^= 0x01;
   //P5OUT ^= 0x01;
   nextelectrode='a';
   if (ADC12MEM1 > 0x400){
     cycle=cycle+1;
   }
   if (ADC12MEM0 > 0x400){
   cycle=cycle-2;}
   inbetween=0;
   }
   if (ADC12MEM2 > 0x400) {
   P1OUT |= 0x22;
   P1OUT &= ~0xCC;
   P5OUT |= 0x22;
   P5OUT &= ~0xCC;
   P5OUT ^= 0x01;
   nextelectrode='c';
   cycle=cycle+2;
   inbetween=0;
   }
   i = speed;
   do (i--);
   while (i != 0);
}
}

// If the slider is stuck in between electrodes, go back to previous step

  if (ignorerest==0){
  if (ADC12MEM2 < 0x400){
       if (ADC12MEM1 < 0x400){
             if (ADC12MEM0 < 0x400){
              if (nextelectrode=='a'){
                if (inbetween==0 || inbetween==2){
                cycle=cycle-1;
                P1OUT |= 0x44;
                P1OUT &= ~0xAA;
                P5OUT |= 0x44;
                P5OUT &= ~0xAA;
```

```
  i = speed;
  do (i--);
  while (i != 0);
  nextelectrode='b';
  inbetween=1;
  ignorerest=1;
  }
  if (ignorerest==0){
  if (inbetween==3){
  cycle=cycle+1;
  P1OUT |= 0x22;
  P1OUT &= ~0xCC;
  P5OUT |= 0x22;
  P5OUT &= ~0xCC;
  i = speed;
  do (i--);
  while (i != 0);
  nextelectrode='c';
  inbetween=1;
  ignorerest=1;
  }}
 }

if (nextelectrode=='c'){
  if(inbetween==0 || inbetween==1){
    if (ignorerest==0){
    cycle=cycle-1;
    P1OUT |= 0x88;
    P1OUT &= ~0x66;
    P5OUT |= 0x88;
    P5OUT &= ~0x66;
    i = speed;
    do (i--);
    while (i != 0);
    nextelectrode='a';
    inbetween=3;
    ignorerest=1;
    }}
  if(inbetween==2){
    if (ignorerest==0){
    cycle=cycle+1;
    P1OUT |= 0x44;
    P1OUT &= ~0xAA;
    P5OUT |= 0x44;
    P5OUT &= ~0xAA;
    i = speed;
```

```
          do (i--);
          while (i != 0);
          nextelectrode='b';
          inbetween=3;
          ignorerest=1;
          }}
        }
        if (nextelectrode=='b'){
         if(inbetween==0 || inbetween==3){
          if (ignorerest==0){
          cycle=cycle-1;
          P1OUT |= 0x22;
          P1OUT &= ~0xCC;
          P5OUT |= 0x22;
          P5OUT &= ~0xCC;
          i = speed;
          do (i--);
          while (i != 0);
          nextelectrode='c';
          inbetween=2;
          ignorerest=1;
          }}
         if(inbetween==1){
          if (ignorerest==0){
          cycle=cycle+1;
          P1OUT |= 0x88;
          P1OUT &= ~0x66;
          P5OUT |= 0x88;
          P5OUT &= ~0x66;
          i = speed;
          do (i--);
          while (i != 0);
          nextelectrode='a';
          inbetween=2;
          ignorerest=1;
          }}
        }


}}}}
}
 if (cycle > moveright){                    //moves moveleft/2 electrode left
    //P5OUT &= ~0x01;

   if (nextelectrode=='a'){
     if (ADC12MEM2 > 0x400 || ADC12MEM0 > 0x400 && ADC12MEM1 < 0x400){
```

```
    P1OUT |= 0x44;
    P1OUT &= ~0xAA;
    P5OUT |= 0x44;
    P5OUT &= ~0xAA;
    P5OUT ^= 0x01;
    nextelectrode='b';
    if (ADC12MEM2 > 0x400){
      cycle=cycle+1;
    }
    if (ADC12MEM0 > 0x400){
    cycle=cycle-2;}
    ignorerest=1;
    inbetween=0;
    }
    if (ADC12MEM1 > 0x400) {
    P1OUT |= 0x22;
    P1OUT &= ~0xCC;
    P5OUT |= 0x22;
    P5OUT &= ~0xCC;
    P5OUT ^= 0x01;
    nextelectrode='c';
    cycle=cycle+2;
    inbetween=0;
    }
    i = speed;
    do (i--);
    while (i != 0);
}

if (ignorerest==0){
if (nextelectrode=='b'){
    if (ADC12MEM1 > 0x400 || ADC12MEM2 > 0x400 && ADC12MEM0 < 0x400){
    P1OUT |= 0x22;
    P1OUT &= ~0xCC;
    P5OUT |= 0x22;
    P5OUT &= ~0xCC;
    P5OUT ^= 0x01;
    nextelectrode='c';
    if (ADC12MEM1 > 0x400){
      cycle=cycle+1;
    }
    if (ADC12MEM2 > 0x400){
    cycle=cycle-2;}
    ignorerest=1;
    inbetween=0;
    }
```

```
    if (ADC12MEM0 > 0x400) {
    P1OUT |= 0x88;
    P1OUT &= ~0x66;
    P5OUT |= 0x88;
    P5OUT &= ~0x66;
    P5OUT ^= 0x01;
    nextelectrode='a';
    cycle=cycle+2;
    ignorerest=1;
    inbetween=0;
    }
    i = speed;
    do (i--);
    while (i != 0);
}
}

if (ignorerest==0){
if (nextelectrode=='c'){
    if (ADC12MEM0 > 0x400 || ADC12MEM1 > 0x400 && ADC12MEM2 < 0x400){
    P1OUT |= 0x88;
    P1OUT &= ~0x66;
    P5OUT |= 0x88;
    P5OUT &= ~0x66;
    P5OUT ^= 0x01;
    nextelectrode='a';
    if (ADC12MEM0 > 0x400){
      cycle=cycle+1;
    }
    if (ADC12MEM1 > 0x400){
    cycle=cycle-2;}
    inbetween=0;
    }
    if (ADC12MEM2 > 0x400) {
    P1OUT |= 0x44;
    P1OUT &= ~0xAA;
    P5OUT |= 0x44;
    P5OUT &= ~0xAA;
    P5OUT ^= 0x01;
    nextelectrode='b';
    cycle=cycle+2;
    inbetween=0;
    }
    i = speed;
    do (i--);
    while (i != 0);
```

```
 }
 }

 // If the slider is stuck in between electrodes, go back to previous step

if (ignorerest==0){
   if (ADC12MEM2 < 0x400){
          if (ADC12MEM1 < 0x400){
                 if (ADC12MEM0 < 0x400){
                   if (nextelectrode=='a'){
                     if (inbetween==0 || inbetween==3){
                     cycle=cycle-1;
                     P1OUT |= 0x22;
                     P1OUT &= ~0xCC;
                     P5OUT |= 0x22;
                     P5OUT &= ~0xCC;
                     i = speed;
                     do (i--);
                     while (i != 0);
                     nextelectrode='c';
                     inbetween=1;
                     ignorerest=1;
                     }
                     if (ignorerest==0){
                     if (inbetween==2){
                     cycle=cycle+1;
                     P1OUT |= 0x44;
                     P1OUT &= ~0xAA;
                     P5OUT |= 0x44;
                     P5OUT &= ~0xAA;
                     i = speed;
                     do (i--);
                     while (i != 0);
                     nextelectrode='b';
                     inbetween=1;
                     ignorerest=1;
                     }}
                    }

                   if (nextelectrode=='c'){
                     if(inbetween==0 || inbetween==2){
                       if (ignorerest==0){
                       cycle=cycle-1;
                       P1OUT |= 0x44;
                       P1OUT &= ~0xAA;
                       P5OUT |= 0x44;
```

```
    P5OUT &= ~0xAA;
    i = speed;
    do (i--);
    while (i != 0);
    nextelectrode='b';
    inbetween=3;
    ignorerest=1;
    }}
  if(inbetween==1){
    if (ignorerest==0){
    cycle=cycle+1;
    P1OUT |= 0x88;
    P1OUT &= ~0x66;
    P5OUT |= 0x88;
    P5OUT &= ~0x66;
    i = speed;
    do (i--);
    while (i != 0);
    nextelectrode='a';
    inbetween=3;
    ignorerest=1;
    }}
}
if (nextelectrode=='b'){
  if(inbetween==0 || inbetween==1){
    if (ignorerest==0){
    cycle=cycle-1;
    P1OUT |= 0x88;
    P1OUT &= ~0x66;
    P5OUT |= 0x88;
    P5OUT &= ~0x66;
    i = speed;
    do (i--);
    while (i != 0);
    nextelectrode='a';
    inbetween=2;
    ignorerest=1;
    }}
  if(inbetween==3){
    if (ignorerest==0){
    cycle=cycle+1;
    P1OUT |= 0x22;
    P1OUT &= ~0xCC;
    P5OUT |= 0x22;
    P5OUT &= ~0xCC;
    i = speed;
```

```
                do (i--);
                while (i != 0);
                nextelectrode='c';
                inbetween=2;
                ignorerest=1;
                }}
              }
}}}}
}
 if (cycle==moveright){
   cycle=cycle+1;}
 if (cycle>=moveleft+moveright+1){
   cycle=0;}
   ignorerest=0;
}
```

Closed Loop Position Control with Proportional Control Law

```
#include  <msp430x16x.h>

// DAC1 = PHASE A,  DAC0 = PHASE B, DIGITAL OUT = PHASE C
// ADC12MEM2 = PDA, ADC12MEM1 = PDB, ADC12MEM0 = PDC

// Current position in synthesizer
static unsigned dac_pos = 0;
// Number of oscillation periods
static unsigned dac_periods = 0;
// Advancement direction
static unsigned dac_dir = 0;
// Number of oscillation periods before direction reverse
static const unsigned dac_reverse_periods = 4000;
// Number of data points in synthesizer
static const unsigned dac_count = 24;
// Phase shift between synthesizer outputs
static const unsigned dac_shift = 8;
// Look-up table of synthesizer values
static const unsigned int dac_table[] = {
 128, 161, 192, 218, 239, 252, 255, 252, 239, 218, 192, 161,
 128,  95,  64,  37,  17,  4,    0,   4,  17,  37,  64,  95
};

volatile int stepcount=0, xcurrent=0, output, i, k;
volatile char lastaligned='c';
volatile int error=0, errorold=0, errorderivative=0, errorintegral=0;
```

```
// THE PARAMETERS TO BE CHANGED

static int xdesired=240; //in micrometers
volatile int amplitude=150;  // voltage amplitude
volatile double proportional=10, derivative=0, integral=0;

void main(void)
{

  WDTCTL = WDTPW + WDTHOLD;                 // Stop watchdog timer

  P6SEL |= 0x07;                            // Enable A/D channel inputs
  P4DIR |= 0x07;
  P3DIR |= 0xFF;

  amplitude=amplitude*20/3;
  proportional=proportional*3/20;
  derivative=derivative*3/20;
  integral=integral*3/20;

  // Disable XT2 and set DCO to fastest speed
  DCOCTL = DCO2|DCO1|DCO0;            // Highest Frequency; Modulator Unused
  BCSCTL1 = XT2OFF|RSEL2|RSEL1|RSEL0; // XT2 Off; Fastest Resistor
  BCSCTL2 = 0;                        // MCLK=DCO/1; SMCLK=DCO/1; Internal Resistor

  // ADC: Measure A0-A2 on Timer B1
  ADC12CTL0 = MSC|REF2_5V|REFON|SHT02;
   // Multiple Sample & Hold, 2.5V Reference, ADC12 ON
  ADC12CTL1 = SHP|SHS1|SHS0|CONSEQ0;
   // TimerB1 Timing, Sampling Timer, Repeat Sequence, Internal Timer/1
  ADC12MCTL0 = INCH_0;                  // ref+=AVcc, channel = A0
  ADC12MCTL1 = INCH_1;                  // ref+=AVcc, channel = A1
  ADC12MCTL2 = INCH_2 + EOS;            // ref+=AVcc, channel = A2
  ADC12IE = 0x04;           // Trigger when channel 7 (EOS) finished
  ADC12CTL0 |= ADC12ON;

  // DAC: Whatever Mustafa set it to
  DAC12_1CTL = DAC12IR + DAC12AMP_6;       // Internal ref gain 1
  DAC12_0CTL = DAC12IR + DAC12AMP_6;       // Internal ref gain 1

  // Timer A: Control DAC
  TACTL=TASSEL_1 | TACLR;
  TACCR0= 300000;
  TACCTL0=CCIE;

  // Timer B: Setup ADC
```

```
  TBCTL=TBSSEL_1 | TBCLR;
  TBCCTL0 = 0;                    // No modulation
  TBCCTL1 = OUTMOD1|OUTMOD0;      // Set on compare, clear on timer reset
  TBCCR0 = 20;
  TBCCR1 = TBCCR0 / 2;

  // Main Loop: Enable ADC, Timers, Interrupts
  ADC12CTL0 |= ADC12ON|ENC; // Enable ADC
  TACTL |= MC_1;
  TBCTL |= MC_1;

  P3OUT |= 0xFF;
  DAC12_0DAT=0x000;
  DAC12_1DAT=0x000;
  for (k=1;k<12;k++){
  i=50000;
  do {
    i=i-1;}
  while (i!=0);}

  _BIS_SR(LPM0_bits + GIE);                 // Enter LPM0, Enable interrupts
  for(;;);
}

#pragma vector=ADC_VECTOR
__interrupt void ADC12ISR (void)
{
  // Ready ADC for next sample
    ADC12CTL0 |= ENC;
    P4OUT ^= 0x02;

    if (ADC12MEM2 < 0x100){
      if (lastaligned=='b'){
        stepcount=stepcount+1;}
      if (lastaligned=='c'){
        stepcount=stepcount-1;}
      lastaligned='a';}

    if (ADC12MEM1 < 0x100){
      if (lastaligned=='c'){
        stepcount=stepcount+1;}
      if (lastaligned=='a'){
        stepcount=stepcount-1;}
      lastaligned='b';}

    if (ADC12MEM0 < 0x100){
```

```
      if (lastaligned=='a'){
        stepcount=stepcount+1;}
      if (lastaligned=='b'){
        stepcount=stepcount-1;}
      lastaligned='c';}

xcurrent=120*stepcount; // for the motor with 90 µm electrode design, step count should
// be multiplied with 60
// calculate error
error=xdesired-xcurrent;
errorderivative=error-errorold;
errorintegral=errorintegral+error;
errorold=error;

if (error >0){
  dac_dir = 0;}
if (error < 0){
  dac_dir = 1;
  error=-1*error;}

// MODIFY SPEED
output=proportional*error + derivative*errorderivative + integral*errorintegral;

if (output != 0){
  TACCR0= 72000/output;}
if (output == 0){
  TACCR0=32000;}
if (TACCR0 < 4){
  TACCR0=4;}
}

#pragma vector=TIMERA0_VECTOR
__interrupt void Timer_A (void) {
P4OUT ^= 0x04;
  // Advance sin synthesis
  if(dac_dir) {
    dac_pos = (dac_pos + dac_count - 1) % dac_count;
  } else {
    dac_pos = (dac_pos + 1) % dac_count;
  }
  // Check for direction reverse
  if(dac_pos == 0) {
    dac_periods++;
    if(dac_periods >= dac_reverse_periods) {
      dac_periods = 0;
      dac_dir = !dac_dir;
```

```
    }
  }
  // P3 has phase of 0 degrees
  P3OUT = amplitude * ((unsigned long)(dac_table[dac_pos])) / 1000;
  // DAC 1 has phase of 120 degrees
  DAC12_1DAT = amplitude * (((unsigned long)dac_table[(dac_pos + dac_shift) %
dac_count]) << 4) / 1000;
  // DAC 0 has phase of 240 degrees
  DAC12_0DAT = amplitude * (((unsigned long)dac_table[(dac_pos + 2*dac_shift) %
dac_count]) << 4) / 1000;
}
```

The programs written for micropositioner applications are slightly different than the above program designed for closed-loop position control. Therefore they are not included.

REFERENCES

[1] S. D. Senturia, Microsystem Design. Boston: Kluwer Academic Publishers, 2001.

[2] J. W. Judy, "Microelectromechanical systems (MEMS): fabrication, design and applications", Smart Materials and Structures, 2001, vol 10, pp. 1115-1134.

[3] R. M. White, "A sensor classification scheme", IEEE Trans. Ultrason. Ferroelectr. Freq. Control, vol. 34, pp. 124-126.

[4] G. T. Kovacs, Micromachined Transducers Sourcebook, Boston, MA: McGraw-Hill, 1998.

[5] M. Madou, Fundamentals of Microfabrication, Boca Raton, FL: Chemical Rubber Company, 1997.

[6] J. Bustillo, R. T. Howe, R. S. Muller, "Surface micromachining for microelectromechanical systems", Proceedings of IEEE, Aug 1998, vol. 86, no. 8, pp. 1552-1574.

[7] K. E. Petersen, "Silicon as a mechanical material", Proceedings of IEEE, vol 70, pp. 420-457.

[8] F. Larmer, P. Schilp, Method of anisotropically etching silicon, German patent DE4,241,045.

[9] C. Keller, M. Ferrari, "Milli-scale polysilicon structures", Solid-State Sensors and Actuators Workshop Technical Digest, Hilton Head Island, SC, 1994, pp.132-137.

[10] P. Barth, "Silicon fusion bonding for fabrication of sensors, actuators, and microstructures", Sensors Actuators A, April 1990, vol. A23, pp. 919-926.

[11] G. Wallis, D. I. Pomerantz, "Field assisted glass-metal sealing", Journal of Applied Physics, vol. 40, pp. 3946-3949.

[12] M. B. Cohn, L. Yiching, R. T. Howe, A. P. Pisano, "Wafer-to-wafer transfer of microstructures for vacuum packaging", Technical Digest Solid-State Sensors and Actuator Workshop, Hilton Head Island, SC, 1996, pp. 32-35.

[13] D. Mass, B. Bustgens, J. Fehrenberg, W. Keller, P. Ruther, W. K. Schomburg, D. Seidel, "Fabrication of microcomponents using adhesive bonding techniques", Proceedings of IEEE International Workshop on Microelectromechanical Systems, San Diego, CA, 1996, pp. 331-336.

[14] W. Ehrfeld *et al*, "Fabrication of microstructures using the LIGA process", Proceedings of IEEE Micro Robots Teleoperators Workshop, 1987, pp. 11/1-11/11.

[15] B. Borovic, A. Q. Liu, D. Popa, H. Cai, F. L. Lewis, "Open-loop versus closed-loop control of MEMS devices: choices and issues", Journal of Micromechanics and Microengineering, vol. 15, pp. 1917-1924.

[16] D. O. Popa, J. T. Wen, H. E. Stephanou, G. Skidmore, M. Ellis, "Dynamic modeling and input shaping for MEMS", Technical Proceedings of 2004 NSTI Nanotechnology Conference and Trade Show, March 7-11, 2004, Boston, vol.2, pp. 315-318.

[17] D. O. Popa, B. H. Kang, J. T. Wen, H. E. Stephanou, G. Skidmore, A. Geisberger, "Dynamic modeling and input shaping of thermal bimorph MEMS

actuators", Proceedings of 2003 IEEE International Conference on Robotics Automation, September 14-19, Taipei, vol.1, pp. 1470-1475.

[18] B. Borovic, C. Hong, X. M. Zhang, A. Q. Liu, F. L. Lewis, "Open vs. closed loop control of the MEMS electrostatic comb drive", 13th Mediterranean Conference on Control and Automation, May 27-29, 2005, Limassol, vol.2 pp.982-988.

[19] M. S-C. Lu, G. K. Fedder, "Position control of parallel-plate microactuators for probe-based data storage", Journal of Microelectromechanical systems, vol. 13, pp. 759-769.

[20] B. Borovic, C. Hong, A. Q. Liu, L. Xie, F. L. Lewis, "Control of a MEMS optical switch", International Conference on Decision and Control, December 14-17, 2004, Nassau, vol. 3, pp. 3039-3044.

[21] Y. Sun, B. J. Nelson, D. P. Potasek, E. Enikov, "A bulk microfabricated multi-axis capacitive cellular force sensor using transverse comb drives", Journal of Micromechanics and Microengineering, vol. 12, pp. 832-840.

[22] Y. Sun, D. Piyabongkarn, A. Sezen, B. J. Nelson, R. Rajamani, "A high aspect ratio two axis electrostatic microactuator with extended travel range", Sensors and Actuators A, vol. 102, pp. 49-60.

[23] J. Boland, Y. H. Chao, Y. Suzuki, Y. C. Tai, "Microelectret power generator", IEEE 16th Annual International Conference on Microelectromechanical systems, Kyoto, Japan, 2003.

[24] J. Boland, H. W. Messenger, H. W. Lo, Y. C. Tai, "Arrayed liquid rotor electret power generator systems", IEEE Microelectromechanical Systems, Miami, FL, USA, 2005.

[25] T. Sterken, P. Fiorini, K. Baert, R. Puers, G. Borghs, "An electret based electrostatic μ-generator", 12th International Conference on Transducers, Solid State Actuators and Microsystems, Boston, MA, USA, 2003.

[26] S. Tanaka, T. Genda, M. Esashi, "High power electrostatic motor and generator using electrets", 12th International Conference on Transducers, Solid State Actuators and Microsystems, Boston, MA, USA, 2003.

[27] D. P. Arnold, F. Cros, I. Zana, M. G. Allen, S. Das, J. H. Lang, "Magnetic induction machines embedded in fusion bonded silicon", Solid State Sensors, Actuators and Microsystems Workshop, Hilton Head Island, SC, USA, 2004.

[28] S. Das, D. P. Arnold, M. G. Allen, "Multi watt electric power from a fabricated permanent magnet generator", IEEE Microelectromechanical Systems, Miami, FL, USA, 2005.

[29] H. Guckel, T. R. Christenson, K. J. Skrobis, T. S. Jung, J. Klein, K. V. Hartojo, I. Widjaja, "A first functional current excited planar rotational magnetic micromotor", IEEE Microelectromechanical Systems, NY, USA, 1993.

[30] Y. B. Jeon, R. Sood, J. H. Jeong, S. G. Kim, "MEMS power generator with transverse mode thin film PZT", Sensors and Actuators, vol. 122, no. 1, pp. 16-22.

[31] R. Sood, S. G. Kim, "Piezoelectric micro power generation for energy harvesting", Solid State Sensors, Actuators and Microsystems Workshop, Hilton Head Island, SC, USA, 2004.

[32] S. Cagatay, B. Koc, P. Moses, K. Uchino, "A piezoelectric micromotor with a stator of phi=1.6mm and l=4mm using bulk PZT", Japanese Journal of Applied Physics, 2004, part 1, vol. 43, pp. 1429-1433.
[33] J. Friend, K. Nakamura, S. Ueha, "A piezoelectric micromotor using in-plane shearing of PZT elements", IEEE/ASME Transactions on Mechatronics, vol. 9, pp. 467-473.
[34] S. Dong, S. P. Lim, K. H. Lee, J. Zhang, L. C. Lim, K. Uchino, "Piezoelectric ultrasonic micromotor with 1.5 mm diameter", IEEE Transactions on Ultrasonics, Ferroelectrics and Frequency Control, vol. 50, pp. 361-367, 2003.
[35] J. T. Leinvuo, S. A. Wilson, H. J. A. Almond, R. W. Whatmore, "Experimental design and construction of a flextensional ultrasonic piezoelectric micromotor", 10th European Meeting on Ferroelectricity, Cambridge, UK, 2004.
[36] W. S. N. Trimmer, K. J. Gabriel, "Design consideration for a practical electrostatic micromotor", Sensors and Actuators, vol. 11, pp. 189-206, 1987.
[37] L. S. Fan, Y. C. Tai, R. S. Muller, "IC-processed electrostatic micromotors", Technical Digest of International Electron Devices Meeting, San Fransisco, CA, USA, 1988.
[38] Y. C. Tai, L. S. Fan, R. S. Muller, "IC processed micromotors: design, technology and testing", Proceedings of Micro Electromechanicalsystems, Salt Lake City, UT, 1989.
[39] M. Mehregany, S. F. Bart, L. S. Tavrow, J. H. Lang, S. D. Senturia, "Principles in design and microfabrication of variable capacitance side drive motors", Journal of Vacuum Science & Technology A, vol. 8, pp. 3614-3624, 1990.
[40] T. A. Lober, "A microfabricated electrostatic motor design and process", Cambridge, MA: Massachusetts Institute of Technology, 1988.
[41] L. S. Fan, Y. C. Tai, R. S. Muller, "Integrated movable micromechanical structures for sensors and actuators", IEEE Transactions on Electron Devices, vol. 35, pp. 724, 1988.
[42] M. Mehregany, K. J. Gabriel, W. S. N. Trimmer, "Integrated fabrication of polysilicon mechanisms", IEEE Transactions on Electron Devices, vol. 35, pp. 719, 1988.
[43] M. Mehregany, S. D. Senturia, J. H. Lang, "Measurement of wear in polysilicon micromotors", IEEE Transactions on Electron Devices, vol. 39, pp. 1136, 1992.
[44] M. Mehregany, S. D Senturia, J. H. Lang, "Friction and wear in microfabricated harmonic side drive motors", IEEE Solid State Sensor and Actuator Workshop Technical Digest, Hilton Head Island, SC, USA, 1990.
[45] J. U. Jeon, S. J. Woo, T. Higuchi, "Variable capacitance motors with electrostatic suspension", Sensors and Actuators A: Physical, vol. 75, pp. 289, 1999.
[46] C. Ruffert, R. Gehrking, B. Ponick, H. H. Gatzen, "Magnetic levitation assisted guide for a linear micro actuator", IEEE Transactions on Magnetics, vol. 42, pp. 3785, 2006.
[47] W. Chien-Chang, Y. Yeong-Der, L. Chien-Sheng, C. Lung-Yu, "Micromagnetic suspension motor design for miniature optical drive", Japanese Journal of Applied Physics, Part 1, vol. 45, pp. 5801.

[48] C. Livermore, A. R. Forte, T. Lyszczarz, S. D. Umans, A. A. Ayon, J. H. Lang, "A high power MEMS electric induction motor", Journal of Microelectromechanical Systems, vol. 13, pp. 465-471, 2004.

[49] N. Ghalichechian, A. Modafe, J. H. Lang, R. Ghodssi, "Dynamic characterization of a linear electrostatic micromotor supported on microball bearings", Sensors and Actuators A, 16 May 2007, vol. 136, no. 2, pp. 496-503.

[50] N. Ghalichechian, M. I. Beyaz, R. Ghodssi, "A rotary micromotor supported on microball bearings", The 14th International Conference on Solid State Sensors, Actuators and Microsystems (Transducers `07), June 10-14, 2007, pp. 1123-1126.

[51] J. Zhang, M. Schroff, "High performance micromotor control systems", 29th Annual Conference of the IEE E Industrial Electronics Society, 2003, vol. 1, pp. 347-352.

[52] P. L. Chapman, P. T. Krein, "Perspectives on micromotors and electric drives", IEEE Industrial Applications Magazine, Jan/Feb, 2003, pp. 62-67.

[53] M. Patrascu, S. Stramigioli, "Stick-slip actuation of electrostatic stepper micropositioners for data storage – the μwalker," *Proceedings of International Conference on MEMS, NANO and Smart Systems*, Los Alamitos, CA, USA, 2005, pp. 81-86.

[54] C.S.B. Lee, S. Han, N.C. MacDonald, "Single crystal silicon (scs) xy-stage fabricated by DRIE and IR alignment," *Proceedings of IEEE 13th Annual International Conference on Micro Electro Mechanical Systems*, Miyazaki, Japan, 2000, pp. 28-33.

[55] I. Shubin, P. LiKamWa, "A guided-wave optical switch controlled by a micro-electro-mechanical cantilever," *IEEE Lasers and Electro-Optics Society 2000 Annual Meeting*, Rio Grande, Puerto Rico, 2000, vol. 1, pp. 50-51.

[56] R.R.A. Syms, "Long-travel electrothermally driven reosonant cantilever microactuators," Journal *of Micromechanics and Microengineering*, vol. 12, no. 3, pp. 211-218, May 2002.

[57] H. Guckel, J. Klein, T. Christenson, K. Skrobis, M. Laudon, E.G. Lovell, "Thermo-magnetic metal flexure actuators," *IEEE Solid-State Sensor and Actuator Workshop*, Hilton Head Island, SC, 1992, pp. 73-75.

[58] S.C. Shen, C.T. Pan, H.P. Chou, "Electromagnetic optical switch for optical network communication," *Journal of Magnetism and Magnetic Materials*, vol. 239, no. 1-3, pp. 610-613, February 2002.

[59] Y. Soeno, S. Ichikawa, T. Tsuna, Y. Sato, I. Sato, "Piezoelectric piggy-back microactuator for hard disk drive," *IEEE Transactions on Magnetics*, vol. 35, no. 2, pt. 1, pp. 983-987, March 1999.

[60] P. Cusin, T. Sawai, S. Konishi, "Compact and precise positioner based on the inchworm principle," *Journal of Micromechanics and Microengineering*, vol. 10, no. 4, pp. 516-521, December 2000.

[61] L.L. Chu, Y,B, Gianchandani, "A micromachined 2D positioner with electrothermal actuation and sub-nanometer capacitive sensing," *Journal of Micromechanics and Microengineering*, vol. 13, no. 2, pp. 279-285, March 2003.

[62] D.A. Horsley, N. Wongkomet, R. Horowitz, A.P. Pisano, "Precision positioning using a microfabricated electrostatic actuator," *IEEE Transactions on Magnetics*, vol. 35, no. 2, pt. 1, pp. 993-999, March 1999.

[63] N. Ghalichechian, A. Modafe, R. Ghodssi, P. Lazzeri, R. Micheli, M. Anderle, "Integration of Benzocyclobutene Polymers and Silicon Micromachined Structures Using Anisotropic Wet Etching," *Journal of Vacuum Science and Technology B,* vol. 22, no. 5, pp. 2439-2447, 2004.

[64] A. Modafe, N. Ghalichechian, B. Kleber and R. Ghodssi, "Electrical Characterization of Benzocyclobutene Polymers for Electric Micromachines," *IEEE Transactions on Device and Materials Reliability*, vol. 4, no. 3, pp. 495-508, September 2004.

[65] A. Modafe, N. Ghalichechian, M. Powers, M. Khbeis, and R. Ghodssi, " Embedded Benzocyclobutene in Silicon (EBiS): An Integrated Fabrication Process for Electrical and Thermal Isolation in MEMS," *Microelectronic Engineering*, vol. 82, no. 2, pp. 154, 2005.

[66] T-W. Lin, A. Modafe, B. Shapiro and R. Ghodssi, "Characterization of Dynamic Friction in MEMS-Based Micro-Ball Bearings," *IEEE Transactions on Instrumentation and Measurement*, vol. 53, no. 3, pp. 839-846, 2004.

[67] X. Tan, A. Modafe, and R. Ghodssi, "Measurement and Modeling of Dynamic Rolling Friction in Linear Microball Bearings," *Journal of Dynamic Systems, Measurement, and Control*, vol. 128, no. 4, pp. 891-898, December 2006.

[68] M. McCarthy, B. Hanrahan, C. Zorman, and R. Ghodssi, "Rolling Friction in MEMS Ball Bearings: The Effects of Loading and Solid Film Lubrication," *STLE/ASME International Joint Tribology Conference*, San Diego, CA, October 22 - 24, 2007.

[69] N. Ghalichechian, M.McCarthy, M. I. Beyaz, R. Ghodssi, "Measurement and Modeling of Friction in Linear and Rotary Micromotors Supported on Microball Bearings," *Proceedings of the 21st IEEE International Conference on Micro Electro Mechanical Systems*, Tucson, AZ, USA, January 13-17, 2008, pp. 507-510.

[70] D. J. Alladi, M. L. Nagy, S. L. Garverick, "An IC for closed loop control of a micromotor with an electrostatically levitated rotor", IEEE International Symposium on Circuits and Systems, 1999, vol. 6, pp. 489-492.

[71] S. L. Garverick, M. L. Nagy, N. K. Rao, D. K. Hartsfield, A. Purushotham, " A capacitive sensing integrated circuit for detection of micromotor critical angles", Journal of Solid State Circuits, Jan 1997, vol. 32, no. 1, pp. 23-30.

[72] A. Purushotham, S. L. Garverick, C. Edwards, M. L. Nagy, "A closed loop micromotor control system", IEEE International Symposium on Circuits and Systems, 1996, vol. 4, pp. 209-212.

[73] N. K. Rao D. K. Hartsfield, A. Purushotham, S. L. Garverick, "An IC for closed loop micromotor control", 1995 URSI International Symposium on Signals, Systems and Electronics, 1995, pp. 563-566.

[74] H. Guckel, T. R. Christenson, K. J. Skrobis, T. S. Jung, J. Klein, K. V. Hartojo, I. Widjaja, "A first functional current excited planar rotational magnetic micromotor", IEEE Micro electromechanical systems, 1993, pp. 7-11.

[75] Z. Li, J. Chen, X. Ge, C. Zhang, "Novel microstepping control methods for electromagnetic micromotors with star connected windings", Sensors and Actuators A, March 2007, vol. 134, no. 2, pp. 513-518.
[76] S. E. Lyshevski, "Modeling and control of MEMS with high speed synchronous micromotors and controllers/drivers-on-VLSI-chip ICs", Energy Conversion and Management, March 2003, vol. 44, no. 5, pp. 667-679.
[77] A. Modafe, "Benzocyclobutene-Based Electric Micromachines Supported on Microball Bearings: Design, Fabrication, and Characterization", in Dept. of Elecrical and Computer Eng., University of Maryland, College Park, 2007.
[78] N. Ghalichechian, "Integration of Benzocyclobutene Polymers and Silicon Micromachined Structures Fabricated with Anisotropic Wet Etching", in Dept. of Elecrical and Computer Eng., University of Maryland, College Park, 2005.
[79] N. Ghalichechian, "Design, Fabrication, and Characterization of a Rotary Variable-capacitance Micromotor Supported on Microball Bearings", in Dept. of Elecrical and Computer Eng., University of Maryland, College Park, 2007.
[80] K.K. Ng, "Complete guide to semiconductor devices", Wiley, New York, 2002.
[81] http://en.wikipedia.org/wiki/Work_function
[82] M.I. Beyaz, N. Ghalichechian, R. Ghodssi, "Toward An Autonomous Electrostatic Micromotor: Integrated Feedback Control", Proceedings of the 21st IEEE International Conference on Micro Electro Mechanical Systems (MEMS 2008), pp. 483-486, Tucson, AZ, USA, January 13-17, 2008.